NTNU

Norwegian University of
Science and Technology

Cement Displacement Efficiency in Rough Pipes

Gunnar Lia Giil

Espen Johansen

Petroleum Geoscience and Engineering
Submission date: June 2017
Supervisor: Pål Skalle, IGP

Norwegian University of Science and Technology
Department of Geoscience and Petroleum

Preface

This Master thesis is written as a part of the study program *Petroleum Engineering* with specialization in *Drilling Engineering*. It was written in the spring semester of 2017, when the undersigned attended the 5th and last year of the study program. The project was developed in cooperation with supervisor professor Pål Skalle.

Trondheim, June 9, 2017

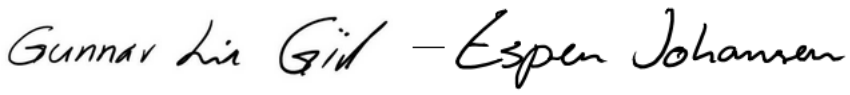

Gunnar Lia Giil — Espen Johansen

Acknowledgements

We would first like to thank our supervisor, professor Pål Skalle at the Department of Geoscience and Petroleum. He has shown strong support, and his door was always open whenever we met problems and needed guidance.

We would also like to thank staff engineers Håkon Myhren and Terje Bjerkan at the mechanical workshop. They were always very helpful when we needed assistance solving problems with the flowloop, and they always stepped up to machine new parts for us.

We would also like to acknowledge Jan David Ytrehus and Bjørnar Lund from SINTEF, together with Benjamin Werner from NTNU for giving us the opportunity to work with them on the DrillWell project. We have learnt a lot from them, and we highly appreciate the close cooperation between SINTEF and NTNU.

Summary

Research within casing string cementing is important in the oil industry. The integrity of an oil well is dependent on the quality of the cement job, and a poor cement job can put the environment, company economics and human lives in severe danger. Mud channels in the cement is often a problem, and if the cement velocity profile experiences no-slip condition at the outer boundaries the mud will be displaced mainly in the center of the annular space, leading to mud channels along the casing string and the formation. If the no-slip condition is not valid, the displacement depends on the slip velocity, or the local velocity. In this report laminar flow were in focus, estimated on basis of the average flow velocity. Turbulent flow requires pressures that many deepwater and extended reach wells can not tolerate. (Giil and Johansen, 2016).

The study is aimed at quantifying a relationship between pipe roughness and local velocity. Experiments were performed in a flow loop where annular flow was simplified to pipe flow. Various water and oil based viscous fluids were used as displacing fluid and displaced fluid, representing cement and spacer respectively. Pipes with three different degrees of roughness were used. The roughness degree was quantified as number of spiral grooves in the pipe wall per length.

The procedure for making two different non-Newtonian water based fluids were presented. A cooperation with SINTEF was also presented, through a brief overview of their large-scale flow loop and presentation of selected results.

Results of this study concludes that cement displacement of spacer can not be modelled in the simple flow loop provided. Gravity segregation and entrance effects dominated the flow, and no clear relationship were found between the roughness degree and the local velocity. Two proposals for better flow loop designs were made and presented in this report.

Norsk sammendrag:

Forskning innen sementering av foringsrør er viktig for oljeindustrien. Integriteten til en brønn er avhengig av kvaliteten på sement-jobben, og en dårlig sementjobb kan sette miljøet, selskaps-økonomien og menneskeliv i fare. Slam-kanaler i sementen er ofte et problem, og hvis sementens hastighet-profil opplever no-slip-betingelsen mot de ytre grensene vil slammet bli fortrengt hovedsakelig midt i ringrommet. Dette fører til slam-kanaler både langs foringsrøret og formasjonen. Hvis no-slip-betingelsen ikke er gyldig vil fortrengningen avhenge av slip-hastigheten, eller den lokale hastigheten langs grensen. I denne rapporten er laminær strømning i fokus, beregnet på grunnlag av gjennomsnittlig strømningshastighet. Turbulent strømning krever trykk som mange dypvannsbrønner og brønner med lange brønnbaner ikke kan håndtere.

Denne studien har som mål å kvantifisere en sammenheng mellom ruhet og lokal hastighet. Eksperimenter ble gjort i en strømningssløyfe hvor annulær strømning var forenklet til rørstrømning. Flere vann- og oljebaserte viskøse væsker ble brukt som fortrengende og fortrengt fluid, for å representere henholdsvis sement og spacer. Rør med tre forskjellige grader av ruhet ble benyttet. Ruhets-graden ble kvantifisert som antall spiral-spor i rørveggen per lengdemeter.

Prosedyre for å lage to forskjellig ikke-Newtonske vannbaserte fluider ble presentert. Et samarbeid med SINTEF ble også presentert, gjennom et lite overblikk over deres større skala strømningssløyfe og presentasjon av utvalgte resultater.

Resultater fra denne studien konkluderer med at sement som fortrenger en spacer ikke kan bli modellert i den enkle små-skala strømningssløyfen. Gravitasjonssegregering og inngangseffekter dominerte strømningen, og et klart forhold mellom ruhet og lokal hastighet ble ikke funnet. To forslag til et forbedret strømningssløyfedesign ble laget og presentert i denne rapporten.

Contents

List of Figures

List of Tables

1. *Introduction*

In the petroleum industry, a significant number of the wells drilled experience problems during their productive lifetime due to poor cement jobs. The consequences of a poor cement job depend on the downhole situation. In some cases the drilling/production has to be paused in order to perform a squeeze job in the well, which again leads to economical costs and delay of production. A bad cement job may also lead to more severe consequences, such as harm to the environment caused by oil spills. Worst-case scenario is a blowout, which besides environmental damage and economic cost, can put human lives on an oil rig in severe danger.

The Macondo incident in the Gulf of Mexico is an example of a fatal disaster, partly caused by a poor cement job. This blowout led to huge environmental damage, enormous economic costs and loss of human life.

Poor cement jobs are often resulting in poor bond between the wellbore, cement and casing, which could be caused by the unfavourable velocity profile. The laminar velocity profile with no-slip condition at the wellbore wall will give no bond at all. Laminar flow in smooth pipes is modelled very detailed by Cengel and Cimbala (2006). Cement flow in the annulus between the formation and the casing will, however, experience rough surfaces. This is specially the case at the formation side. Experience indicate that the no-slip condition is not valid due to the roughness at the walls.

A squeeze cement job is one of the few options of repairing a poor cement job (Bourgoyne Jr. et al., 1986). This is a time consuming and costly activity. Another option would be to plug the well and drill a sidetrack, which is even more costly.

Our goal is to develop a model of the displacement efficiency as a function of pipe roughness. A sub goal is to prove it valid for annular displacement in real boreholes.

To reach the goal we first need to check if something similar has been investigated. If so, we can learn the basic building blocks and start our investigation from there. As a basis for

this Master thesis we build on the autumn project (Giil and Johansen, 2016). Compared to the autumn project the experimental fluids will be more realistic, and experiments with rough pipe will also be performed. The theoretical basis will be the same, but with more detailed studies of the impact of rough pipe on non-Newtonian fluids.

This project will use the flow loop setup used in the autumn project (Giil and Johansen, 2016). The flow loop experiments need to investigate how pipe roughness influences the displacement efficiency. For this purpose we must develop mathematical models in which the roughness is included as a direct or indirect parameter. To determine displacement efficiency, a mass balance calculation for the pipe is executed. By comparing theoretical and observed displacement, the true velocity profile can be determined.

Experiments are performed in the pre-existing flow loop at PTS. Annular flow is here simplified to pipe flow, and cement and spacer will be simulated by various water and oil based viscous fluids.

2. *Previous relevant experience*

This chapter gives a view on previous studies on cement displacement, and presents factors that influence the process. Parts of this chapter are inspired by the report from the autumn project in TPG4560 (Giil and Johansen, 2016).

2.1 Density and rheology of the displacing fluid

When determining the desired density of your cement slurry there are two important boundary conditions. It has to give a hydrostatic overpressure in your well to prevent inflow of formation fluid, and be light enough to not exceed the formation strength (Bourgoyne Jr. et al., 1986). Most often the formation strength will be the limiting parameter, and you have to focus on proportioning your cement light enough.

According to Bu et al. (2016) it is the density difference between the displacing fluid and the fluid to be displaced that is of importance for the displacement efficiency. This optimal density difference depends on the inclination of the pipe and the eccentricity of the casing. The model for finding this optimal density difference is made for Herschel-Bulkley fluids, flowing in annular flow. This optimal density difference is more important for experiments where annular flow might be performed.

For optimal displacement the viscosity of the displacing fluid should be greater than the viscosity of the displaced fluid (Braghini et al., 2010). In this case the properties of the displacing fluid will dominate the flow.

2.1.1 Rheology for Newtonian fluids

A Newtonian fluid begins to deform instantly when a shear stress or force is applied to it. After movement has been initiated, the degree of movement is proportional to applied stress (Hawker, 2001). The relationship is shown in Figure 2.1 and Equation 2.1. We see a linear

relationship between shear stress, τ, and shear rate, γ. The slope of the line, or the gradient, is the viscosity, μ. Water and parafine oil (e.g. Exxsol D60) are Newtonian fluids.

$$\tau = \mu\gamma \tag{2.1}$$

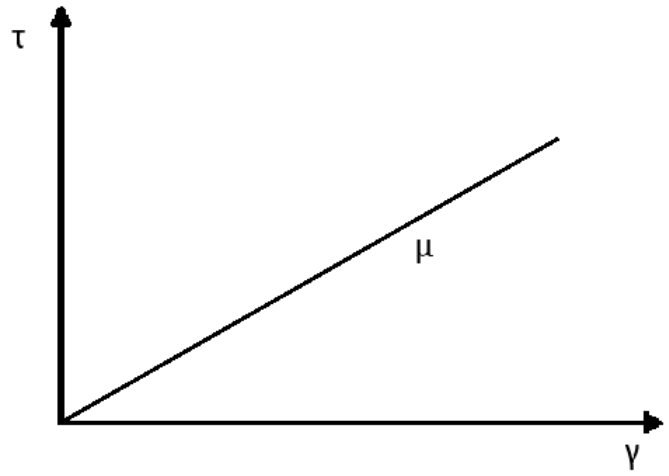

Figure 2.1: *Shear stress vs shear rate for a Newtonian fluid (Giil and Johansen, 2016).*

2.1.2 Rheology for non-Newtonian fluids

Most drilling fluids and cement slurries are non-Newtonian fluids. The Bingham Plastic Model (Equation 2.2) and the Power Law Model (Equation 2.3) are two models that are widely used in the oil industry (Hawker, 2001). Here τ_0 is the yield stress, μ_{pl} the plastic viscosity, K is the consistency factor and n is the flow index. The relationship between the shear stress and shear rate is shown in Figure 2.2.

$$\tau = \tau_0 + \mu_{pl}\gamma \tag{2.2}$$

$$\tau = K\gamma^n \tag{2.3}$$

In many cases these models do not describe the rheological properties in a satisfying way as a fluid may require a yield stress and in the same time be shear thinning/thickening (Shahriar, 2011; Olowolagba and Yerubandi, 2011). Herschel-Bulkley combines these two models as shown in Figure 2.3. The relationship between shear stress and shear rate for a Herschel-Bulkley fluid is shown in Equation 2.4. As for the Bingham and Power-law fluids, τ_0

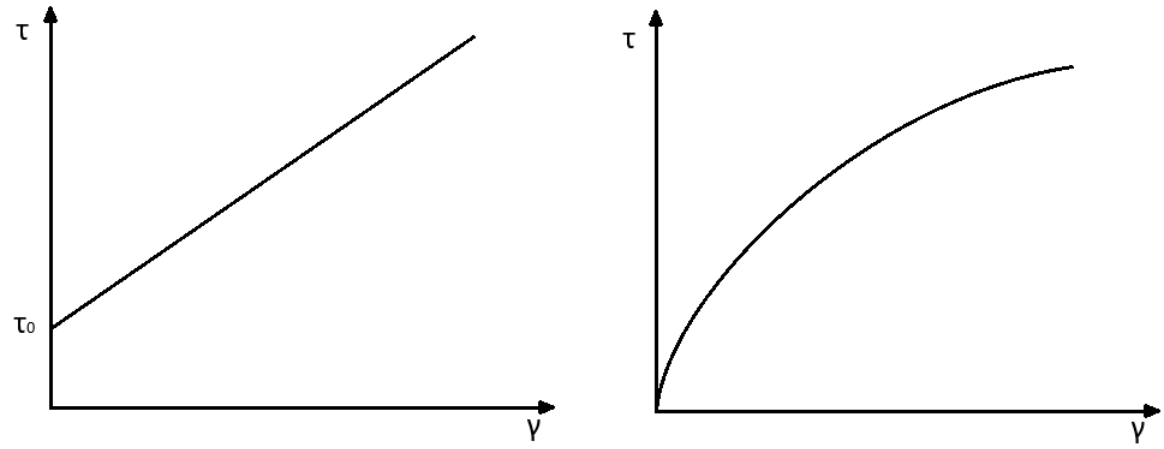

Figure 2.2: *Shear stress vs shear rate for Bingham and Power Law fluids, to the left and right respectively (Giil and Johansen, 2016).*

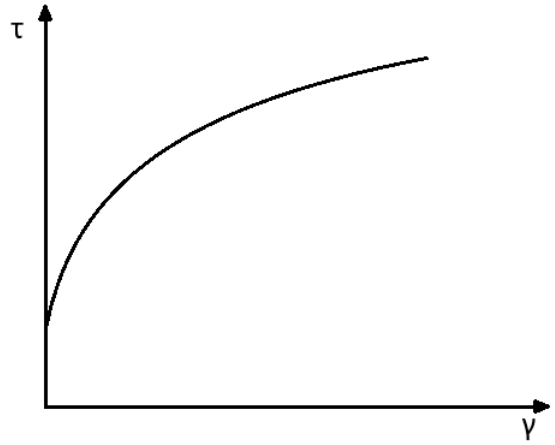

Figure 2.3: *Shear stress vs shear rate for a Herschel-Bulkley fluid (Giil and Johansen, 2016).*

is the yield stress, K is the consistency factor and n is the flow index.

$$\tau = \tau_0 + K\gamma^n \tag{2.4}$$

2.1.3 Interpretation of rheological measurements

Measurements of rheological properties from SINTEF (Lund, 2016), gave the results presented in Table 2.1. $1\ lb/100ft^2 = 0.48\ Pa$, and for a standard Fann Viscometer setup the shear rate (γ) can be obtained by the relationship $\gamma = 1.703RPM$ (Lam and Jefferis, 2014). These conversion factors are used to present the data in SI-units. As stated above, this data can be used to decide which rheological model that fits best. To do this the data set is plotted, and a regression analyses is performed in Excel. Excel has built in regression models that fit with

Table 2.1: *Rheological properties for CMC-fluid from July 2016. T=24°C.*

RPM	Shear stress $lb/100ft^2$	Shear rate $1/s$	Shear stress Pa
600	79.0	1021.80	37.92
300	55.0	510.90	26.40
200	45.0	340.60	21.60
100	30.0	170.30	14.40
6	8.5	10.22	4.08
3	6.0	5.11	2.88

Newtonian, Bingham and Power-law rheological models, and this is shown in Figure 2.4. The Herschel-Bulkley rheological model is also included, but that is more advanced, and more steps are necessary. In the industry it is often assumed that $\tau_0 = \tau_{3RPM}$, but this simplification will clearly lead to error. Another possibility is to perform 10 sec gel strength tests, but that is also not a recommended approach (Hemphill, 1993). The method developed by Hemphill (1993) is shown in Appendix C, and because of the non-linearity of the system of equations, Excel's solver tool is used to determine the value of the yield point, τ_0, the consistency factor K, and the flow index n. Graphical interpretation and comparison of R^2-value, or the coefficient of determination, for the four models indicates what is the best model. R^2 for the four models are shown in Table 2.2, and Herschel-Bulkley rheological model represents the fluid best in this particular example. The R^2-value describes the fraction of total variation in τ that is explained by variation in γ, and closer to 1 is better. This means that for the Herschel-Bulkley model, 0.04% of the variation in τ is a consequence of the model not being perfect.

Table 2.2: *R^2-value for the four models in the six points.*

Model	Coefficient of determination
Herschel-Bulkley	$R^2 = 0.9996$
Power-law	$R^2 = 0.9965$
Bingham	$R^2 = 0.9351$
Newton	$R^2 = 0.8774$

,

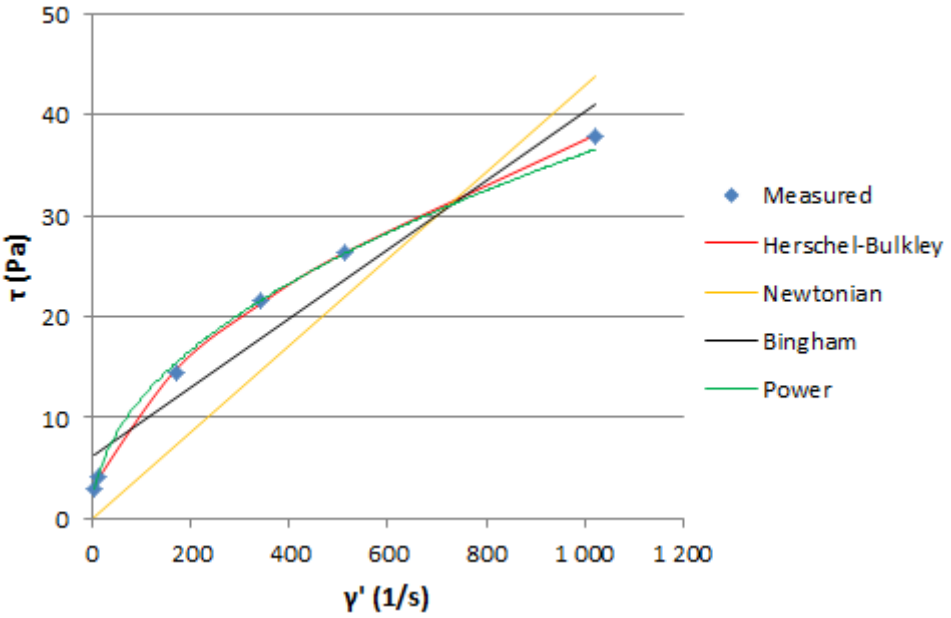

Figure 2.4: *Measured data from Table 2.1 compared to the four rheological models.*

2.2 Flow profile during laminar slick pipe flow

The velocity profile will be different for the different fluid types, because of the difference in rheological properties. Below are central parts in the derivation of the velocity profile for slick pipe flow of Newtonian and non-Newtonian fluids presented. The general expression for the shear stress in laminar pipe flow is shown in Equation 2.5. A central concept here is that this representation is not dependent on fluid type (Syvum Technolgies Inc., 1999).

$$\tau = \frac{\Delta p}{2L} r \tag{2.5}$$

2.2.1 Velocity profile for Newtonian fluids

Derivation of the velocity profile for laminar pipe flow of a Newtonian fluid is shown in detail on pp. 343-345 in Cengel and Cimbala (2006), and the central steps are shown below.

A force balance of the viscous and pressure forces on a volume element in the flow can be executed and is shown in Equation 2.6. The derivation of this equation is based on Figure 2.5.

$$-\left[(2\pi r\ dr\ P)_x - (2\pi r\ dr\ P)_{x+dx}\right] = (2\pi r\ dx\ \tau)_r - (2\pi r\ dx\ \tau)_{r+dr} \tag{2.6}$$

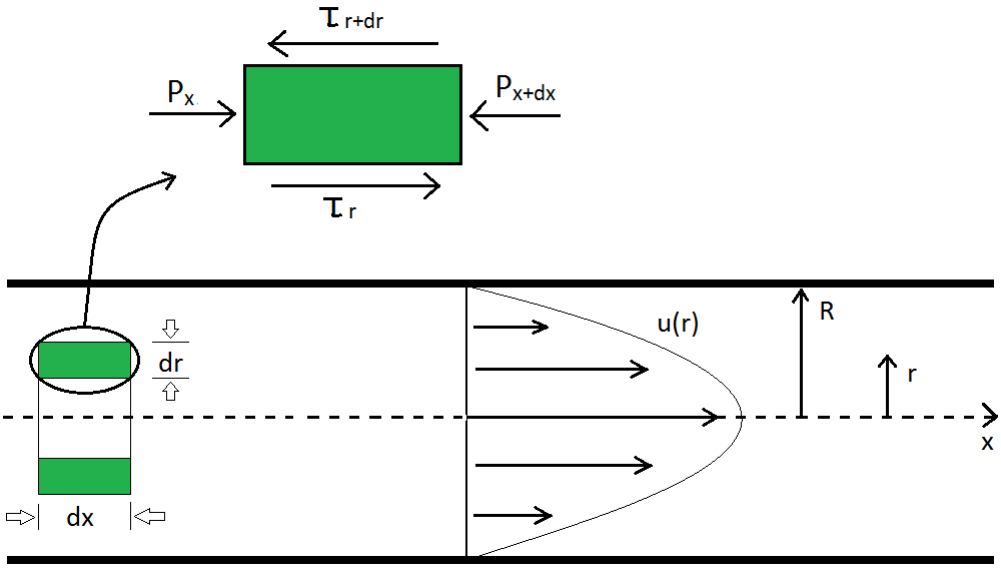

Figure 2.5: *Basis for mass balance equation (Cengel and Cimbala, 2006).*

Dividing by $2\pi\ dr dx$ and letting dr and $dx \to 0$ gives

$$r\frac{dP}{dx} = -\frac{d(r\tau)}{dr}.$$

Further, implementing that $\tau = -\mu(dv/dr)$ gives Equation 2.7.

$$\frac{dP}{dx} = \frac{\mu}{r}\frac{d}{dr}\left(r\frac{dv}{dr}\right) \tag{2.7}$$

Integrating twice, and applying boundary conditions $(dv/dr) = 0$ at $r = 0$, and $v = 0$ at $r = R$, gives the equation for the velocity profile for laminar pipe flow of a Newtonian fluid, as shown in Equation 2.8.

$$v(r) = \frac{R^2}{4\mu} \times \left(\frac{\Delta P}{L}\right)\left[1 - \frac{r^2}{R^2}\right] \tag{2.8}$$

Equation 2.9 is the definition of the average velocity, $\bar{v}$.

$$\bar{v} = \frac{2}{R^2}\int_0^R v(r) r\ dr \tag{2.9}$$

Inserting the expression for $v(r)$ from Equation 2.8 into Equation 2.9 and integrating gives Equation 2.10 (Cengel and Cimbala, 2006), which describes the velocity profile independent of the fluid viscosity and density.

$$v(r) = 2\bar{v}\left(1 - \frac{r^2}{R^2}\right) \tag{2.10}$$

2.2.2 Velocity profile for Bingham fluids

As shown in Equation 2.2, the viscosity of a Bingham fluid is dependent on the applied shear rate. The velocity profile is shown in Figure 2.6. The plug flow region ($r < r_0$) is the region where the $\tau < \tau_0$, and r_0 can be found with Equation 2.11 (Mehari, 2016).

$$\tau_0 = \frac{\Delta p}{2L} r_0 \tag{2.11}$$

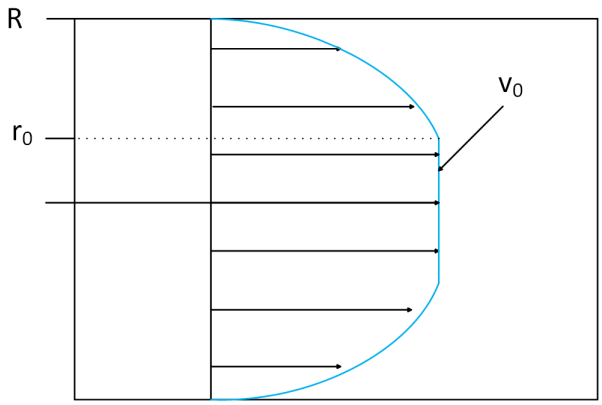

Figure 2.6: *Velocity profile for Bingham fluids (Giil and Johansen, 2016).*

For laminar pipe flow, the velocity profile for a Bingham fluid is described in Equation 2.12 (Syvum Technolgies Inc., 1999).

$$v(r) = \begin{cases} \frac{\Delta p R^2}{4\mu_{pl} L}\left[1 - \frac{r_0}{R}\right]^2 & \text{for } r \leq r_0 \\ \frac{\Delta p R^2}{4\mu_{pl} L}\left[1 - \left(\frac{r}{R}\right)^2\right] - \frac{\tau_y R}{\mu_{pl}}\left(1 - \frac{r}{R}\right) & \text{for } r_0 < r < R \end{cases} \tag{2.12}$$

2.2.3 Velocity profile for Power-law fluids

By substituting $\gamma = -dv/dr$ into Equation 2.3 and integrating with no-slip boundary condition the expression for the velocity profile for a Power-law fluid shown in Equation 2.13 can be obtained. The velocity profile is illustrated in Figure 2.7.

$$v(r) = \left(\frac{\Delta P}{L}\frac{R}{2k}\right)^{1/n} \frac{R}{(1/n)+1}\left[1 - \left(\frac{r}{R}\right)^{(1/n)+1}\right] \tag{2.13}$$

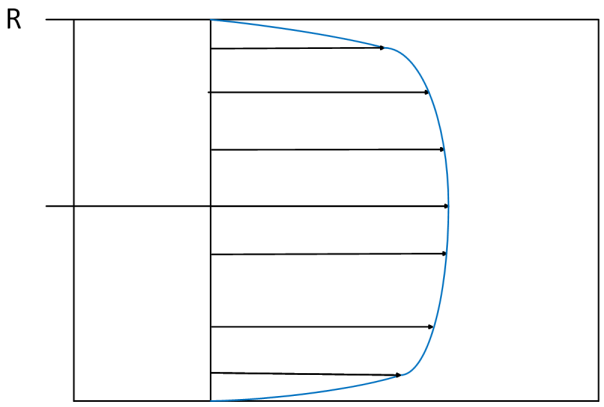

Figure 2.7: *Velocity profile for Power-law fluids (Giil and Johansen, 2016).*

2.2.4 Velocity profile for Herschel-Bulkley fluids

Most drilling muds and cements fits better with the Herschel-Bulkley rheological model (Shahriar, 2011). The velocity profile will here consist of two parts, a flat plug flow in the middle, and a parabolic shape near the pipe wall. For the plug flow region the yield stress in Equation 2.5 can be expressed as

$$\tau_0 = \frac{\Delta p}{2L} r_0. \tag{2.14}$$

By substituting the shear rate by $-dv/dr$ in Equation 2.4 the shear stress can be expressed by Equation 2.15.

$$\tau = \tau_0 + K\left(\frac{-dv}{dr}\right)^n \tag{2.15}$$

By combining Equation 2.5, 2.14 and 2.15 and integrating along the pipe radius the velocity profile for Herschel-Bulkley fluids can be expressed as Equation 2.16 with the plug flow velocity v_0 specified in Equation 2.17 (Mehari, 2016).

$$v(r) = \begin{cases} v_0 \left[1 - \left(\frac{r-r_0}{R-r_0}\right)^{\frac{n+1}{n}}\right] & \text{for } r_0 \le r \le R \\ v_0 & \text{for } r \le r_0 \end{cases} \tag{2.16}$$

$$v_0 = \left(\frac{\Delta p}{2KL}\right)^{\frac{1}{n}} \left(\frac{n}{n+1}\right) (R - r_0)^{\frac{n+1}{n}} \tag{2.17}$$

2.3 Flow profile during laminar rough pipe flow

When a primary cement job is performed, the flowing cement will not experience slick walls. On one side it will be in contact with the open hole, which is the drilled out rock. This is very rough, and the roughness can be illustrated with the caliper log in Figure 2.8. The dotted line represents the bit size, and the solid line represents the actual hole size. In addition to roughness induced by drilling, the borehole also has roughness with smaller magnitude. This type of roughness is present due to BHA scraping and the fact that formation rock has natural roughness due to grain size. This smaller magnitude roughness is what will be in focus in this model.

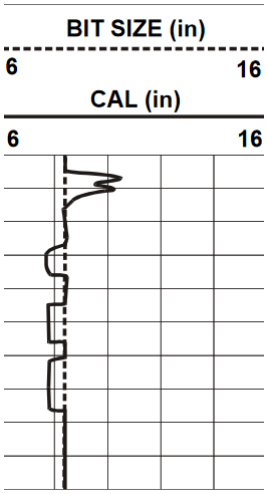

Figure 2.8: *Example of a caliper log (Glover, 2000).*

The roughness described above is found on the formation surface in the annulus. Another surface present in the annulus is the outside of the casing. In Cengel and Cimbala (2006) the surface roughness of commercial steel is given to be 0.045 mm. The roughness in our flow loop will have a greater value than the roughness mentioned for commercial steel, and therefore more comparable to the roughness on the formation surface of the annulus. The surface roughness may increase the slip velocity, and hence also the displacement efficiency.

For flow in rough pipes it is more difficult to quantify the velocity profile because of local turbulence on the pipe wall inducing a slip velocity. With this as a basis, we have to create a simplified equation with v_{local} included as the velocity at the pipe wall.

2.3.1 Local velocity for Newtonian fluids

v_{local} is the slip velocity and v_x is an unknown which has to be defined. This is shown in Equation 2.18.

$$v(r) = v_{local} + v_x\left(1 - \frac{r^2}{R^2}\right) \tag{2.18}$$

To determine v_x some mathematical steps has to be performed. The volumes in the slick and rough pipes has to be preserved. This criteria is fulfilled when the flow rates are equal as shown in Equation 2.19.

$$q_{slick} = q_{rough} \tag{2.19}$$

The mass balance in Equation 2.19, can be rewritten as Equation 2.20 by expressing the rate as the integral $q = \int v(r) \times 2\pi r dr$.

$$\int_{slick} v(r) \times 2\pi r dr = \int_{rough} v(r) \times 2\pi r dr \tag{2.20}$$

Solving Equation 2.20 in terms of v_x results in Equation 2.21.

$$v_x = 2(\bar{v} - v_{local}) \tag{2.21}$$

The previous unknown v_x is now defined and can be put into Equation 2.18 as shown in Equation 2.22.

$$v(r) = v_{local} + 2(\bar{v} - v_{local})\left(1 - \frac{r^2}{R^2}\right) \tag{2.22}$$

Here v_{local} describes the slip velocity at the wall. $\bar{v}$ is the average velocity in the pipe as in Equation 2.23. R is the inner radius of the pipe and r is the varying radius where you want to investigate the velocity. The maximum velocity, v_{max}, is given in equation 2.24.

$$\bar{v} = \frac{q}{A} \tag{2.23}$$

$$v_{max} = 2\bar{v} - v_{local} \tag{2.24}$$

The velocity profiles with and without a slip velocity are shown in Figure 2.9, together with the resulting displacement profiles.

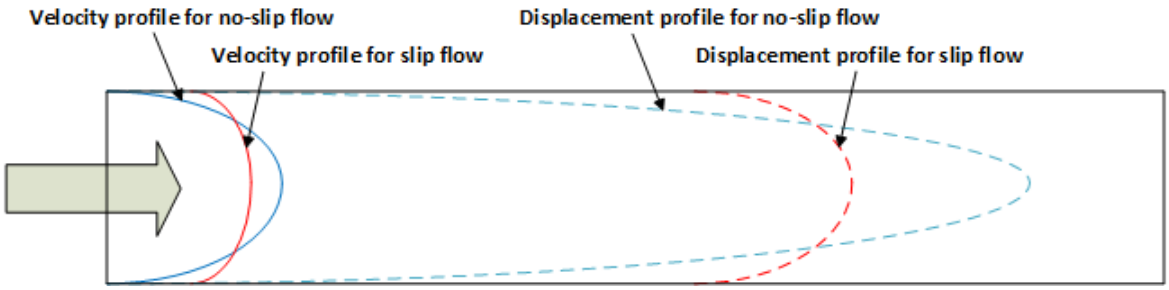

Figure 2.9: *Velocity profiles for slip and no-slip flow with corresponding displacement profiles (Giil and Johansen, 2016).*

2.3.2 Local velocity for Bingham fluids

As for the Newtonian fluids, the velocity profile expression for Bingham fluids can be modified to include a slip velocity, v_{local}. This can be written on the form shown in Equation 2.25.

$$v(r)_{rough} = v_{local} + c \times v(r)_{slick} \tag{2.25}$$

By performing the mass balance shown in Equation 2.20 and integrating over the radius of the pipe an expression of c can be found, as shown in Equation 2.26.

$$c = 1 - \frac{v_{local} R^2}{2\left(\frac{\Delta p}{L}\frac{R^2}{4\mu_{pl}}\left[\frac{R^2}{4} + \frac{r_0^2}{4R^2} - \frac{r_3}{R} + \frac{r_0^4}{2R^2}\right] - \frac{\tau_y R}{\mu_{pl}}\left[\frac{R^2}{6} - \frac{r_0^2}{2} + \frac{r_0^3}{3R}\right]\right)} \tag{2.26}$$

The final expression for the velocity profile for a Bingham fluid flowing in a rough pipe is shown in Equation 2.27.

$$v(r) = v_{local} + c \times \begin{cases} \frac{\Delta p R^2}{4\mu_{pl} L}\left[1 - \frac{r_0}{R}\right]^2 & \text{for } r \leq r_0 \\ \frac{\Delta p R^2}{4\mu_{pl} L}\left[1 - \left(\frac{r}{R}\right)^2\right] - \frac{\tau_y R}{\mu_{pl}}\left(1 - \frac{r}{R}\right) & \text{for } r_0 < r < R \end{cases} \tag{2.27}$$

2.3.3 Local velocity for Power-law fluids

Following the same path as for the Newtonian fluid, the expression for the velocity profile including slip velocity v_{local} for Power-law fluids will be on the form shown in Equation 2.28.

$$v(r) = v_{local} + C\left(\frac{\Delta p}{L}\frac{R}{2K}\right)^{\frac{1}{n}} \frac{R}{\frac{1}{n}+1}\left[1 - \left(\frac{r}{R}\right)^{\frac{1}{n}+1}\right] \tag{2.28}$$

C can be determined by performing the mass balance for slick and rough pipe shown in Equation 2.20. Integrating over the radius gives the final expression for the velocity profile for a rough pipe flow of a Power-law fluid, shown in Equation 2.29.

$$v(r) = v_{local} + \frac{1}{\frac{1}{n}+1}\left[\left(\frac{\Delta p}{L}\frac{R}{2K}\right)^{\frac{1}{n}} R - v_{local}\left(\frac{1}{n}+3\right)\right]\left[1-\left(\frac{r}{R}\right)^{\frac{1}{n}+1}\right] \tag{2.29}$$

2.3.4 Local velocity for Herschel-Bulkley fluids

When introducing slip velocity to the velocity profile for a Herschel-Bulkley fluid (Equation 2.16), following the same path as for the Newtonian fluid, the result is shown in Equation 2.30.

$$v(r) = \begin{cases} v_{local} + cv_0\left[1-\left(\frac{r-r_0}{R-r_0}\right)^{\frac{n+1}{n}}\right] & r_0 < r < R \\ v_{local} + cv_0 & r \leq r_0 \end{cases} \tag{2.30}$$

Here cv_0 is determined by performing the mass balance for slick and rough pipe as shown in Equation 2.20. v_0 is shown in Equation 2.17, and c is determined by integrating over the radius. This gives the expression for cv_0 shown in Equation 2.31.

$$cv_0 = \left(1 - \frac{v_{local}R}{v_0\left[R - \frac{n}{2n+1}(R-r_0)\right]}\right)\left[\left(\frac{\Delta p}{2KL}\right)^{\frac{1}{n}}\left(\frac{n}{n+1}\right)(R-r_0)^{\frac{n+1}{n}}\right] \tag{2.31}$$

2.4 Viscous sublayer

Flow regime dictates velocity profile and in turn the displacement profile and overall displacement of the flow. This section presents a detailed explanation of four different regions seen over the cross section of turbulent flow. The turbulent flow regime is investigated since it has interesting regions, and the inner region is dominated by viscous effects similar to laminar flow. This section is to a large extent inspired from Cengel and Cimbala (2006), and further elaborations of the equations can be found in their work.

During pipe flow, different flow regimes might occur due to different rheological properties of the fluids, flow rate etc.. The three different flow regimes are laminar flow, turbulent flow and a combination of both laminar and turbulent flow called transitional flow. Commonly, these three flow regimes are separated and characterized by the Reynold number. Laminar

flow occurs for a Reynold number below 2300, while turbulent flow regime is present for a Reynold number above 4000. The region between laminar and turbulent ($2300 > Re > 4000$) is called the transitional flow regime (Cengel and Cimbala, 2006). These Reynold number limits are not absolute, but indicative values. For instance transitional flow can occur at $Re = 2100$. Velocity profiles representing laminar flow and turbulent flow are different and shown in Figure 2.10.

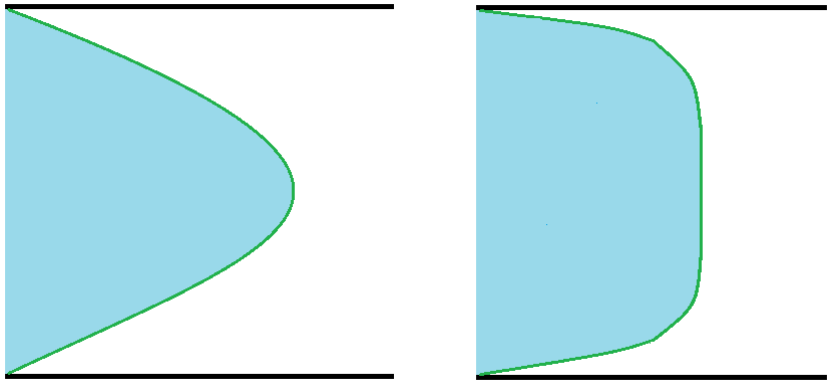

Figure 2.10: *Laminar velocity profile (left) and turbulent velocity profile (right).*

During turbulent flow, the flow profile can be divided into four regions across the cross section of the pipe. These regions are shown in Figure 2.11, and are called the viscous (laminar) sublayer, the buffer layer, the overlap layer and the outer layer.

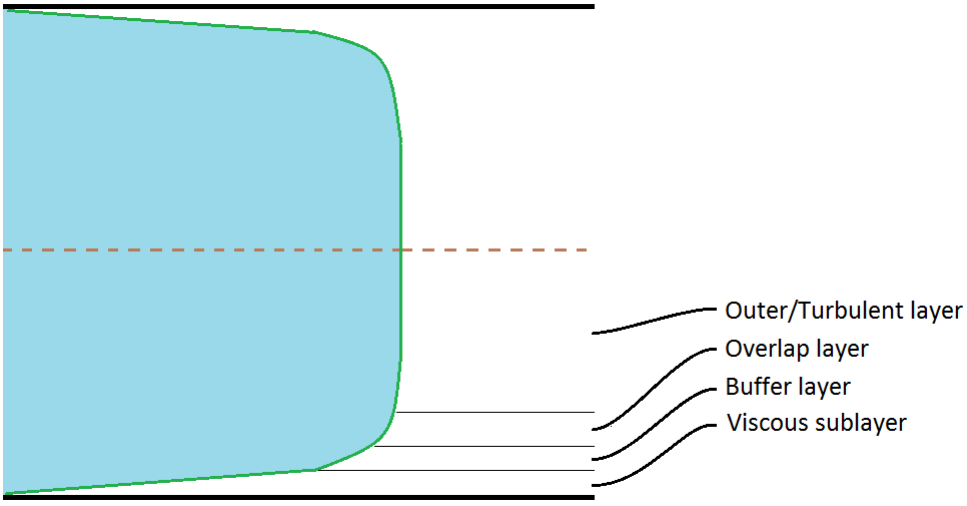

Figure 2.11: *Different layers occurring during pipe flow with respect to a turbulent velocity profile.*

The region farthest from the wall is the outer layer. This layer is the widest in terms of cross section distance, as illustrated in Figure 2.11. The outer layer is turbulent and is dominated by

turbulent effects instead of viscous effects. Equation 2.32 represents the velocity profile for the outer layer and is called velocity defect law. v_* is called the friction velocity and expressed as; $v_* = \sqrt{\tau_w/\rho}$.

$$\frac{v_{max} - v}{v_*} = 2.5 \ln \frac{R}{R-r} \tag{2.32}$$

Next to the outer layer, the overlap layer is present. This layer is affected by both turbulent and viscous effects. The turbulent effect is significant but not dominant. The velocity profile for this region is represented by Equation 2.33.

$$\frac{v}{v_*} = 2.5 \ln \frac{y v_*}{\nu} + 5.0 \tag{2.33}$$

The second innermost layer is called the buffer layer. The buffer layer is dominated by viscous effects, and to some degree affected by turbulence.

Closest to the wall is the region called the viscous sublayer. The flow occurring in this thin layer is laminar and dominated by viscous forces. Figure 2.11 shows that the velocity profile in this region is close to linear. During no-slip condition, the particle velocity at the wall is zero. Equation 2.34 is called the law of the wall and describes the velocity profile within the viscous sublayer. Equation 2.35 describes the thickness of the viscous sublayer (Cengel and Cimbala, 2006).

$$\frac{v}{v_*} = \frac{y v_*}{\nu} \tag{2.34}$$

$$y = \delta_{sublayer} = \frac{5\nu}{v_*} = \frac{25\nu}{v_\delta} \tag{2.35}$$

Based on descriptions of the four layers above, we know that the amount of turbulence within the layers is decreasing towards the pipe wall. Close to the wall the flow appears laminar.

Although the viscous sublayer is, by many, considered laminar, there are research suggesting otherwise. During research Corino and Brodkey (1969) has observed that turbulent eddies occur also in the the viscous sublayer, but to a much lesser degree in terms of frequency and size compared to adjacent regions. Most of the disturbances in the region closest to the wall were observed produced by the adjacent regions further away from the wall.

The thickness of the viscous sublayer is typically less than 1 percent of the pipe diameter. Even though the thickness of this region is very small, the effect on the overall flow is considered to be large. This is due to the large velocity gradient, shown in Figure 2.11. Roughness has an effect on the viscous sublayer, and thus also on the overall flow. The impact on the flow is significant if the roughness height is comparable to the viscous sublayer thickness (Cengel and Cimbala, 2006).

The viscous sublayer is a subject during turbulent flow and studied mainly in terms of heat transfer. Unlike the turbulent region, the laminar flow in the viscous sublayer region prevents mixing of fluid in the direction perpendicular to the direction of flow, reducing heat transfer.

The different regions described in this section applies to a turbulent flow regime. The overall tendency is that viscous forces tend to dominate towards the wall. Having in mind that laminar flow is driven by viscous forces, we apply theory about the viscous sublayer obtained from turbulent flow theory, to the region close to the wall in our study of laminar flow.

3. *Model development*

3.1 Model assumptions

In order to succeed in understanding of the physical phenomena and creating models, simplifications are in many cases necessary. Simplifications used for the model and experimental work were in general:

1. Velocity profile was stationary for the pipe length
2. The presence of a mixing front of the two fluids had negligible impact on the flow profile
3. Viscous forces dominated the flow, and gravitational forces were neglected

3.1.1 Stationary velocity profile

As described by Cengel and Cimbala (2006) theoretical solutions for pipe flow can be obtained only in specific simple cases. The assumption that the flow is fully developed in the test pipe with a stationary velocity profile is key here. Without this assumption the flow is not possible to model.

3.1.2 Impact of mixing on flow profile

The phenomena when an unstable interface between two fluids is forming unsystematic patterns is called fingering. If such a pattern is formed, it leads to an early breakthrough of displacing fluid, and the flow gets very challenging to model. By analyzing recorded videos of the displacement, it can be decided if this assumption was valid. The assumption of no mixing of the two fluids is closely connected to the constant velocity profile assumption.

3.1.3 Gravitational forces

If viscous forces dominate the flow and gravitational forces can be neglected, the development of a mathematical expression of the displacement efficiency can be derived from the relatively simple expressions of the laminar velocity profile shown in chapter 2. To identify if this is a reasonable assumption, forces on a droplet of the displacing fluid moving in the displaced fluid can be analyzed. This analysis gives only an indication, and to be sure a simplified 2D model of the problem can be developed, or a computational fluid dynamics (CFD) software can be used.

Forces on the displacement front described as viscous and gravitational forces on a droplet

An analysis of the forces acting on a droplet can be performed. The derivation is shown below, and here F_g are the sum of the gravitational and buoyancy forces, and F_τ are the viscous forces acting on a droplet of fluid falling in another fluid. The balance of these forces is shown in Equation 3.3, and the expression for the two forces are shown in Equation 3.1 and 3.2. This leads to the expression for the falling velocity of the droplet given in Equation 3.4.

$$F_g = mg = \rho V g = (\rho_1 - \rho_2) g \frac{4}{3} \pi r^3 \tag{3.1}$$

$$F_\tau = \Delta p A = 6\pi \mu r_d v_d \tag{3.2}$$

$$F_g = F_\tau \tag{3.3}$$

$$v_d = \frac{g d_d^2}{18\mu} (\rho_1 - \rho_2) \tag{3.4}$$

The scenario is described in Figure 3.1, which is a sketch of the displacement profile at a short distance from the inlet. The front of the displacement is simplified to be described as a droplet, and the force balance is applied on this.

By inserting typical values shown in Table 3.1, the downwards velocity of a droplet of Laponite-fluid falling in oil can be obtained. The value for this is shown in Table 3.2, together with the distance, l_d, it falls travelling through the test pipe for a given scenario. The droplet diameter for this example is half of the pipe diameter.

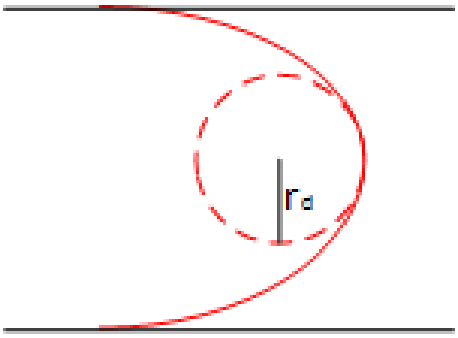

Figure 3.1: *Displacement profile at a short distance from the inlet, with the imaginary droplet for use in the force balance.*

Table 3.1: *Typical values for the Laponite-fluid (1) and oil (2) that will be used in the experiments*

Parameter	Typical value	Unit
ρ_1	1000	kg/m^3
ρ_2	828	kg/m^3
μ_2	17.5	cp
d_d	0.022	m

Table 3.2: *Downwards velocity (v_d) of a droplet of Laponite-fluid (1) falling in oil (2) with typical flow rate and time. The resulting theoretical falling distance (l_d) is included.*

Parameter	Typical value	Unit
v_d	2.59	m/s
q	0.00095	m^3/s
t	20	s
l_d	51.85	m

A similar analysis can be performed for a droplet of CMC-fluid (1) falling in Laponite-fluid (2). Typical values are shown in Table 3.3 with resulting parameters in Table 3.4.

The values obtained for the two scenarios show that the falling velocity and falling distance will lead to segregation. It is important to note that due to the simple approach in this method, this analysis gives only an indication of whether gravity segregation might be a problem or not, and not a definite answer. Not much research has been done on gravitational impact on displacement flow, but Alba et al. (2012) shows that it may impact the flow profile even for low density differences.

Table 3.3: *Typical values for the CMC-fluid (1) and Laponite-fluid (2) that will be used in the experiments*

Parameter	Typical value	Unit
ρ_1	1100	kg/m^3
ρ_2	1000	kg/m^3
μ_2	35	cp
d_d	0.022	m

Table 3.4: *Downwards velocity (v_d) of a droplet of CMC-fluid (1) falling in Laponite-fluid (2) with typical flow rate and time. The resulting theoretical falling distance (l_d) is included.*

Parameter	Typical value	Unit
v_d	0.75	m/s
q	0.00095	m^3/s
t	20	s
l_d	15.07	m

3.2 Displacement efficiency

The expression displacement efficiency can in this context be understood in two different ways, as shown in Giil and Johansen (2016). The volumetric displacement efficiency is the comparison of the displaced volume and the volume initially in place in the flow loop. This is the oil volume read out of the collector tank in the experiment, V_o, divided by the flow loop volume, V_p (Equation 3.5). If a water based displaced fluid is used, the volume can be calculated by using a calibrated conductivity-chart as shown in Figure 3.3. The other type of efficiency is the areal displacement efficiency, shown in Equation 3.6. In Figure 3.2 the areal displacement efficiency at length s from the inlet is the ratio $A_{displacing}/A_{tot}$. The relationship between these two efficiencies are shown in section 3.4.

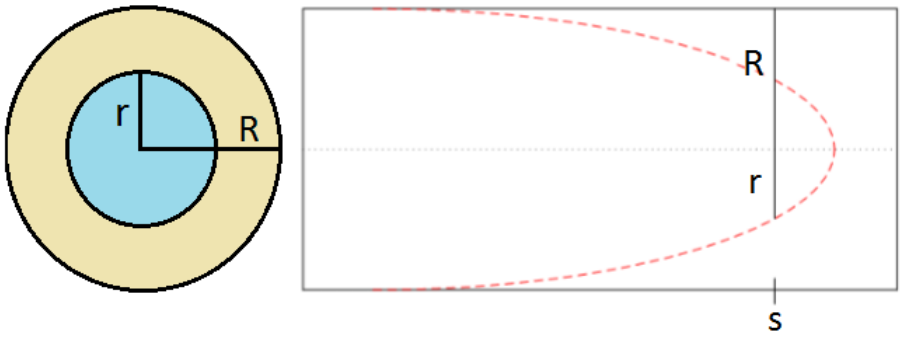

Figure 3.2: *Areal efficiency factor parameters. Cross sectional view and side view of the pipe. s indicates the distance to the point under investigation. (Giil and Johansen, 2016).*

$$\epsilon_v = \frac{V_o}{V_p} \tag{3.5}$$

$$\epsilon_a = \frac{A_{displacing}}{A_{tot}} = \frac{r^2}{R^2} \tag{3.6}$$

3.3 Determining volume of displaced fluid by conductivity measurements

For experiments performed with two water based muds, the muds will mix in the collector tank and the volume of each mud can not be read directly. To solve this, salt is added to one of the muds prior to testing. The salt concentration of the mud will then be proportional with the conductivity (Leinebø, 1971), which can be measured with a conductivity meter at the lab. The fraction of the salt containing fluid will then be proportional to the salt concentration, and the conductivity. A chart to determine the fraction of Laponite-fluid in a mix of Laponite- and CMC-fluid is shown in Figure 3.3. This chart was developed in the laboratory by starting with 100% Laponite-fluid and adding CMC-fluid in small amounts, to measure the increasing conductivity. As read from the chart, this method will be reliable only for fractions of Laponite-fluid greater than 50%. The mix of the two fluids were also observed to be homogenous for these ratios, whereas for ratios of Laponite-fluid lower than 50% it was very difficult to get a homogeneous mix. Table 3.5 shows the different uncertainties associated with the different Laponite fraction regions based on the linear regression done in Excel. The uncertainty values clearly shows that a high Laponite fraction results in better accuracy in terms of volume

fraction readings.

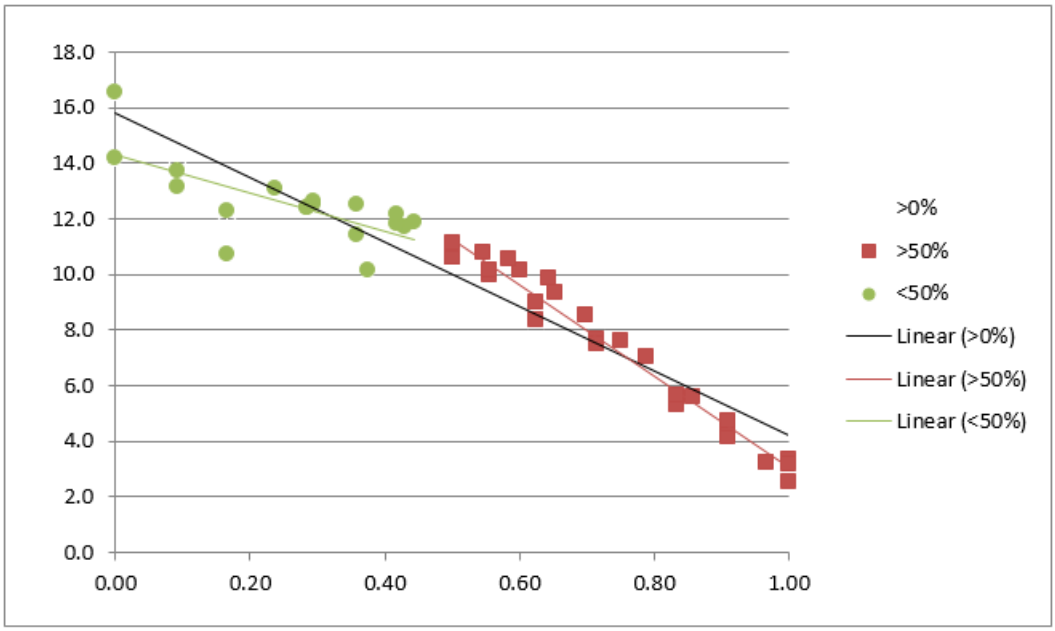

Figure 3.3: *Fraction of Laponite-fluid in mixture vs. conductivity. For Laponite concentrations higher than 50% the model has only 2.6% error. T=20°C.*

Table 3.5: *Linear regression of Laponite fraction vs. conductivity.*

Laponite fraction region	Linear regression	Coefficient of determination
0% to 100%	y = -11.568x + 15.793	R^2 = 0.9027
0% to 50% •	y = -6.7945x + 14.296	R^2 = 0.4978
50% to 100% ■	y = -16.322x + 19.394	R^2 = 0.9733

3.4 Verification of the displacement efficiency based on experimental data

In this section the volumetric and areal displacement efficiencies are explained and derived, developed from Giil and Johansen (2016) to apply for Herschel-Bulkley fluids. These factors are well suited to describe the displacement efficiency in terms of volume and area respectively. The derivations are based on the Herschel-Bulkley model derived and explained in chapter 2.

The velocity profile in Equation 2.30 can be transferred to a displacement profile by multiplying with t, shown in Equation 3.7.

$$s(r,t) = \begin{cases} v_{local}\,t + tcv_0\left[1 - \left(\frac{r-r_0}{R-r_0}\right)^{\frac{n+1}{n}}\right] & \text{for } r_0 < r < R \\ v_{local}\,t + tcv_o & \text{for } r \le r_0 \end{cases} \tag{3.7}$$

This can be solved for the radius of the displacement front, giving Equation 3.8.

$$r(s,t)^2 = \left[(R-r_0)\left(1 - \frac{s - v_{local}\,t}{tcv_0}\right)^{\frac{n}{n+1}} + r_0\right]^2 \tag{3.8}$$

There are three different scenarios for how far the displacement has come, shown in Figure 3.4. The notation S_f and S_t describes the position of the displacement *front* and *tail* respectively.

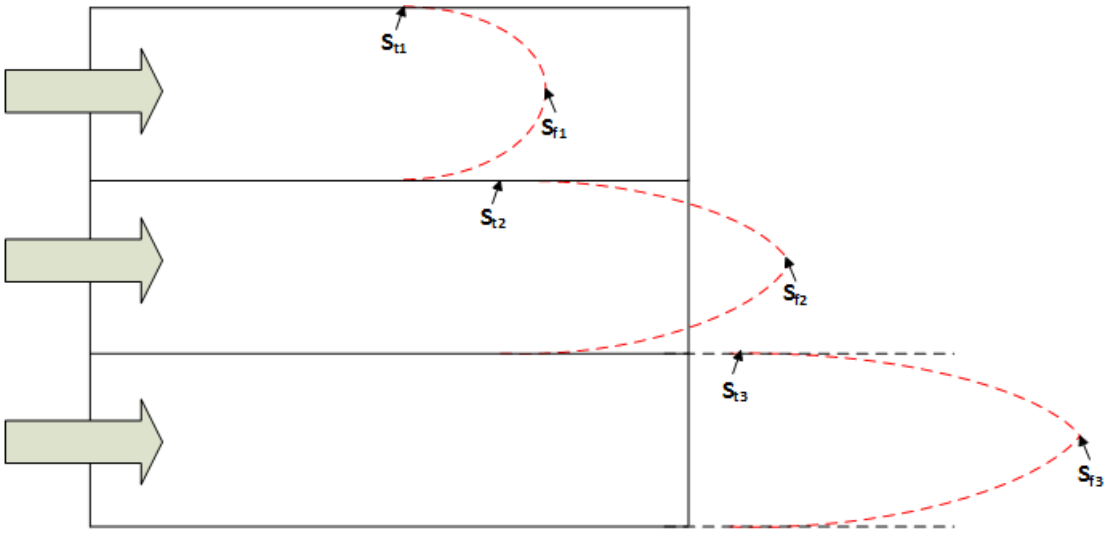

Figure 3.4: *Illustration of the three different scenarios of the displacement front travel length (Giil and Johansen, 2016).*

For scenario 1, $S_f < L$, the volumetric displacement efficiency is given by Equation 3.9.

$$\epsilon_v = \frac{qt}{V_p} \tag{3.9}$$

Scenario 1 is recognized by the presence of only displaced fluid in the collector tank.

For scenario 2, where $S_t \le L \le S_f$, ϵ_v can be derived as follows:

The scenario is shown in Figure 3.5. The displaced volume consists of two parts, V_1 and V_2. Equation 3.5 defines the volumetric efficiency factor ϵ_v, and it can be rewritten as Equation 3.10.

$$\epsilon_v = \frac{V_1 + V_2}{V_p} \tag{3.10}$$

V_1 and V_2 are described below, and combining Equation 3.10, 3.11 and 3.12 results in Equa-

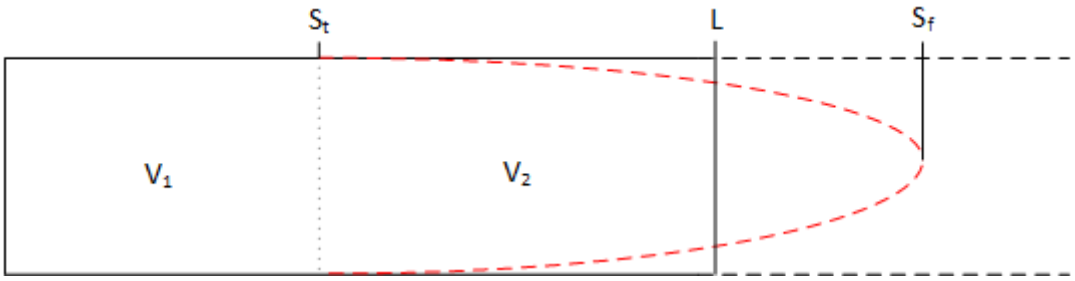

Figure 3.5: *Illustration of the flow loop for displacement scenario 2 (Giil and Johansen, 2016).*

tion 3.13.

$$V_1 = \pi R^2 \times v_{local} t \tag{3.11}$$

$$V_2 = \int_{S_t}^{L} \pi r(s,t)^2 ds \tag{3.12}$$

$$\epsilon_v = \frac{\pi R^2 \times v_{local} t + \int_{S_t}^{L} \pi r(s,t)^2 ds}{V_p} \tag{3.13}$$

Comparing this to experimental data, where ϵ_v is measured, for scenario 2, we can solve Equation 3.13 for v_{local} to get a value for the slip velocity in the pipe for the given flow rate. The areal displacement efficiency can be found by substituting Equation 3.8 into Equation 3.6, shown in Equation 3.14. ϵ_a can here for a given time, t, be found at any point, s, in the pipe where $S_t \leq s \leq S_f$. To be able to compare the results for experiments with different flow rates and flow times, a dimensionless representation of the local velocity was developed. This is shown in Equation 3.15.

$$\epsilon_a = \frac{\left[(R - r_0)\left(1 - \frac{s - v_{local} t}{t c v_0}\right)^{\frac{n}{n+1}} + r_0\right]^2}{R^2} \tag{3.14}$$

$$v^* = \frac{v_{local}}{\bar{v}} \tag{3.15}$$

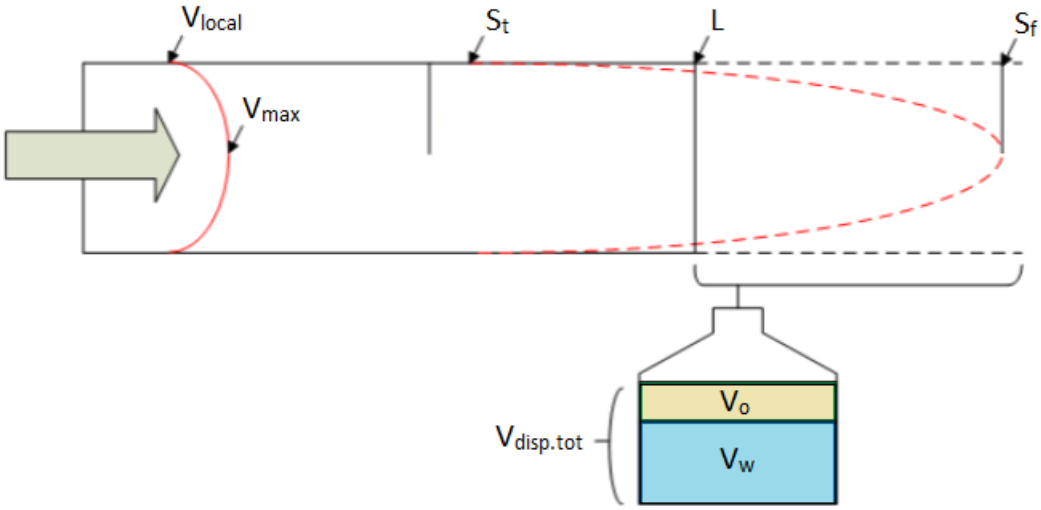

Figure 3.6: *Set-up with explanation of variables and resulting data (Giil and Johansen, 2016).*

3.5 Simulations

In this section the Herschel-Bulkley model is simulated in terms of velocity profile, displacement profile and displacement efficiency. In addition, some of the Herschel-Bulkley simulations are compared to simulations done with the somewhat simpler Newtonian model. Some variables are held constant while other variables are changed to see how certain parameters influence the model. These simulations are done to visualize and understand the model, and to see if the model makes sense in terms of a practical understanding.

3.5.1 Velocity profile and displacement profile

The first simulation is done by varying the local velocity and keeping all the other parameters constant. As seen in Figure 3.7, the graphs have the same shape when comparing displacement profile with velocity profile. This is expected since the only difference between the two, is that the displacement profile is a function of time and the velocity profile is not. More exact: $s(r,t) = v(r) \times t$. The lower plot shows simulations of three different velocity profiles, varying the local velocity. It is clearly shown that the simulation with the lowest local velocity has the highest max velocity. This observation is expected knowing the flow rate is constant and equal for all the three simulations.

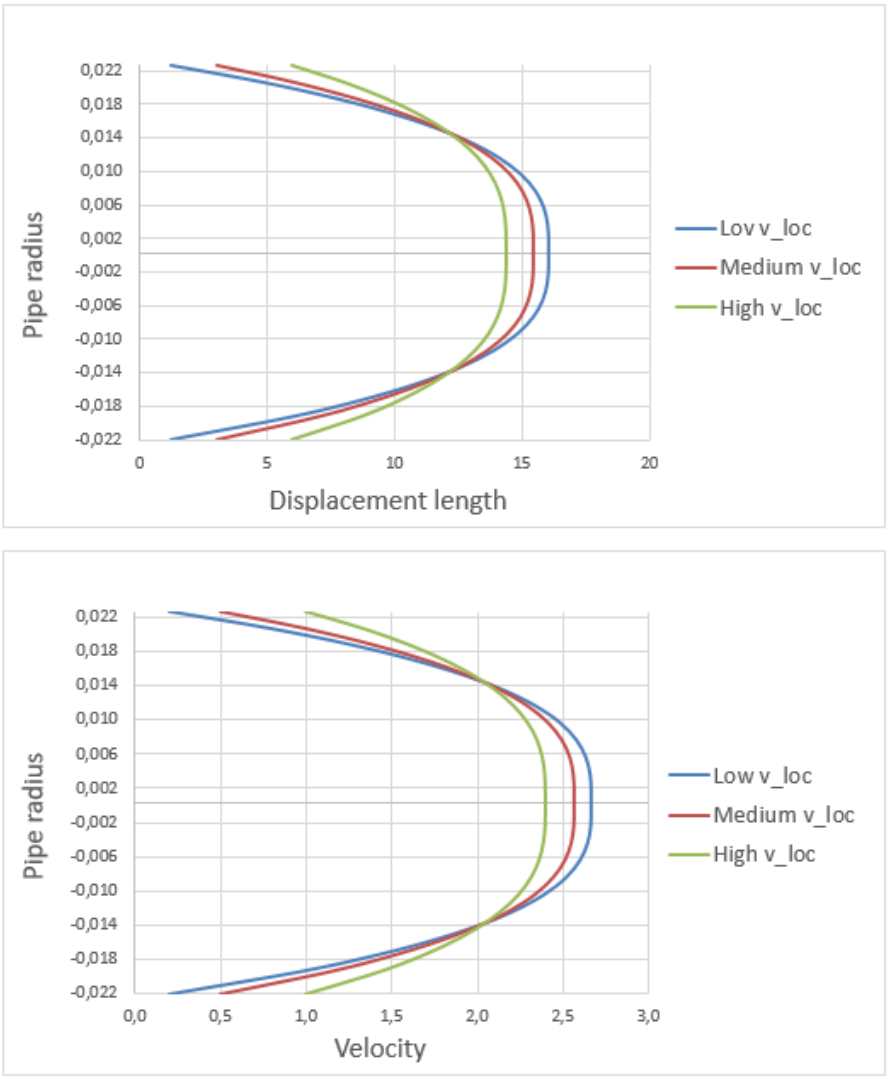

Figure 3.7: *Herschel-Bulkley simulations showing displacement profiles (upper) and velocity profiles (lower). Local velocity as varying parameter.*

The second simulation type is shown in Figure 3.8. This figure shows the displacement profiles and velocity profiles obtained by the Herschel-Bulkley model when varying flow rate. The graphs shown in the displacement profile plot have the same shape as the graphs appearing in the velocity profile plot for the same reason as explained in the previous paragraph. The blue line, representing the lowest rate, is observed to be flatter and have less maximum velocity compared to the lines representing higher flow rate. This is expected since higher flow rate in turn increases the total displaced volume when time is held constant or equal for all the simulations.

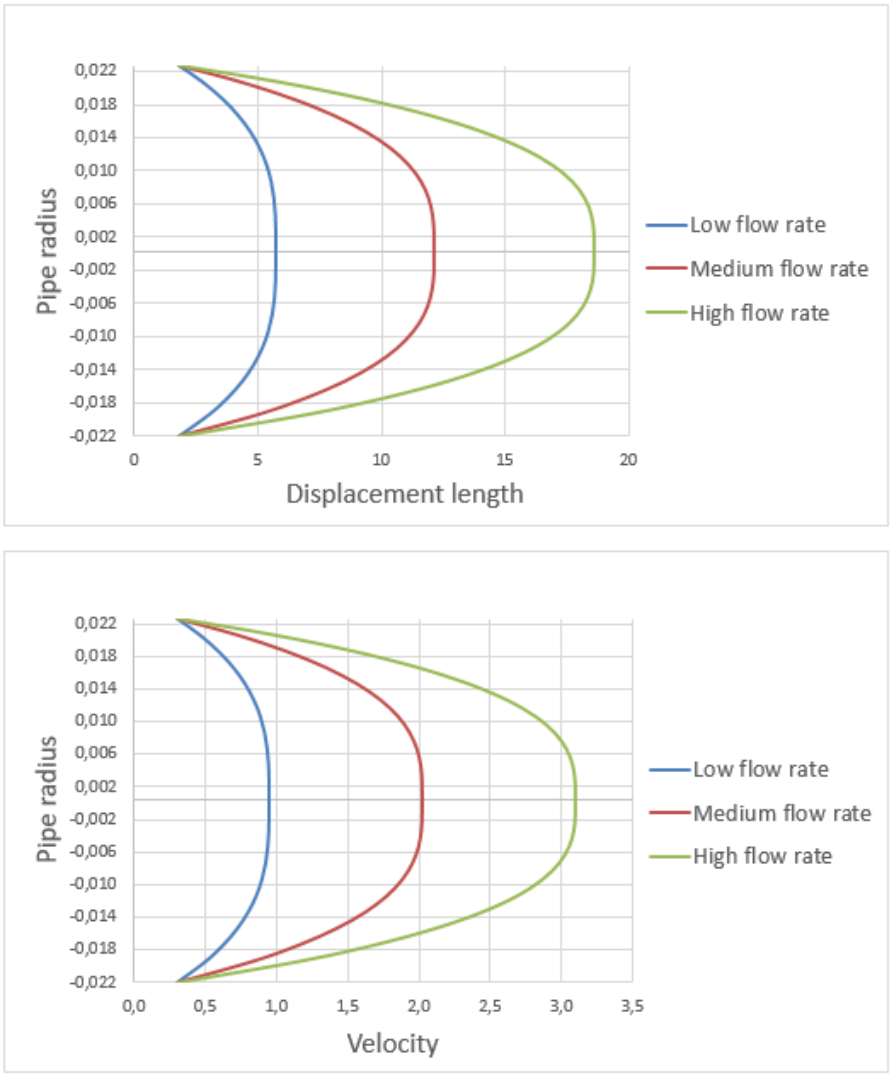

Figure 3.8: *Herschel-Bulkley simulations showing displacement profiles (upper) and velocity profiles (lower). Flow rate as varying parameter.*

Figure 3.9 shows the displacement profile and velocity profile for three different scenarios, varying time and keeping all the other variables constant. From the plot presenting the displacement profiles it can be observed a larger volume displaced for the largest time value compared to the lines representing lesser time values. This is easily explained by the fact that a larger volume has been transported when more time has gone by, keeping the flow rate constant. Comparing the displacement profile plot to the velocity profile plot shown in Figure 3.9, a big difference can be observed. In the displacement profile three different lines are shown. In the velocity profile there are three lines but they overlap and appear as only one line. The overlap is due to the fact that the velocity profile function, $v(r)$, is not a function of time. Therefore, it will not change keeping all variables constant except time.

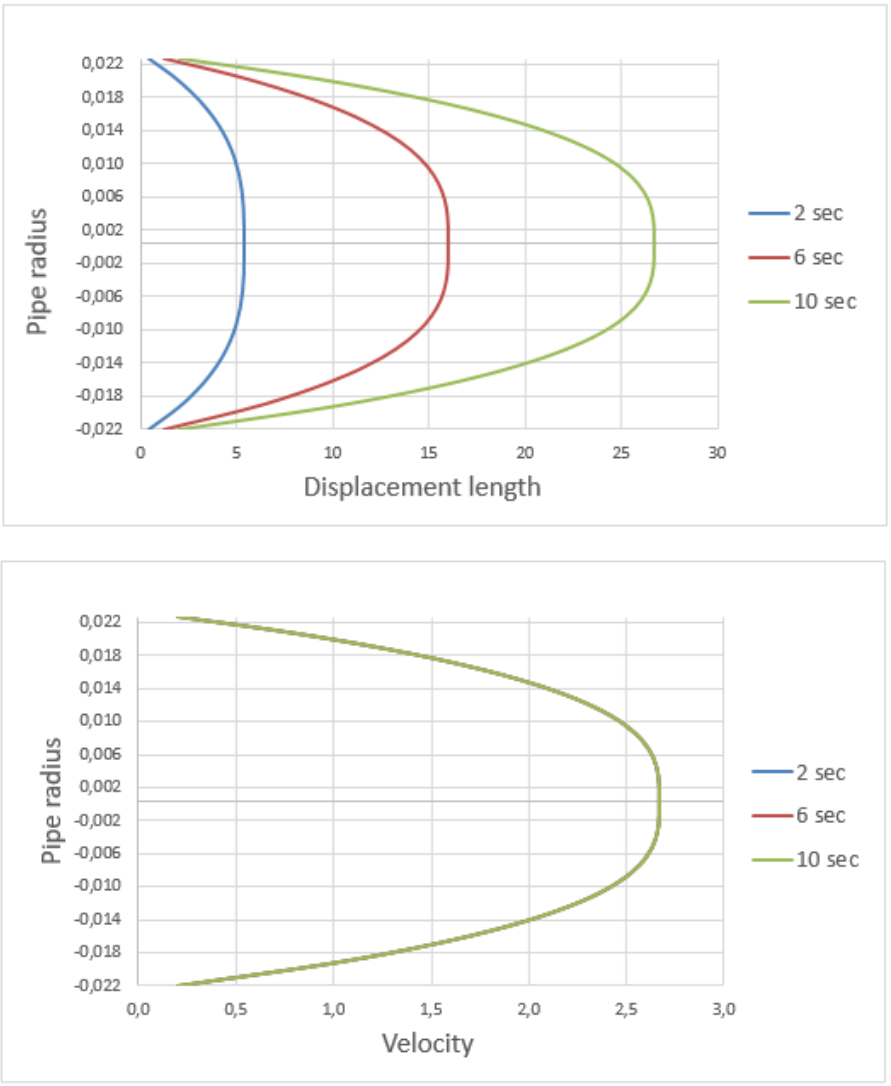

Figure 3.9: *Herschel-Bulkley simulations showing displacement profiles (upper) and velocity profiles (lower). Time as varying parameter.*

3.5.2 Volumetric displacement efficiency

Volumetric displacement efficiency is, as explained in section 3.2, a factor describing the amount of the initial pipe volume of displaced fluid that has been displaced. Put in other words, the volumetric efficiency factor gives us a factor telling us how much of the entire pipe volume is filled with the displacing fluid.

Figure 3.10 displays three graphs in the same plot, each one representing a local velocity different from the others, keeping all other variables constant. The plot clearly shows that a variation in local velocity affects the volumetric displacement efficiency. Higher local velocity results in better volumetric displacement efficiency. Knowing the flow rate is held constant for the three simulations, we can expect the volumetric efficiency to be equal for the three

simulations until one of them has encountered breakthrough at the pipe end. This expectation is confirmed by the observation of the three graphs overlapping at the beginning until about $t = 0.7sec$. Having the velocity profiles and displacement profiles shown in Figure 3.7 in mind, we know that higher local velocity results in a flatter velocity profile. A consequence of this observation is in turn that a high volumetric efficiency will occur faster compared to a less flat velocity profile resulted by a lower local velocity. This is also shown in Figure 3.10 by the green line approaching a volumetric efficiency of 1 faster than the other graphs.

In Figure 3.10 the blue line represents the lowest local velocity. The local velocity for this simulation is set to be 0 m/s. A local velocity equal to 0 means that there is no flow closest to the wall, representing no-slip condition. In theory, having no-slip will result in never reaching full displacement, or a volumetric displacement efficiency of 1.

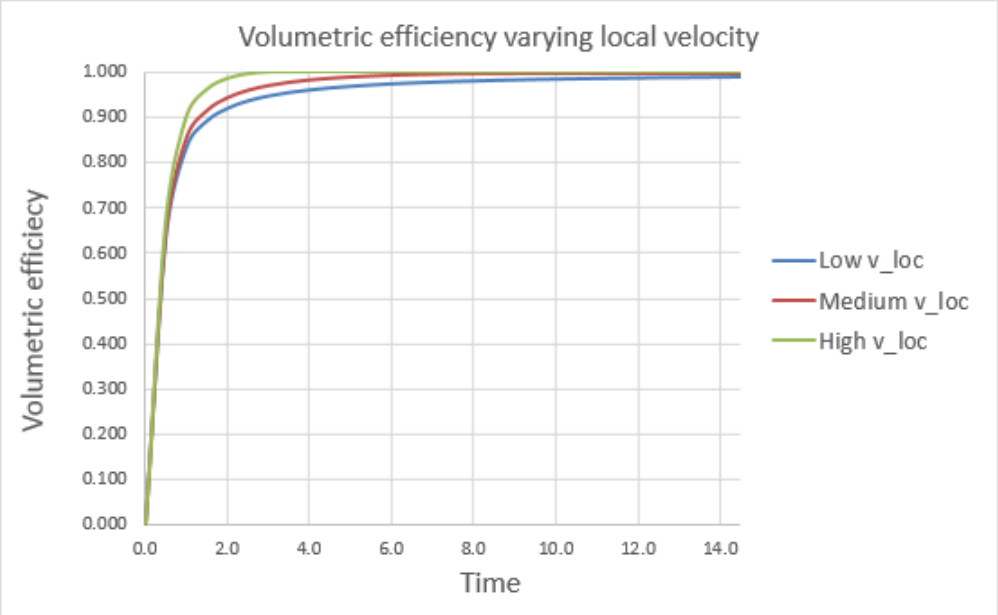

Figure 3.10: *Herschel-Bulkley simulations showing volumetric efficiency graphs. Local velocity as varying parameter.*

It is expected that a high flow rate will result in a high volumetric efficiency factor, and a low flow rate will result in a lower volumetric efficiency factor, keeping the other variables constant. Figure 3.11 contains three simulations only varying flow rate. The green line, representing the highest flow rate has the highest volumetric efficiency over the entire time interval. This observation supports our expectation. The local velocities are set to the same value for all three simulations, resulting in full displacement at the same time. This can to some extent be observed in the plot by the fact that the three simulations seem to overlap towards the end.

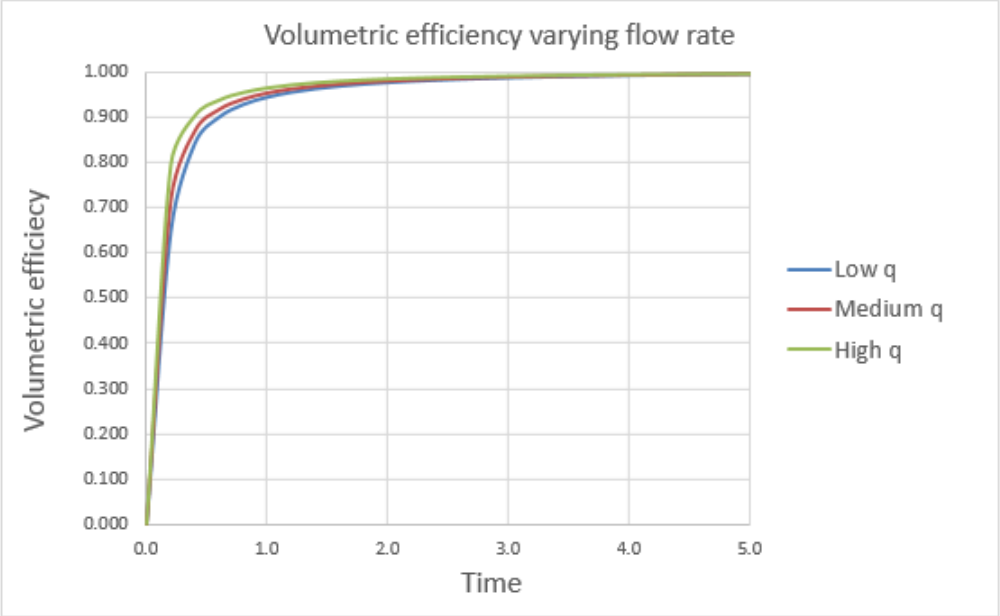

Figure 3.11: *Herschel-Bulkley simulations showing volumetric efficiency graphs. Flow rate as varying parameter.*

As observed and explained from Figure 3.11 the volumetric efficiency factor will increase over time. Also, a higher flow rate will result in a better displacement efficiency. Figure 3.12 shows these observations clearly. The graph representing $t = 0.6sec$ results in better volumetric efficiency factor compared to the one based on values at 0.2 seconds for all flow rates simulated. This observation supports our first claim. The second claim being, higher flow rate will result in a better displacement efficiency, is supported by both graphs and their positive trend with increasing flow rate.

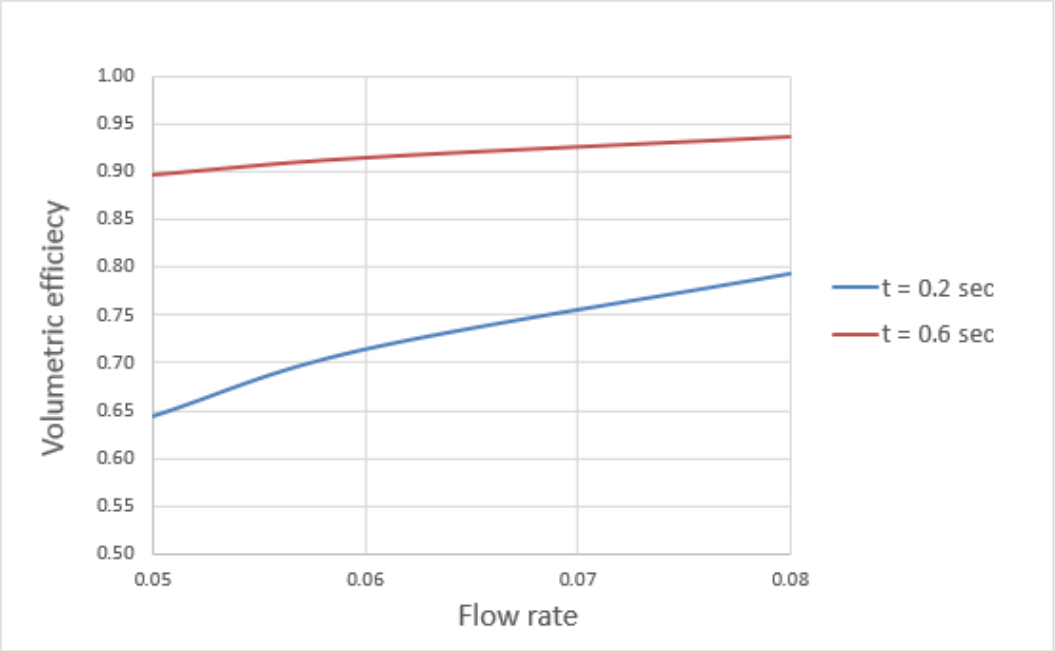

Figure 3.12: *Volumetric efficiency factors varying flow rate at two different times;* $t = 0.2s$ *and* $t = 0.6s$.

3.5.3 Comparison of Herschel-Bulkley and Newtonian simulations

This subsection compares simulations done with both the Herschel-Bulkley model and the Newtonian model. Input parameters used in the two models are set to be equal to investigate if, or how, the two models differ from each other.

Figure 3.13 shows a comparison between the Herschel-Bulkley model and the Newtonian model, both simulating the displacement profile. Two different local velocities are used for both models. The Herschel-Bulkley model show a flatter displacement profile compared to the simulation done with the Newtonian model. The flat displacement front appears because the Herschel-Bulkley model consists of two parts; a flat plug in the middle and a parabolic shape near the wall. The flat shape will in turn result in a shorter maximum displacement length compared to the Newtonian model since the other parameters, such as flow rate and time, are held constant. We can see from Figure 3.13 that the maximum displacement length appearing in the Herschel-Bulkley simulation is shorter than the one appearing in the Newtonian simulation.

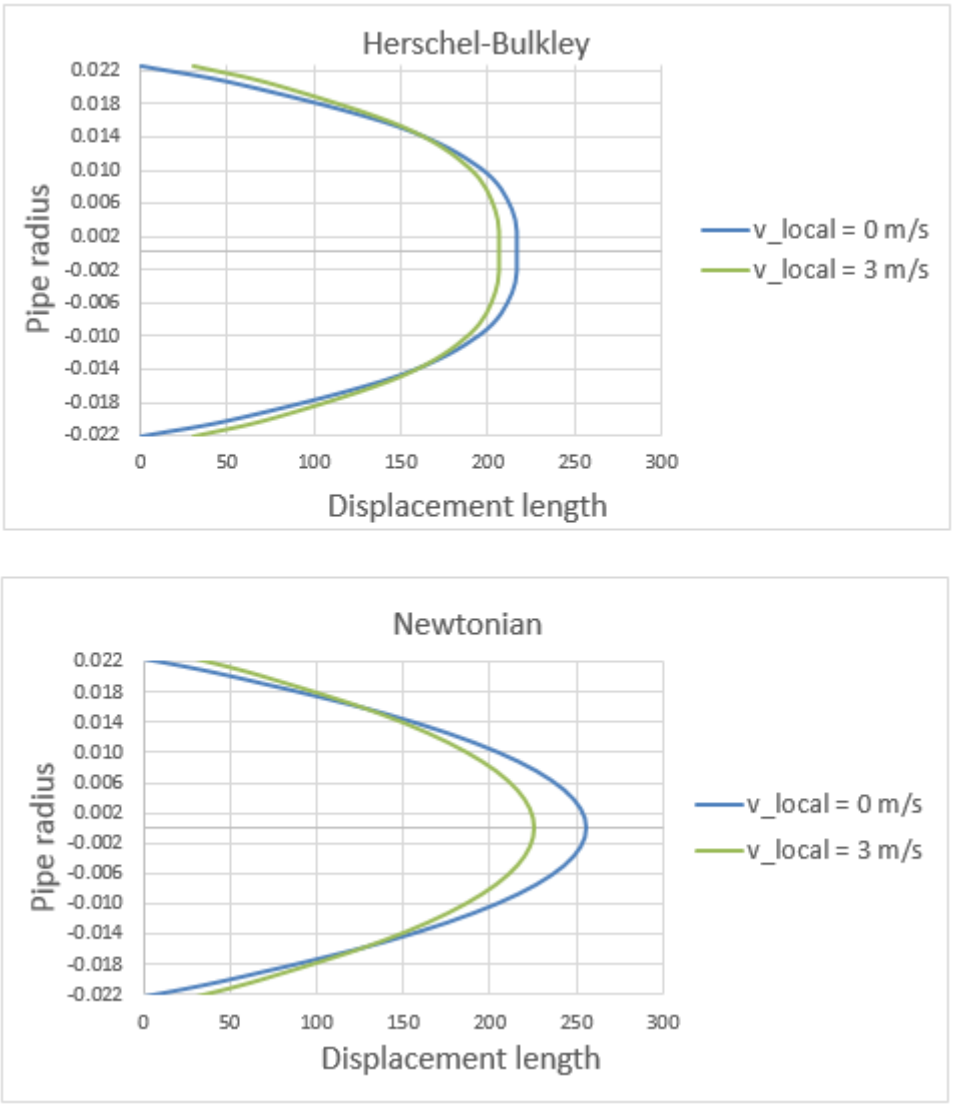

Figure 3.13: *Displacement profiles for Herschel-Bulkley (upper) and Newtonian (lower).Local velocity as varying parameter.*

Displacement profiles with flow rate as varying parameter are shown in Figure 3.14. Isolated, the two models behave as expected. Comparing the two model simulations to each other we observe the same as we did in Figure 3.13. The Herschel-Bulkley simulation results in a flatter displacement profile with a plug flow in the center and a parabolic trend towards the pipe wall. The Newtonian model results in a parabolic trend over the entire pipe radius. As expected, the Newtonian model results in the longest maximum displacement lengths.

Figure 3.15 shows volumetric efficiency simulations for both Herschel-Bulkley and the Newtonian model. The two plots are very similar, but some differences are present. Until the displacement front reaches pipe end, the volumetric efficiencies are equal. The reason for this observation is explained in section 3.4. After breakthrough, the volumetric displacement

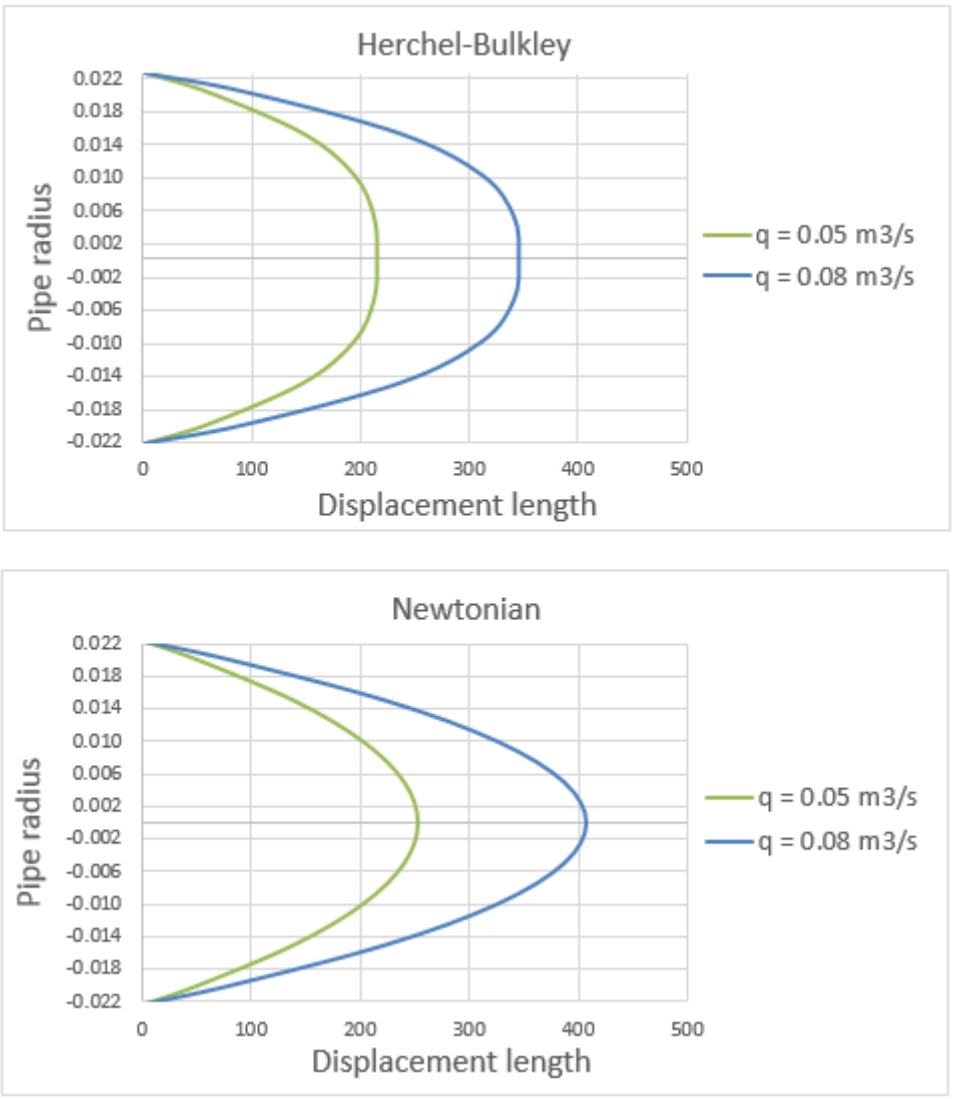

Figure 3.14: *Displacement profiles for Herschel-Bulkley (upper) and Newtonian (lower). Flow rate as varying parameter.*

for the Newtonian simulation will be of a smaller value than the Herschel-Bulkley simulation. This is due to the differences in velocity profiles, and will last until the local velocity reaches pipe end, resulting in full displacement. The claimed differences are hard to see directly from the plots, but Table 3.6 clearly demonstrates them. The table shows that the volumetric efficiencies are equal for $0.0s$ and $0.3s$ (cells marked blue). For these time values, the displacement front has not yet reached pipe end in our simulations. From $0.6s$ and on, the Newtonian volumetric efficiency values are smaller compared to the values obtained by the Herschel-Bulkley model. An exception is present for the simulations done with local velocity equal to $3m/s$. Equal local velocity for the two models will result in full displacement at the same point in time. For the simulation using $v_{loc} = 3m/s$ this happens at $t = 3.3$, resulting in

a volumetric efficiency of 1 (cells marked red).

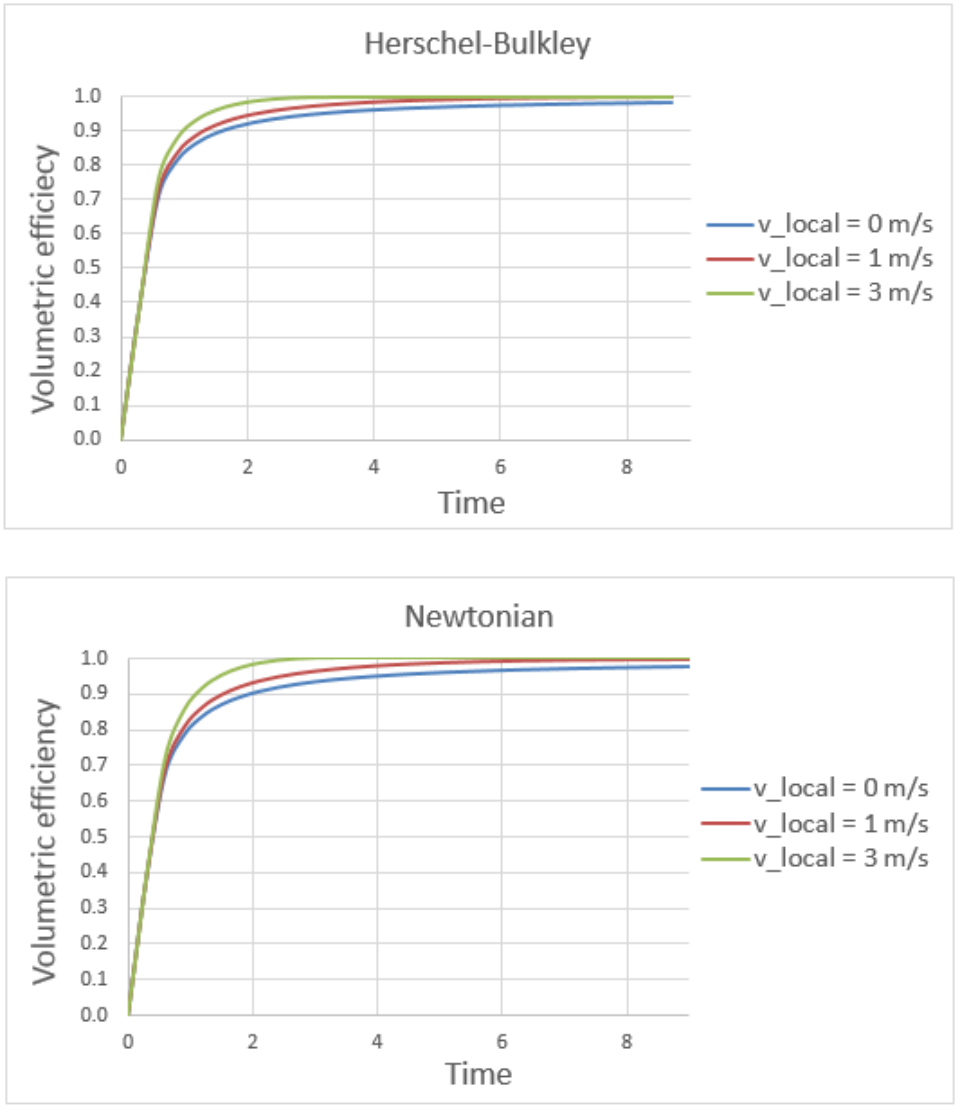

Figure 3.15: *Volumetric efficiency plots for Herschel-Bulkley (upper) and Newtonian (lower). Local velocity as varying parameter.*

Figure 3.16 visualize volumetric efficiency simulations varying flow rate. The main observable difference between the two model simulations presented in these plots are the bending trends towards the horizontal direction. The bending in the Hershel-Bulkley plot looks sharper compared to the Newtonian plot. This trend appears due to the plug flow resulting in a flat velocity profile in the Herschel-Bulkley model. Table 3.7 shows the values used in Figure 3.16. The cells marked blue represent equal values for the Herschel-Bulkley and Newtonian model, suggesting breakthrough has not yet happened. It is clearly shown that a higher flow rate will result in earlier breakthrough. As seen from both Figure 3.16 and Table 3.7, none of the simulations encounter full displacement.

Table 3.6: *Volumetric efficiency values for the Herschel-Bulkley and Newtonian model at different time steps. The comparisons are done with three different local velocities.*

	v_local = 0m/s		v_local = 1 m/s		v_local = 3 m/s	
Time	Volumetric efficiency		Volumetric efficiency		Volumetric efficiency	
	HB	NT	HB	NT	HB	NT
0.0	0.0000	0.0000	0.0000	0.0000	0.0000	0.0000
0.3	0.3913	0.3913	0.3913	0.3913	0.3913	0.3913
0.6	0.7114	0.6806	0.7288	0.6946	0.7635	0.7219
0.9	0.8156	0.7871	0.8382	0.8095	0.8820	0.8540
1.2	0.8641	0.8403	0.8888	0.8666	0.9339	0.9165
1.5	0.8923	0.8722	0.9179	0.9006	0.9618	0.9512
1.8	0.9108	0.8935	0.9369	0.9230	0.9782	0.9720
2.1	0.9239	0.9087	0.9501	0.9389	0.9882	0.9848
2.4	0.9336	0.9201	0.9598	0.9506	0.9943	0.9927
2.7	0.9411	0.9290	0.9672	0.9596	0.9979	0.9972
3.0	0.9471	0.9361	0.9730	0.9666	0.9996	0.9994
3.3	0.9520	0.9419	0.9776	0.9723	1.0000	1.0000
3.6	0.9561	0.9468	0.9813	0.9769	1.0000	1.0000
3.9	0.9595	0.9509	0.9844	0.9807	1.0000	1.0000
4.2	0.9624	0.9544	0.9870	0.9838	1.0000	1.0000
4.5	0.9649	0.9574	0.9891	0.9865	1.0000	1.0000
4.8	0.9672	0.9601	0.9909	0.9887	1.0000	1.0000
5.1	0.9691	0.9624	0.9925	0.9906	1.0000	1.0000
5.4	0.9708	0.9645	0.9938	0.9922	1.0000	1.0000
5.7	0.9724	0.9664	0.9949	0.9936	1.0000	1.0000
6.0	0.9738	0.9681	0.9958	0.9948	1.0000	1.0000
6.3	0.9750	0.9696	0.9966	0.9958	1.0000	1.0000
6.6	0.9762	0.9710	0.9973	0.9966	1.0000	1.0000
6.9	0.9772	0.9722	0.9979	0.9974	1.0000	1.0000
7.2	0.9782	0.9734	0.9984	0.9980	1.0000	1.0000
7.5	0.9791	0.9744	0.9988	0.9985	1.0000	1.0000
7.8	0.9799	0.9754	0.9991	0.9989	1.0000	1.0000
8.1	0.9806	0.9763	0.9994	0.9992	1.0000	1.0000
8.4	0.9813	0.9772	0.9996	0.9995	1.0000	1.0000
8.7	0.9820	0.9780	0.9998	0.9997	1.0000	1.0000

The volumetric efficiency differences between the two models are plotted in Figure 3.17. This figure shows the difference between the two models when $v_{local} = 1m/s$. The sharp turn upwards at $t = 0.55s$ represent the breakthrough of the Newtonian model. Following the turn is a dramatic increase in efficiency difference. Since the Herschel-Bulkley displacement front is flatter, the front will reach pipe end later, hence the dramatic increase in efficiency difference. The peak at about $t = 0.65s$ represents breakthrough for the Herschel-Bulkley model. This peak is followed by a decrease in efficiency difference until the pipe is fully

Table 3.7: *Volumetric efficiency values for the Herschel-Bulkley and Newtonian model at different time steps. The comparisons are done with three different flow rates.*

	q = 0.01 m3/s		q = 0.02 m3/s		q = 0.05 m3/s	
Time	Volumetric efficiency		Volumetric efficiency		Volumetric efficiency	
	HB	NT	HB	NT	HB	NT
0.0	0.0000	0.0000	0.0000	0.0000	0.0000	0.0000
0.2	0.1304	0.1304	0.2609	0.2609	0.6447	0.6185
0.4	0.2609	0.2609	0.5218	0.5215	0.8400	0.8132
0.6	0.3913	0.3913	0.7201	0.6876	0.8976	0.8780
0.8	0.5218	0.5218	0.8013	0.7706	0.9255	0.9104
1.0	0.6542	0.6255	0.8471	0.8204	0.9420	0.9299
1.2	0.7284	0.6946	0.8766	0.8535	0.9529	0.9428
1.4	0.7771	0.7439	0.8972	0.8772	0.9606	0.9520
1.6	0.8119	0.7808	0.9125	0.8949	0.9663	0.9589
1.8	0.8381	0.8095	0.9242	0.9086	0.9707	0.9643
2.0	0.8586	0.8324	0.9335	0.9196	0.9743	0.9686
2.2	0.8751	0.8510	0.9411	0.9286	0.9772	0.9721
2.4	0.8887	0.8666	0.9473	0.9360	0.9796	0.9750
2.6	0.9000	0.8797	0.9526	0.9423	0.9816	0.9775
2.8	0.9097	0.8909	0.9571	0.9477	0.9833	0.9796
3.0	0.9179	0.9006	0.9609	0.9523	0.9848	0.9814
3.2	0.9251	0.9090	0.9643	0.9564	0.9861	0.9830
3.4	0.9313	0.9164	0.9672	0.9599	0.9872	0.9844
3.6	0.9369	0.9230	0.9698	0.9631	0.9882	0.9856
3.8	0.9418	0.9289	0.9722	0.9659	0.9891	0.9867
4.0	0.9461	0.9341	0.9742	0.9684	0.9899	0.9877
4.2	0.9501	0.9389	0.9761	0.9707	0.9907	0.9886
4.4	0.9536	0.9432	0.9778	0.9727	0.9913	0.9894
4.6	0.9569	0.9471	0.9793	0.9746	0.9919	0.9901
4.8	0.9598	0.9506	0.9807	0.9763	0.9925	0.9907
5.0	0.9625	0.9539	0.9820	0.9779	0.9930	0.9914
5.2	0.9649	0.9568	0.9832	0.9793	0.9934	0.9919
5.4	0.9672	0.9596	0.9842	0.9806	0.9938	0.9924
5.6	0.9693	0.9621	0.9852	0.9818	0.9942	0.9929
5.8	0.9712	0.9645	0.9861	0.9830	0.9946	0.9933

displaced.

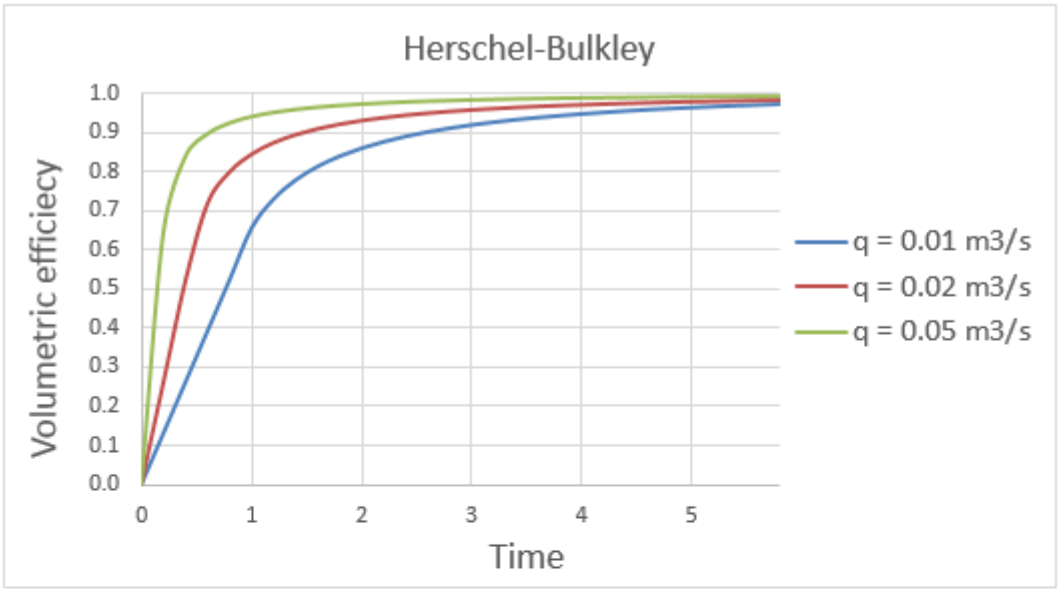

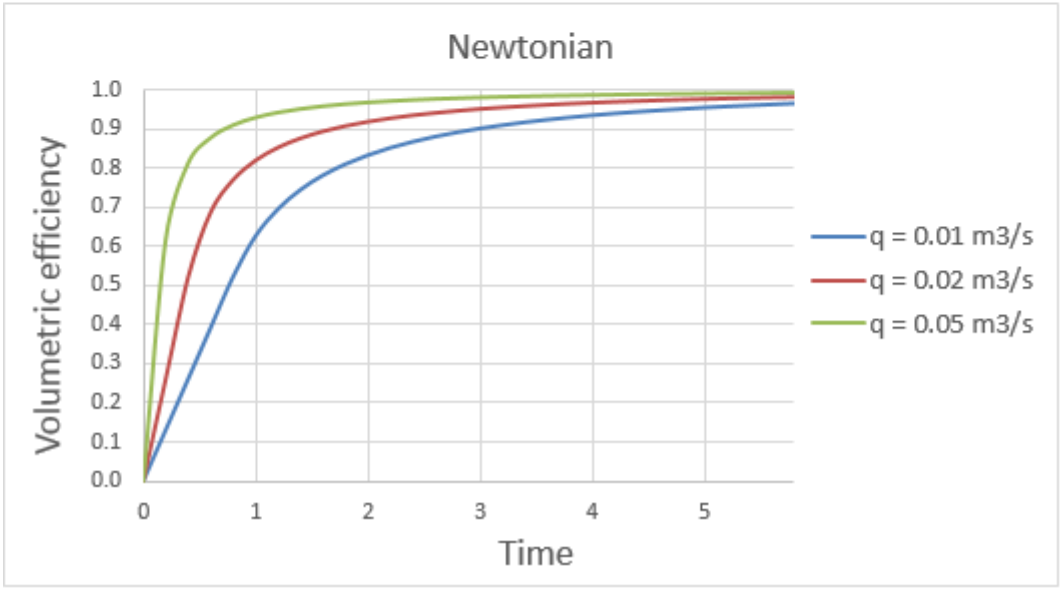

Figure 3.16: *Volumetric efficiency plots for Herschel-Bulkley (upper) and Newtonian (lower). Flow rate as varying parameter.*

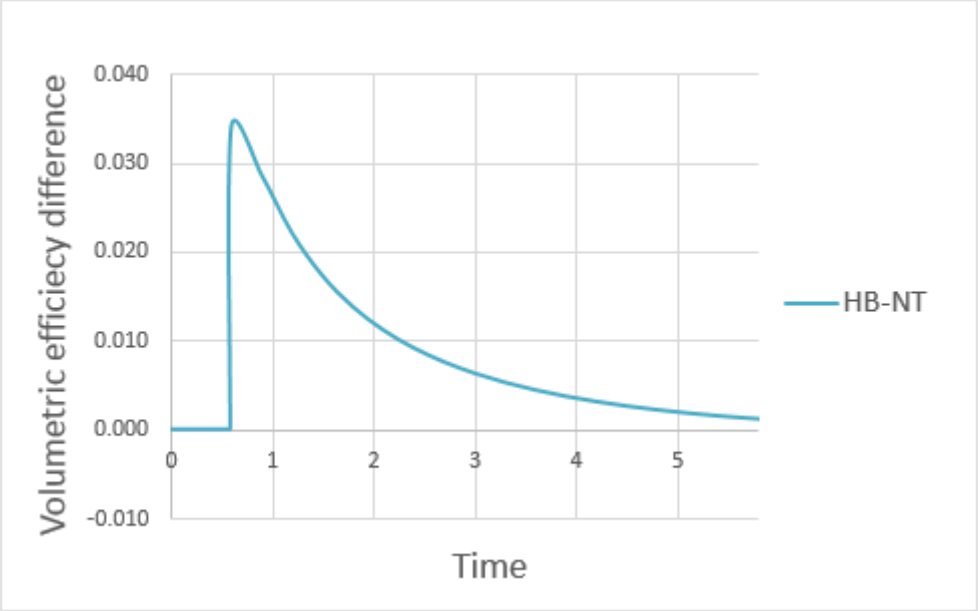

Figure 3.17: *Difference in volumetric efficiency factor for Herschel-Bulkley and the Newtonian model. All parameters are set to be equalfor the two models.*

4. *Experimental work*

This thesis is built on the previous project from autumn 2016. The experimental setup used is the same one, but with some alterations. Therefore some parts of this chapter are from the autumn project (Giil and Johansen, 2016).

Experimental and theoretical investigations could possibly reveal the effect of pipe roughness on displacement efficiency of primary cement job. No-slip condition characterizes viscous flow in smooth pipes in which velocity is zero on solid surfaces. Pipe roughness tests were planned performed on pipes with different degrees of roughness to investigate pipe wall boundary conditions by inducing local turbulence. The objective was to investigate if this local turbulence caused a slipping boundary layer at the pipe wall. The roughness depth was 1 mm (2% of pipe diameter) for all rough pipes, to meet the criteria of a roughness comparable to 1% of the pipe diameter stated in chapter 2. The variation in roughness was made with variation in density of spiral windings per pipe length. For the three different degrees of roughness several repetitive runs were planned to secure consistency in the results. The results were then matched to the theoretical model to determine the values of the empirical constants.

4.1 Type of experiments

4.1.1 Displacement tests in small scale flow loop

Our main and original objective was to simulate and perform flow tests in a small scale flow loop. It is characterized by being limited to test displacement efficiency for pipe flow as opposed to annular flow. However, the surface roughness of the pipes used could be varied, and thus the displacement efficiency could be used to estimate the local slip velocity. The set-up for this flow loop is explained in detail later in this chapter.

4.1.2 Displacement tests in large scale flow loop

We have, in addition to our initial small scale project, been invited to work with SINTEF Petroleum at the "Drilling and Well Centre for Improved Recovery" (*DrillWell*, 2016) program 3, project 6: "Cementing Irregular Wellbore Geometries". The setup of the flow loop that is used is similar to our, but with some important differences. The flow loop is larger and the geometry is annular. It is also possible to vary the eccentricity and rotate the pipe acting as the casing string. The applied fluids are prepared to have rheological properties similar to a cement and spacer used on the Norwegian Continental Shelf (Ytrehus et al., 2017).

The objectives of the project is to investigate how the displacement is affected by wash outs, varying angle, varying eccentricity and rotation of the casing string. We aim to compare the results from this project to the results obtained from our small scale flow loop project. To make the comparison more interesting, we plan to use the same fluids for both experiments. These large scale tests were run in the autumn of 2016, and relevant comparison of the two different tests will take place in this report.

4.2 Fluid properties

Fluid information such as rheological properties, composition and mixing procedure is presented in this section for all fluids used during testing. The compositions and mixing procedure of the different fluids are presented, enabling others to reproduce the fluids if desirable.

4.2.1 Fluids used in small scale flow loop

Laponite-fluid The Laponite-fluid consists of water, Laponite RD Powder and Xantan gum. Laponite is a synthetic clay. It is widely used in different industries and consumer products to obtain preferred rheological properties of fluids, most often to develop a thixotropic rheology in water based solutions (Bayville Chemical Supply Company Inc., 2014). The platelets of laponite synthetic clay has dimensions of typically around 20-30 nm in length and 0.92 nm in width (Perotti et al., 2011). In our fluid, Laponite RD from BYK Additives and Industries were used. According to BYK Additives and Industries the Laponite RD had properties as shown in Table 4.1. It is a layered silicate manufactured from naturally occurring inorganic mineral

sources.

Table 4.1: *Typical properties of Laponite RD (*Laponite RD*, Technical Data Sheet, 2013)*

Characteristics	Specifications
Appearance	Free flowing white powder
Bulk Density	1000 kg/m^3
Surface Area (BET)	370 m^2/g
pH (2 % suspension)	9.8
Chemical Composition (dry basis) SiO_2	59.5 %
Chemical composition (dry basis) MgO	27.5 %
Chemical composition (dry basis) Li_2O	0.8 %
Chemical composition (dry basis) Na_2O	2.8 %
Chemical composition (dry basis) Loss on ignition	8.2 %
Gel strength	22 g min QA Test Code: ELP-L-1H

According to (Batista et al., 2011), Laponite RD is a synthetic trioctahedral hectorite composed of two tetrahedral silica sheets and a central octahedral sheet. Dispersed in water, disk shaped layers occur similar to natural clay. When mixed with water, laponite behave similar to some natural clays in terms of thixotropy. During static conditions the fluid is thick, while it becomes less viscous when exposed to shaking, shearing or other types of stress. The viscosity of the fluid is also dependent on the laponite concentration. We have observed the effect of thixotropy both during storing of the fluid and in the lab where viscosity tests have been performed. Lab measurements from two fluid samples are shown in Figure 4.1 and 4.2. The viscosity tests were performed in cooperation with SINTEF and a Phd. student from NTNU. Further information about the fluids and procedures can be found in Werner et al. (2017). General procedure for rheology measurements with Fann viscometer is shown in Appendix F.

The graphical representations of viscosity illustrated in both Figure 4.1 and Figure 4.2 show that the Fann readings are higher after 24 hours of resting compared to readings done right after mixing. This observation clearly shows that the viscosity of the fluid is time dependent, supporting the thixotrophy claim. These tests were performed with and without preshear, and show the same trend. In this research, preshear consists of 10 minutes in the Fann viscometer with 600 RPM.

To get the desired rheological properties a mixing recipe was developed (Lund, 2016) with a target mass of 1000 kg. This is also described in Giil and Johansen (2016). The necessary laponite concentration was 1.5 w%. The mixing procedure of laponite and water was very time consuming, and the practice developed by Lund (2016) required several days to fullfill

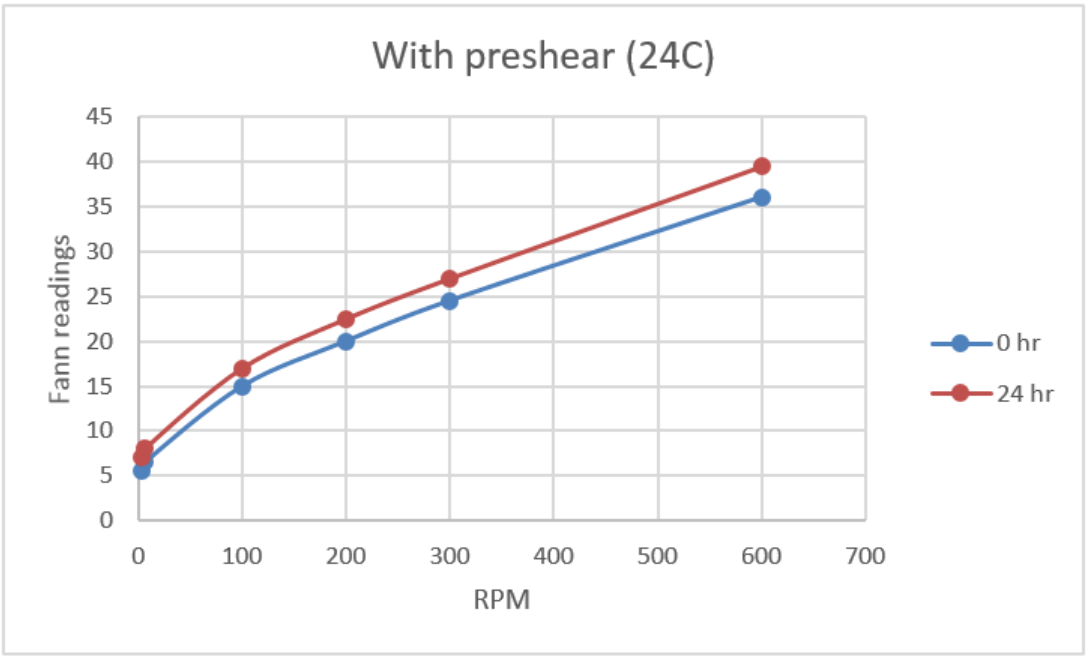

Figure 4.1: *Fann measurements of a fluid sample after resting for 0 hours and 24 hours.*

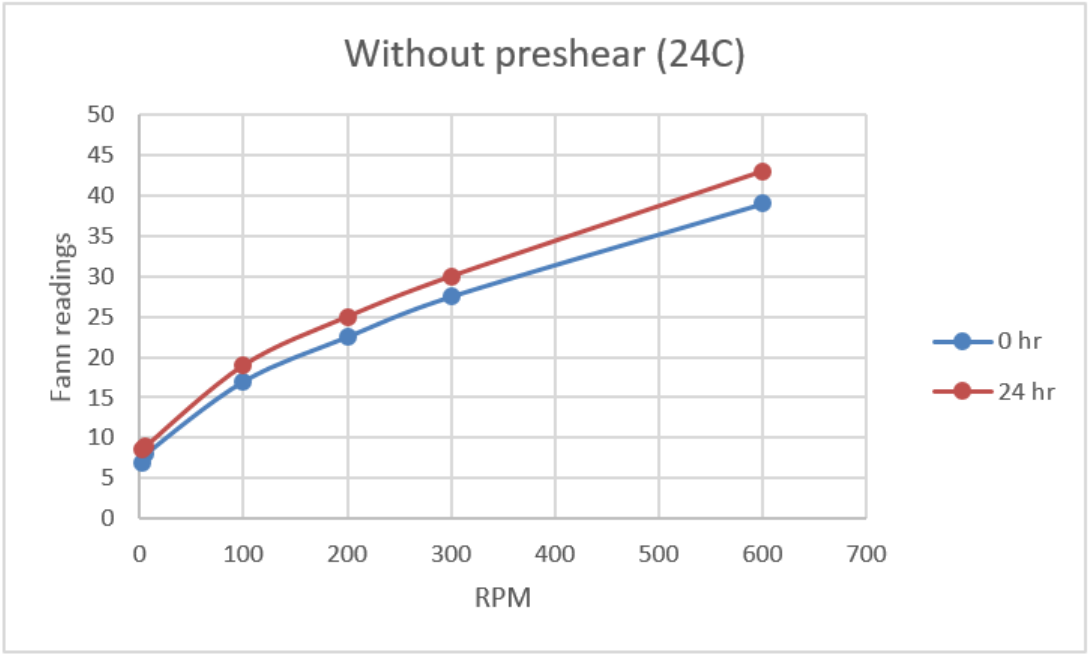

Figure 4.2: *Fann measurements of a fluid sample after resting for 0 hours and 24 hours.*

the process. First the dry laponite had to be pre-hydrated, with 1.5 kg added to 20 kg of hot water, and mixed with MeecTools Cement Mixer 1220W. This is a commercially available hand mixer often used for mixing small batches of concrete. To get the required laponite concentration of 1.5 w% of a 1000 kg target mass, 10 of these sub-batches had to be made. The sub-batches was left overnight for pre-hydration before next step was performed.

The pre-hydrated laponite was then mixed with the rest of the water. Each batch was

mixed with 78.5 kg of free water to get 10 batches of 100 kg each. The mixing was done using MeecTools Cement Mixer 1220W. Before transferring to storage tank the fluid had to be mixed at high speed with Waring blender, in batches of 4 l each to ensure good mixing of accumulated laponite powder balls that still could be present. A color, metyl blue, was added to the laponite for good contrast during the displacement experiments.

Xantan gum where then added to small portions of the mixture in the lab, and the viscosity increase where monitored. A 0.1 w% of Xantan gum where found to give the preferred viscosity profile, and the final composition is shown in Table 4.2. The Fann measurements of the final composition for the Laponite-fluid are shown in Figure 4.3.

The Laponite-fluid is used as the displaced fluid in the large scale test loop. In the small scale test loop it is used as a fluid being displaced by CMC-fluid, and as a fluid displacing an oil based spacer fluid.

Table 4.2: *Final composition of the Laponite-fluid.*

Component	w%
Water	98.4
Laponite	1.5
Xantan-gum	0.1
Methyl blue	neglible

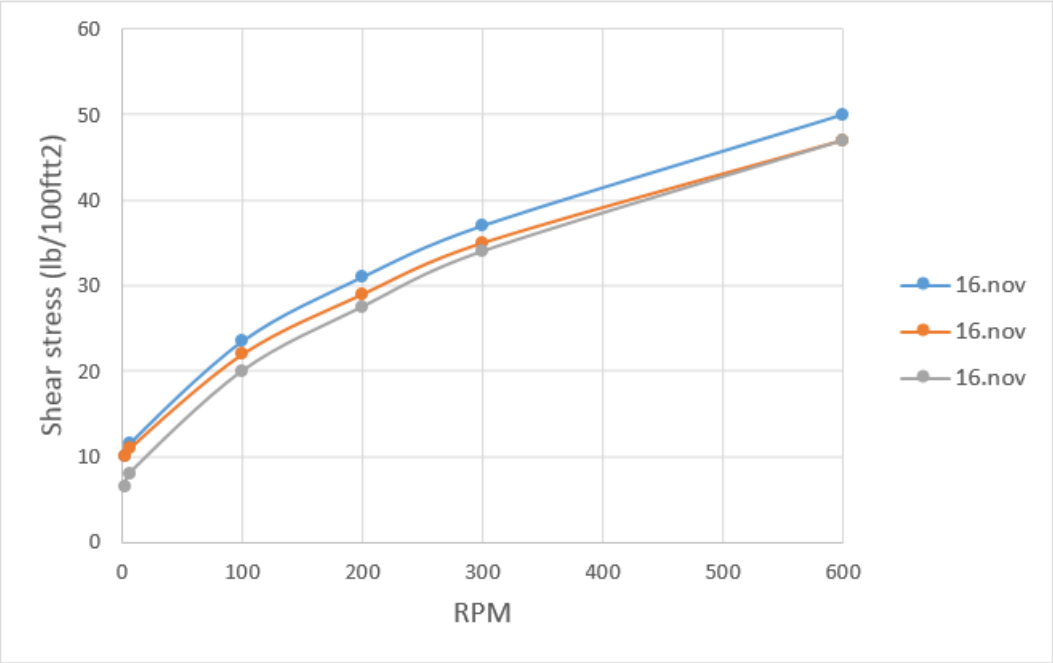

Figure 4.3: *Fann measurements for the final composition of the Laponite-fluid. T=24°C.*

CMC-fluid The CMC-fluid consisted of water, sucrose, CMC, NaCl, biocide, soda ash and uranine. This is also described in Giil and Johansen (2016). Sucrose is regular white household sugar, and in the fluid it was used as a weighting agent. CMC is Carboxymethyl cellulose, and it is often (and also here) used as a viscosifier. NaCl was added to increase the conductivity of the fluid, as the displacement efficiency was measured with electrodes measuring the conductivity. A biocide is a general term describing a chemical substance designed to control unwanted organisms, such as bacterial growth. The biocide used in this fluid composition was MB-5111 from MI-Swaco. Soda ash is sodium carbonate, a water soluble salt, and it was added to adjust the pH of the fluid. The Uranine tracer salt was used to give the fluid a characteristic yellow-green fluorescent color. 1 g of uranine is enough for coloring 100 m^3 of water, and the 0.1 g used in ~ 2 m^3 of CMC-fluid gave a very distinct color.

The mixing procedure for the CMC-fluid was also developed by Lund (2016). The procedure was based on mixing two sub-batches in parallel, and mixing them together afterwards. Sub-batch A was 14.7 kg of sugar dissolved in 20 kg of hot water. MeecTools Cement Mixer 1220W was used for stirring. Sub-batch B consisted of all the dry chemicals, water, and biocide. First the dry chemicals were mixed in a bucket, 0.6 kg CMC, 0.72 kg NaCl and 0.3 kg soda ash. Then the dry chemicals were mixed with water, 1/4 of the chemicals and 2 kg water each time, at high speed in Waring blender. 0.06 kg biocide was then added, and the rest of the water (15.62 kg). Sub-batch A was transferred into the bucket with sub-batch B and they were mixed before transferred to the IBC tank. The recipe was adjusted a bit during the mixing to obtain the desired rheological properties, and the final composition is shown in Table 4.3. Fann measurements were done, using three fluid samples from the final CMC-fluid composition. The three fluid samples represent the same IBC tank, but are taken from different positions such as top, center and bottom of the tank. Results from the fann measurements are shown in Figure 4.4. Figure 4.5 presents Fann measurements from the final composition of both the Laponite- and CMC-fluid together.

The CMC-fluid was used as the displacing fluid in the large scale flow loop. In the small scale setup it was used as the displacing fluid for experiments with Laponite-fluid as the displaced fluid.

Table 4.3: *Composition of the CMC-fluid.*

Component	w%
Water	73.17
Sucrose	24.28
CMC	0.79
NaCl	1.23
Biocide	0.10
Soda ash	0.42
Uranine	negligible

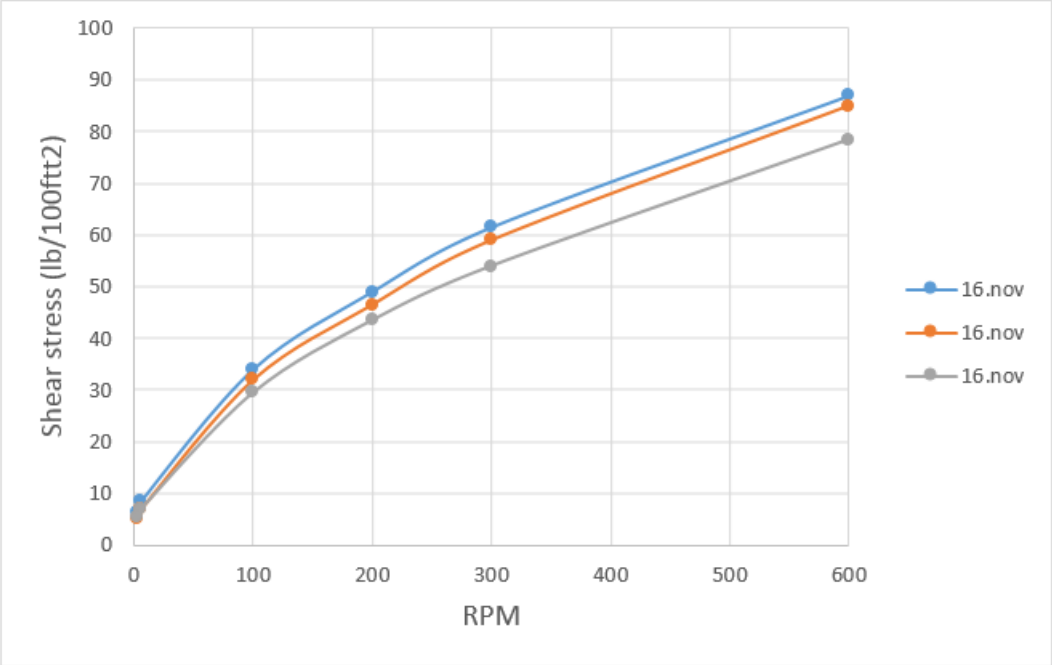

Figure 4.4: *Fann measurements for the final composition of the CMC-fluid. T=24°C.*

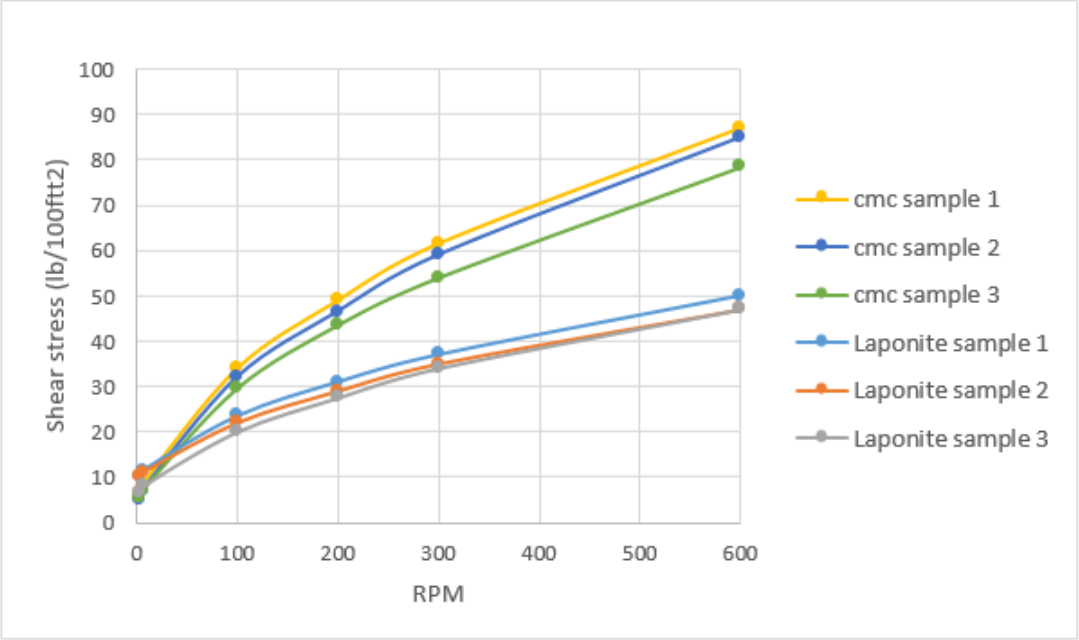

Figure 4.5: *Fann measurements for CMC- and Laponite-fluid. T=24°C.*

Oil based fluid An oil based fluid with a viscosity (μ_{eff}) of 17.5 cp was developed to be used as a fluid being displaced by the Laponite-fluid. It was developed by mixing Exxsol D60 with Mobil DTE 10 Excel 32. The oil based fluid was Newtonian, and the viscosity of the mix is plotted vs the fraction of Mobil DTE 10 Excel 32 in Figure 4.6. The necessary Mobil-content to get the desired viscosity was 75%.

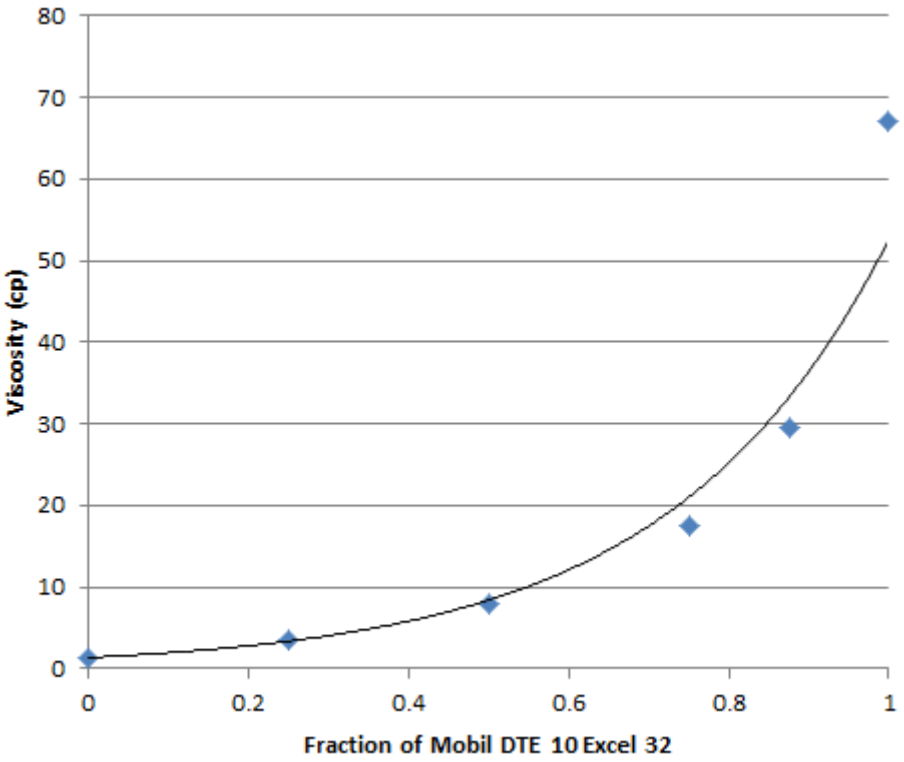

Figure 4.6: *Viscosity of the mixture of Exxsol D60 and Mobil DTE 10 Excel 32*

4.2.2 Fluids used in large scale flow loop

The experiments performed by SINTEF Petroleum in the large scale flow loop uses Laponite-fluid as the displaced fluid and CMC-fluid as the displacing fluids. Both fluids are described in section 4.2.1.

4.3 Experimental setup

This section presents the requirements and setup of the test loop. An overview of the test loop is shown and the different components are described in detail. Since both flow loops were presented during the autumn project, this section is based on the description in Giil and Johansen (2016). Some adjustments to the setup has been done based on experience from the autumn project.

4.3.1 Small scale test

A detailed schematic of the flow loop is shown in Figure 4.7.

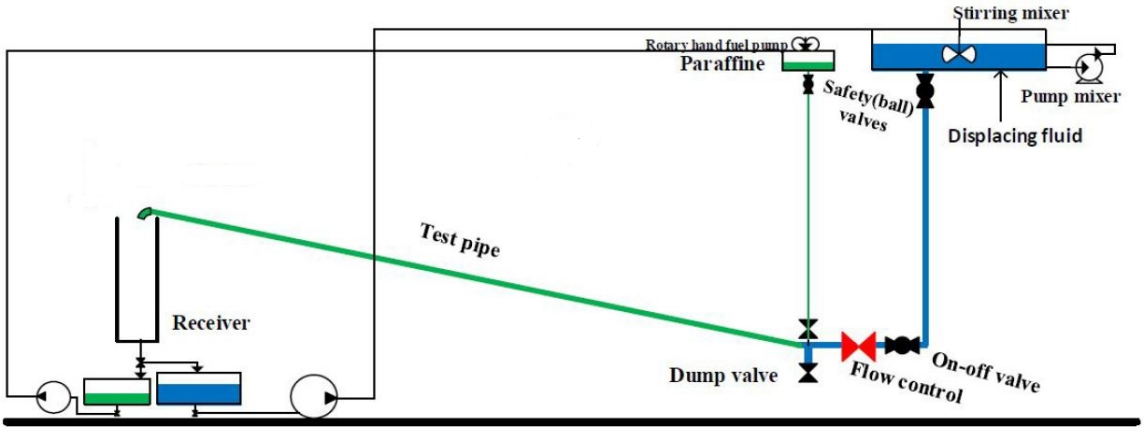

Figure 4.7: *Detailed schematic of the flowloop (Mehari, 2016).*

Flow loop design requirements

1. The entrance length should be long enough for the fluid to be stable in the inclined section of the test pipe.
2. The pressure supply must be high enough for all planned tests.
3. The flow rate must be adjustable, and repeatable between the experiments.
4. The system must be designed so that the quantities of displaced and displacing fluids can easily be measured.

Flow loop design calculations are shown in Appendix A.

Flow loop main components

Test pipe: The test pipe was a 9 m long plastic pipe with an internal diameter of 50 mm. The pipe was mounted to the wall with 13° tilt from horizontal. Entrance length was 1 m.

Measuring cylinder: At the end of the test pipe a measuring cylinder was placed to directly catch the flow from the test pipe end. The cylinder height was 1500 mm, with an internal diameter of 244 mm. This gives a capacity of 0.0468 m^3/m or a total of 0.0702 m^3. This represents 3.97 pipe volumes. If more volume was required an extra tank with a volume of 0.0471 m^3 could be coupled in series.

Separation of the displaced and displacing fluid were performed with gravity segregation in the measuring cylinder and the extra tank when oil and water based fluids were used.

Collector tanks: After gravity had separated the two fluids they were tapped over in two separate collector tanks. Here they were stored before they were pumped back to the source tanks. The capacity of these tanks were 50 l.

Source tanks: Both fluids were stored in source tanks located 7 m above the pipe inlet. This was to ensure gravity would give sufficient pressure for the system to flow. At the outlet of both source tanks on/off ball valves where fitted for the possibility to close near the source.

Water feed pipe and return hose: This pipe goes from the source tank of the displacing fluid and down to the flow loop. A larger diameter (76.2 mm) was used here to minimize the friction loss. Return to the source tank goes through a 25.4 mm hose.

Oil feed and return hose: Feed and return of the displaced fluid goes through 25.4 mm hoses.

Flow control valve: The flow rate was controlled with a gate valve. Turning of the valve regulates the flow rate.

On/off valve: The experiment was started and stopped with a on/off ball valve fitted upstream of the flow control valve. This is the main valve in the lower section controlling whether displacing fluid flow is allowed or not.

Air release valve: A small valve was fitted on the pipe, between the on/off valve and the flow control valve. This valve can be opened to remove trapped air in the pipe prior to testing. This was fitted after air bubbles were observed in the CMC- displacing Laponite-fluid tests.

Flow straightener: A flow straightener was fitted in the entrance region after the flow control valve. It has the structure somewhat similar to a honeycomb, shown in Figure 4.8. The flow straightener has two main purposes. First of all, it will contribute to creating a laminar flow regime in the test pipe. Second, we hope that it will contribute to distributing the displacing fluid to the entire cross sectional area of the pipe before displacing the displaced fluid.

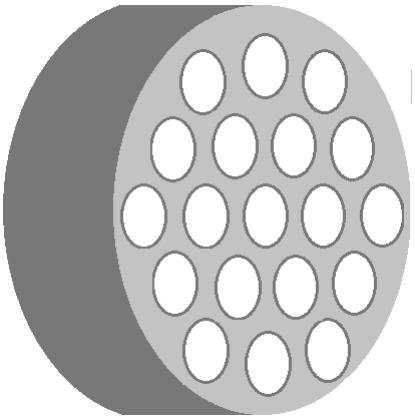

Figure 4.8: *Schematic of a flow straightener.*

Pumps: Two pumps were fitted to pump the displaced and displacing fluid from collector to source tanks after separation. A circulation pump were also fitted to the displacing fluid source tank to simplify mixing and maintain rheological properties for experiments including viscous displacing fluid.

Dump valve: A dump valve was fitted because of the need to empty the test pipe after an experiment was performed, before filling it with displacing fluid for a succeeding experiment.

4.3.2 Large scale test

The large scale flow loop is designed for displacement experiments in an annulus. A picture of the setup is shown in Figure 4.9, and a more detailed schematic is shown in Figure 4.10. The diameter of the outer pipe is 165 mm representing the open hole, with an internal pipe of 127 mm representing the casing string. The eccentricity is adjustable, giving the opportunity to simulate cementing of a casing that is not perfectly centralized. The flow loop also includes a zone where the outer pipe has a diameter of 280 mm, representing a washout. The setup can also be tilted, from horizontal and up to 30°.

The flow loop is equipped with cameras, recording video at four points along the pipe. These videos show the displacement profile at three points in the regular pipe, together with the profile in the irregular section. The displacement front is also recorded with conductivity readings at four points. Because of the difference in salinity of the displaced and displacing fluid, the front and zone where the two fluids mix can be monitored with conductivity readings. The pressure in the annulus is also measured at four points, to keep track of the pressure drop

along the pipe.

The details in the experiment will not be outlined here, but a brief introduction is the following: The displaced fluid is circulated in the loop with a low rate, and at the same time the displacing fluid is circulated at the displacing rate, which is higher, through a bypass loop. When the experiment starts the pump circulating the displaced fluid is switched of and the flow of displacing fluid is directed into the test loop immediately. Then pressure, salinity and video is recorded for a predetermined test time. After the experiment is ended the test loop is emptied and the system is flushed with hot water.

Figure 4.9: *Large scale flow loop. Small picture shows a sampling point for pressure and salinity, together with the adjusting mechanism for the eccentricity (Giil and Johansen, 2016).*

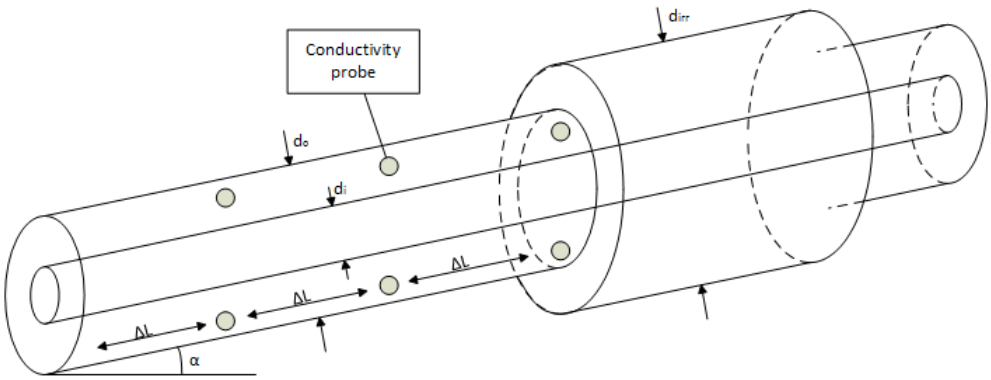

Figure 4.10: *Large scale flow loop. Values for the parameters are shown in Table 4.4.*

Table 4.4: *Values for relevant parameters in the large scale flow loop.*

Parameter	Value	Unit
ΔL	2	m
d_o	165	mm
d_i	127	mm
d_{irr}	280	mm
α	0-30	°

4.4 Test matrix for small scale flow loop

The fluid combinations for the experiments are shown in Table 4.5. Full test matrix will be performed with fluid combination *a*, as shown in Table 4.6. This is to meet the primary objective, to investigate how the surface roughness affects the displacement efficiency. To compare how rheology and fluid type affects the displacement efficiency, a secondary test matrix is developed, shown in Table 4.7. The proposed total number of experiments is then 40.

The flow rate will be varied as accurate as possible by varying the flow control valve setting, with the goal to have Reynolds numbers of 900, 600, 300 and 200.

Table 4.5: *Fluid combinations used for the small scale flow loop experiments.*

	Displacing fluid	Displaced fluid
a	CMC	Laponite
b	Laponite	Oil (17.5 cp)

Table 4.6: *Primary test matrix.*

Variable	Variations	Number of variations
Fluid comb.	a	1
Flow rate	Valve settings	4
Time (# of V_{pipe})	1.0, 1.8	2
Roughness	0/m, 6/m, 17/m	3
Number of experiments: 1×4×2×3=24		

Table 4.7: *Secondary test matrix.*

Variable	Variations	Number of variations
Fluid comb.	b	1
Flow rate	Valve settings	3
Time (# of V_{pipe})	1.3	1
Roughness	0/m, 6/m, 17/m	3
Number of experiments: 1×3×1×3=9		

4.5 Test procedures

4.5.1 Test procedure for small scale test loop

The general procedure for performing the experiments in the small scale flow loop was as follows:

1. Open the displaced fluid on/off ball valves to fill the test pipe with displaced fluid. Close when test loop is full. This is driven by gravity. At the same time make sure to release air in the system by adjusting the air release valve.
2. Adjust the flow control valve to the position for the predetermined flow rate.
3. Turn on/off ball valve for the displacing fluid to on. Start the watch simultaneously.
4. Turn off the valve when desired time of flow is reached or when desired volume in the measuring cylinder is filled.
5. Measure the volume in the collector tank, this is the total displaced volume.
6. When fluids are separated measurements of volumes of displaced and displacing fluids can be performed. If conductivity is used to determine fractions, the fluids are thoroughly mixed and sampled.
7. Drain the fluids from the measuring cylinder and into the two collector tanks.
8. Pump the fluids back to the source tanks.
9. Calculate flow rate, average velocity, Reynolds number, displacement efficiency, and find an appropriate flow model with slip velocity.

5. *Results and discussion*

This chapter presents results and discussion. Measurements performed during experiments are used in the developed model, and discussed based on simulations and expectations. Observations from the experiments are presented and discussed in comparison to measurements.

5.1 Experimental results from small scale loop

5.1.1 CMC displacing Laponite

Displacement tests were performed on slick pipe and pipe with two different roughnesses. CMC-fluid were used as displacing fluid, and Laponite-fluid were used as the displaced fluid. Their properties are described in chapter 4. The flow regime was laminar for all experiments, and the flow rate was changed between the series. Four different valve positions were used, all producing Reynolds numbers between 200 and 1000. In Table 5.1 Reynolds numbers for the experiments are presented.

The pipes in the test loop were transparent, and we were therefore able to observe the development of the displacement front, but because of the high viscosity of the displacing fluid the flow rates had to be relatively high to get the preferred Reynolds numbers. This made

Table 5.1: *Reynolds numbers for the experiments with CMC displacing Laponite.*

Series	Re_d
1	863
2	852
3	275
4	281
5	626
6	218
7	202

it difficult to observe the displacement front in real time, and interpretation had to be done on video played in slow motion. In some of the experiments it was also difficult to see a clear displacement front, as shown in Figure 5.1 which is a picture from the rough pipe (17/m) test in Series 5.

In other experiments the displacement front was clearer, as in Figure 5.2. This picture is from the slick pipe test in Series 7, and shows the development of the displacement front between the two measuring points. The displacement front was not perfectly clear, but when interpreting the video it had a shape similar to the red line presented.

In Table 5.2 the data collected from the displacement experiments with CMC displacing Laponite is presented. The total volume and time are parameters that are read directly, while two samples from each test are taken to perform conductivity measurements. The Laponite fraction is calculated based on conductivity measurements, while the volumetric efficiency, ϵ_v, and the dimensionless local velocity, v^*, are calculated based on these parameters. Figure 5.3 shows the fluid in the collector tank before it was mixed and conductivity measurements were performed.

Table 5.2: *Measured and calculated parameters for the test runs with CMC displacing Laponite.*

Series *#*	Roughness *1/m*	Test time *s*	V_{tot} *l*	Conductivity *mS/cm*	V_{lap}/V_{tot} *frac*	ϵ_v *frac*	v^* *frac*
1	0	6	15.431	4.49	0.90	0.91	0.50
	6	7.5	17.067	6.72	0.77	0.85	0.18
	17	7.5	0.016.833	6.56	0.78	0.85	0.19
2	0	11.5	27.354	10.67	0.52	0.93	0.16
	6	11	24.081	9.65	0.59	0.92	0.18
	17	12	28.897	10.76	0.52	0.97	0.30
3	0	15	16.600	6.14	0.80	0.87	0.26
	6	15	16.600	5.89	0.82	0.89	0.32
	17	15	16.132	5.54	0.84	0.88	0.34
4	0	20	21.276	9.25	0.61	0.85	0.00
	6	20	23.193	9.90	0.57	0.86	0.01
	17	25	27.822	10.08	0.56	1.01	0.55
5	0	10	18.376	7.42	0.72	0.87	0.17
	6	10	19.218	7.55	0.72	0.90	0.24
	17	10	19.545	8.51	0.66	0.84	0.02
6	0	20	19.078	7.84	0.70	0.87	0.14
	6	20	18.470	7.68	0.71	0.85	0.11
	17	20	18.704	7.62	0.71	0.87	0.16
7	0	16	14.682	3.71	0.95	0.91	0.57
	6	16	14.028	3.57	0.96	0.88	0.50
	17	16	14.028	3.66	0.96	0.87	0.48

Figure 5.1: *Picture of the displacement front at $S = 1m$ (above) and $S = 7m$ (below) from entrance for experiment Series 5, Roughness 17/m. Laponite is blue and CMC is yellow. Pictures are taken at two different times, when the displacement front passes the two points. A clear displacement front is not present.*

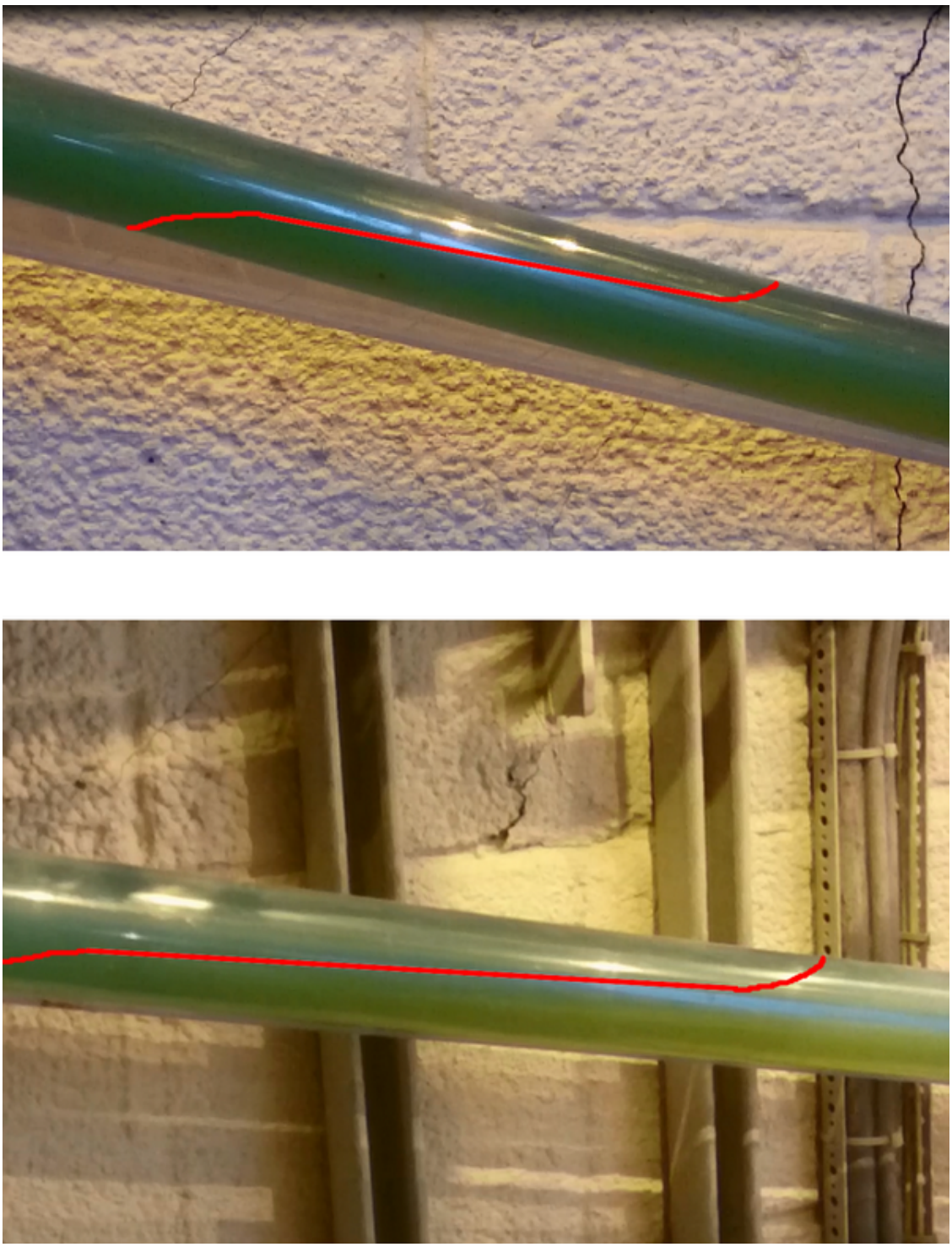

Figure 5.2: *Picture of the displacement front at $S = 1m$ (above) and $S = 7m$ (below) for experiment Series 7, Roughness 0/m. The displacement front is not perfectly clear in the picture, but its shape is highlighted in red.*

Figure 5.3: *The collector tank with the two fluids before they were thoroughly mixed and conductivity measurements were performed.*

The test time was varied as described in Table 4.6 to see how the flow volume affected the effectivity. When comparing series 1 and 2, which had the same valve setting, we can see that increasing the flow time in this case increased the volumetric efficiency. This is not the case when comparing series 3 and 4. Series 6 and 7 was also paired with the same valve setting, but the flow rate varied between the two series, so these can not be compared with flow time in mind.

Figure 5.4 shows the dimensionless local velocity for all tests plotted as a function of the pipe roughness.

Based on the recorded data it can not be concluded that the roughness in the pipes influences the displacement efficiency or the local velocity. In experiment Series 1 we experienced trouble with the flow adjusting valve. Here, the flow rate varied with 20% between the tests, and the tests can therefore not be trusted in terms of establishing a relationship between roughness and local velocity.

For experiment series 2 and 3 we see an increase in dimensionless local velocity (v^*) as the degree of roughness is increased. A weakness for Series 2 was that the test time varied with a deviation of 1% or 1s. Series 3 was perfectly conducted, but much air in huge bubbles was observed for all the tests.

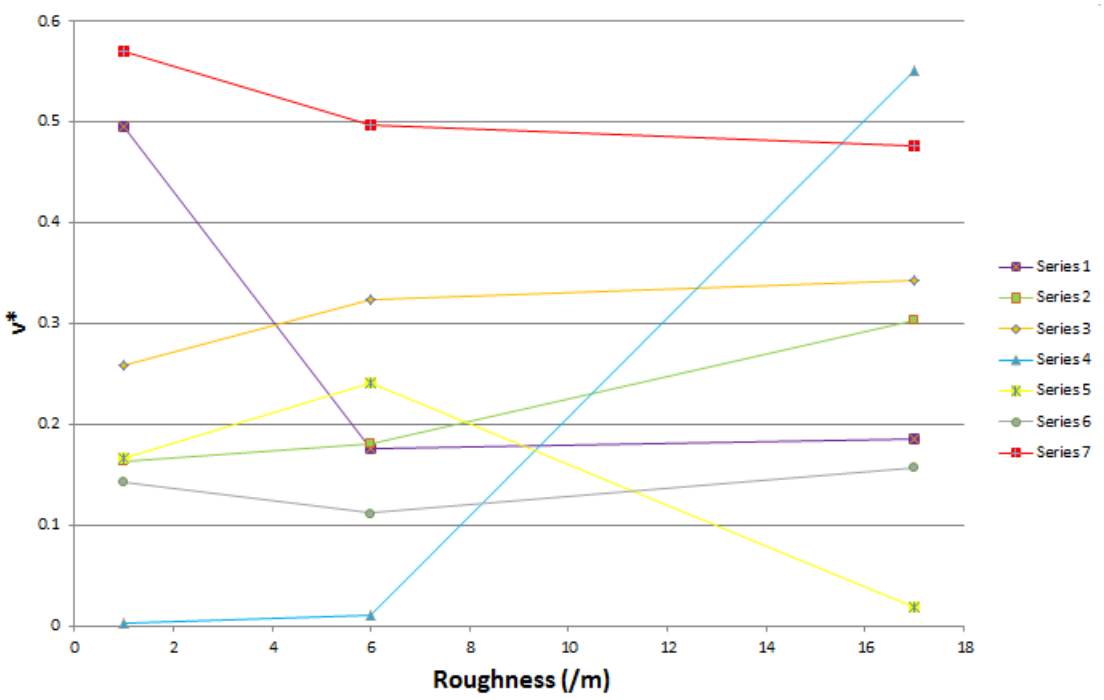

Figure 5.4: *Dimensionless velocity for experiments where CMC displaces Laponite illustrated as a function of pipe roughness.*

Series 4 shows the same trend, but these experiments could not be trusted as the Laponite-fluid fraction in the collector tank was too low to produce reliable conductivity measurements. This was because the test time was too high, $20s$ was enough to displace $1.6V_{pipe}$ and hence too much CMC-fluid entered the collector tank. This led to inconsistent efficiencies, as the rough (17/m) test which read an efficiency of 1.01. That is not possible.

In Series 5 the dimensionless local velocity is very low for the rough (17/m) test. This result is not consistent with the others, and no explanation can be given on basis of observations done while performing the experiment. Video analysis of the test run evaluated afterwords shows a lot of air bubbles present, which could affect the results.

Series 6 shows that the efficiency is equal in both the slick pipe test and the rough (17/m) test. v^* is highest in the rough (17/m) test. At both of the rough tests (6/m and 17/m) we observed a lot of huge air bubbles around the displacement front when analyzing the video. This could possibly impact the result.

For Series 7, the results show that the efficiency and v^* decreases with the roughness. The flow rate was constant within the series, but a lot of air was observed for all the tests. It is a possibility that this air is the reason why our results appear so inconsistent.

5.1.2 Laponite-fluid displacing oil

For the tests with Laponite-fluid as the displacing fluid, and the mixture of Exxsol D60 and Mobil DTE10 Excel32 as the displaced fluid, nine displacement tests were performed. This is described in Table 4.7. The tests were performed with a flow time corresponding to a flow volume in the range of $1.3V_{pipe}$. Three different valve positions were used, giving the Reynolds numbers described in Table 5.3. The flow regime was laminar, and the flow rate was changed between the series by adjusting the flow control valve.

Table 5.3: *Reynolds number for the experiments where Laponite displaces oil.*

Series	Re_d
O1	331
O2	932
O3	791

As for the CMC-fluid displacing Laponite-fluid tests, the test pipes were transparent and the observation of the displacement front could be performed by analysing slow motion video.

Before the tests with Laponite-fluid displacing oil were initiated an air release valve was installed to remove air that could have been accumulated in the space between the on/off valve and the flow control valve. By opening this valve after the pipe was filled we managed to remove about half a litre of air, and we did not observe the air bubbles described for the CMC displacing Laponite tests.

Table 5.4 gives an overview of the measured and calculated parameters of interest regarding the displacement experiments with Laponite displacing oil. Figure 5.5 shows the dimensionless local velocity for all tests plotted as a function of the pipe roughness.

Based on the recorded data it can not be concluded that the roughness in the pipes influences the displacement efficiency or the local velocity. In experiment Series O1 no problems was experienced, and the air bubbles that were observed at Series 1-7 were not present. We observed that the displacement started at the bottom of the pipe before filling the pipe completely, and this was not ideal. The results for Series O1 indicates that the displacement efficiency and the dimensionless local velocity increases with increasing roughness.

Series O2 were also performed with no problems. No air bubbles were observed, but also here the displacement tended to start at the bottom of the pipe. The results for this series indicates that the displacement efficiency and the dimensionless local velocity *decreases* with

Table 5.4: *Measured and calculated parameters for the test runs with Laponite displacing oil.*

Series *#*	Roughness *1/m*	Test time *s*	V_{tot} *l*	V_{oil} *l*	ϵ_v *frac*	v^* *frac*
O1	0	20	19.031	14.589	0.95	0.49
	6	20	18.844	14.636	0.95	0.51
	17	20	18.844	14.682	0.96	0.52
O2	0	11	19.966	14.028	0.91	0.29
	6	11	20.107	13.654	0.89	0.19
	17	11	20.481	13.420	0.88	0.12
O3	0	12	19.639	14.262	0.93	0.36
	6	12	20.247	13.560	0.88	0.16
	17	12	19.545	13.654	0.89	0.21

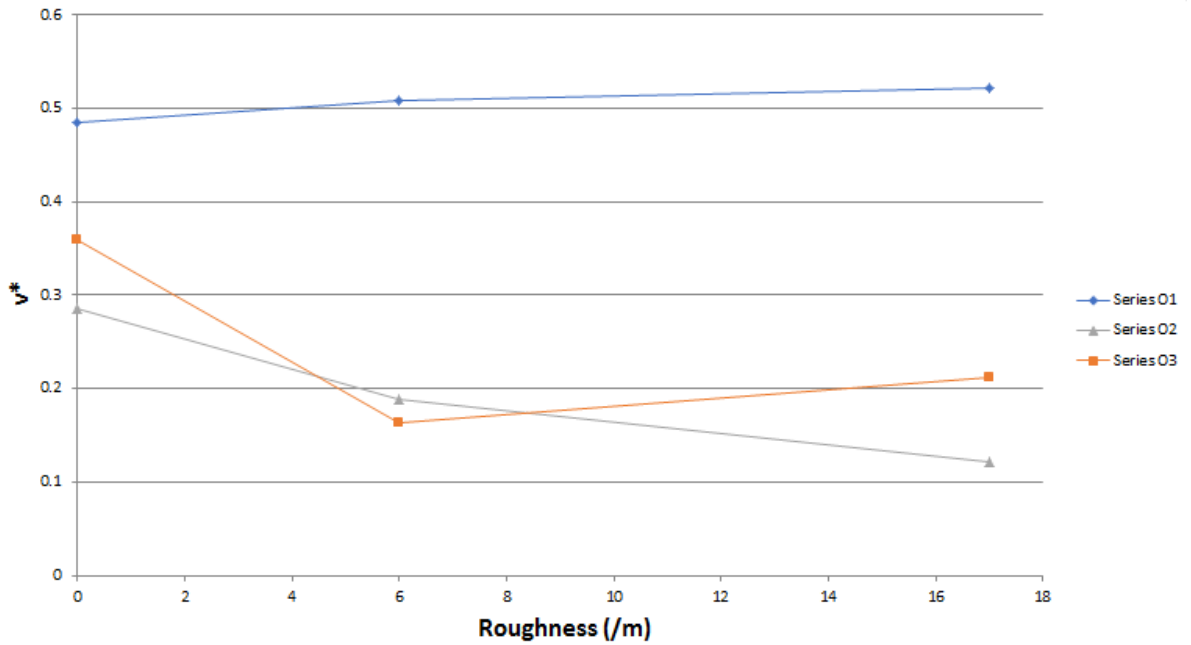

Figure 5.5: *Dimensionless velocity for experiments where Laponite displaces oil illustrated as a function of pipe roughness.*

increasing roughness.

In Series O3 the experiments were also performed with no problems. The air bubbles were not present, but the displacement started at the pipe bottom. The results for this series does not indicate either an increase or decrease in displacement efficiency and dimensionless local velocity as the roughness increases.

5.1.3 List of trouble

- **Air accumulation in valve arrangement**

  Cause of problem: Highest point in the valve arrangement was not the outlet. The low air density resulted in air migrating to the highest point.

  Effect on experiments: Wrong volume measurement and uncontrolled flow.

  Solution: Installation of an air bleed-of valve.

  Status: Solved.

- **Fluid segregation** The fluids tend to segregate in the pipe.

  1. possible cause of problem: The density difference between the displaced and displacing fluid was to high.

  Effect on experiments: The displacement front did not develop optimally.

  Solution: Do calculations to define the limit of the density difference.

  Status: Unsolved

  2. possible cause of problem: The flow control valve did open in the bottom periphery of the pipe.

  Effect on experiments: The flow at the bottom of the pipe dominated the displacement.

  Solution: Install a piece centering the flow before entering the test pipe.

  Status: Unsolved.

- **Flow rate repeatability**

  Cause of problem: The flow control valve was not accurate.

  Effect on experiments: It was not possible to repeat the exact same flow rate twice.

  Solution: Install a more accurate flow control valve, computer operated if possible.

Status: Unsolved.

- **Unable to flow displacing fluid down the feed pipe**

  Cause of problem: Air was trapped in the horizontal section of the feed pipe. The horizontal section is illustrated in Figure 5.6.

  Effect on experiments: Experiments could not be started, as it was not possible to initiate flow.

  Solution: *Temporary:* While on/off valve by the test pipe was closed, a submersible pump was used to pump displacing fluid down the feed pipe forcing the air out. *Permanent:* Use a pump for pressure supply to avoid the need of a long feed pipe.

  Status: Temporarily solved.

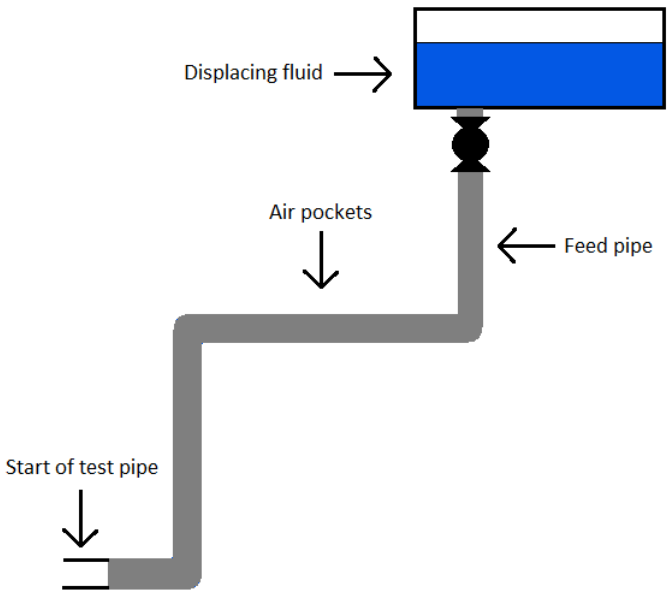

Figure 5.6: *Correct presentation of the feed pipe and the horizontal section.*

- **Fluid transfer to feed tanks**

  Cause of problem: Fluid was to viscous to be pumped up to the third floor balcony with the provided pumps. Building elevator was non-operative 90% of the time.

  Effect on experiments: A lot of time was used for carrying buckets of fluid up the stairs to the feed tanks at the third floor.

  Solution: Use a pump for pressure supply and place feed tanks at the ground floor.

  Status: Unsolved.

5.1.4 Effect of flow straightener

A flow straightener was installed after Series 4. The effect can be investigated by comparing pictures of Series 1, 2, 3, 4 with Series 5, 6, 7. The most comparative series of these is 6 & 3, and 5 & 2, as these pairs had approximately the same flow rate.

Figure 5.7 shows the difference in displacement profile for the slick pipe experiments for Series 3 and 6. Series 6 had a flow straightener installed at $0.2m$ from the inlet. Series 6 did also have a slightly lower flow rate, with $Re = 218$, compared to Series 3 which had $Re = 275$. Higher flow rate will lead to a longer displacement front, but the difference shown in Figure 5.7 is very large, and can not be explained by the flow rate difference alone.

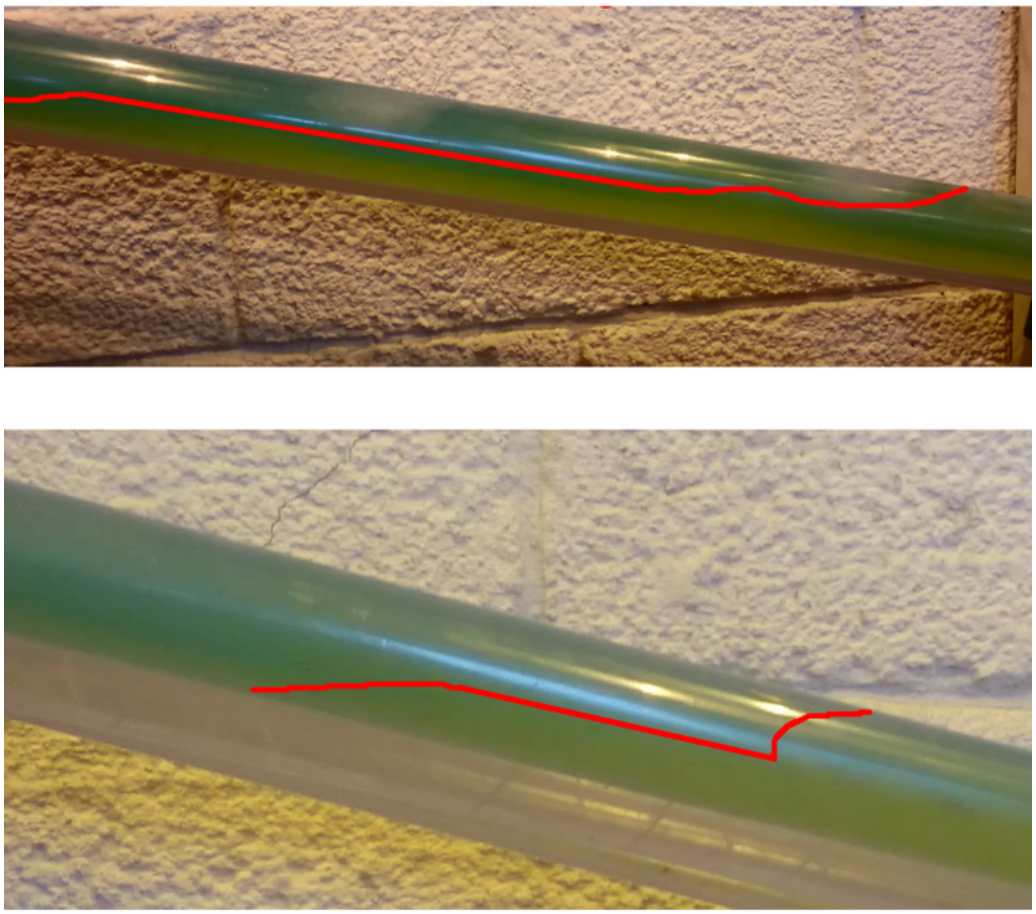

Figure 5.7: *Displacement front for slick pipe experiments in Series 3 (top) and 6 (bottom). Series 6 has a flow straightener installed at the inlet.*

For Series 2 and 5 the video quality was too poor to use for comparison between the series.

5.2 Experimental results from large scale flow loop

The large scale flow loop is built different from the small scale loop. It is an annular loop, it has an irregular section and it uses only slick pipes. This makes it inconvenient to directly compare the results with the results from the small scale loop, but since the applied fluids are the same some of the basic concepts can be interpreted with data from this experiment.

Figure 5.8 shows a plot of the time series data from conductivity probes for the concentric experiment with 10° inclination. The data was normalized between 0 and 1, where 0 indicates that only Laponite-fluid is present. 1 indicates full displacement with only CMC-fluid around the probe. Station A was placed $2m$ from the inlet, Station B at $4m$. Station C was placed at $6m$ from the inlet, right before the irregular section. Probe 5 was placed at 22.5° from the bottom, and probe 8 was placed at 22.5° from the top. This is illustrated in Figure 5.9.

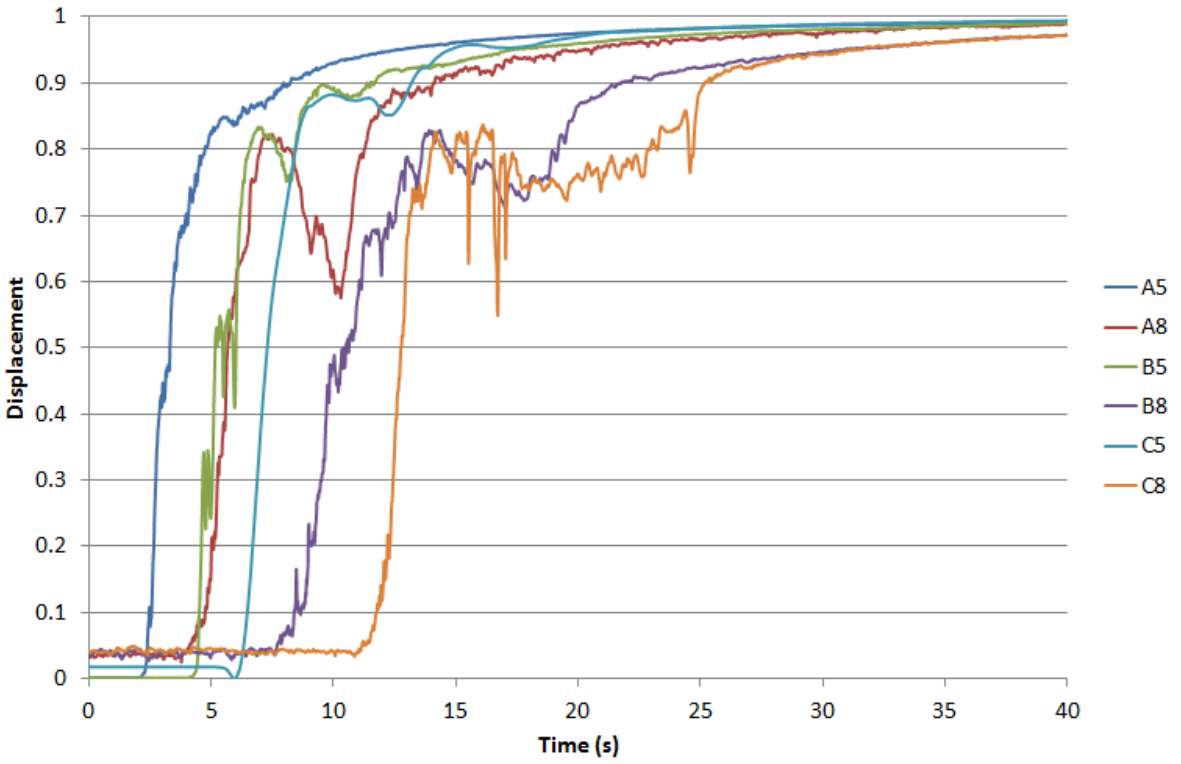

Figure 5.8: *Displacement efficiency vs time at conductivity probes placed in different positions in the large scale test loop.*

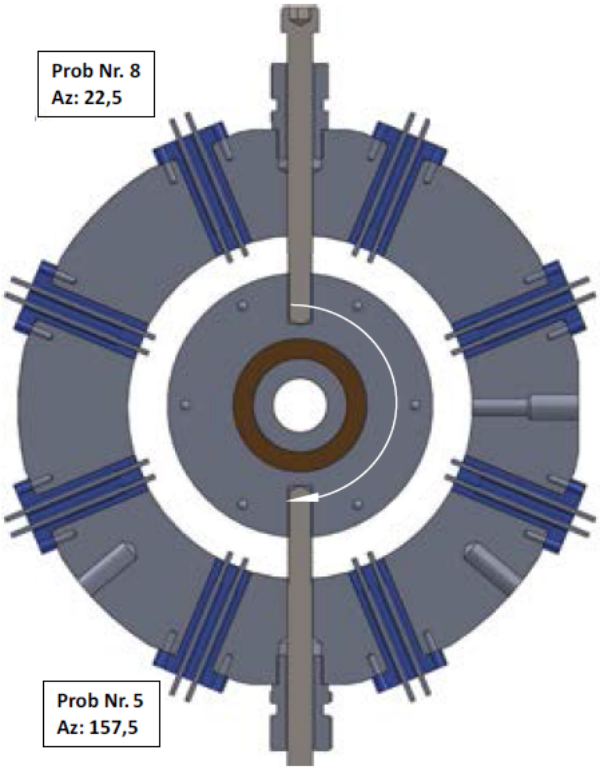

Figure 5.9: *Schematic of the probe placement. Analyzed data are from probes 8 and 5 (Ytrehus et al., 2017).*

By interpreting these data the order for breakthrough can be determined, and the time for breakthrough at the different probes can be read as shown in Table 5.5. The placement of the probes are illustrated in Figure 5.10. t_{bt} is defined as the time where the displacement at the probe is 0.1. This again could be used to calculate the velocity of the front in the different parts of the pipe as shown in Table 5.6.

Table 5.5: *Breakthrough time (t_{bt}) for the six probes.*

Probe	t_{bt} s
A5	2.54
B5	4.52
A8	4.76
C5	6.48
B8	8.40
C8	11.76

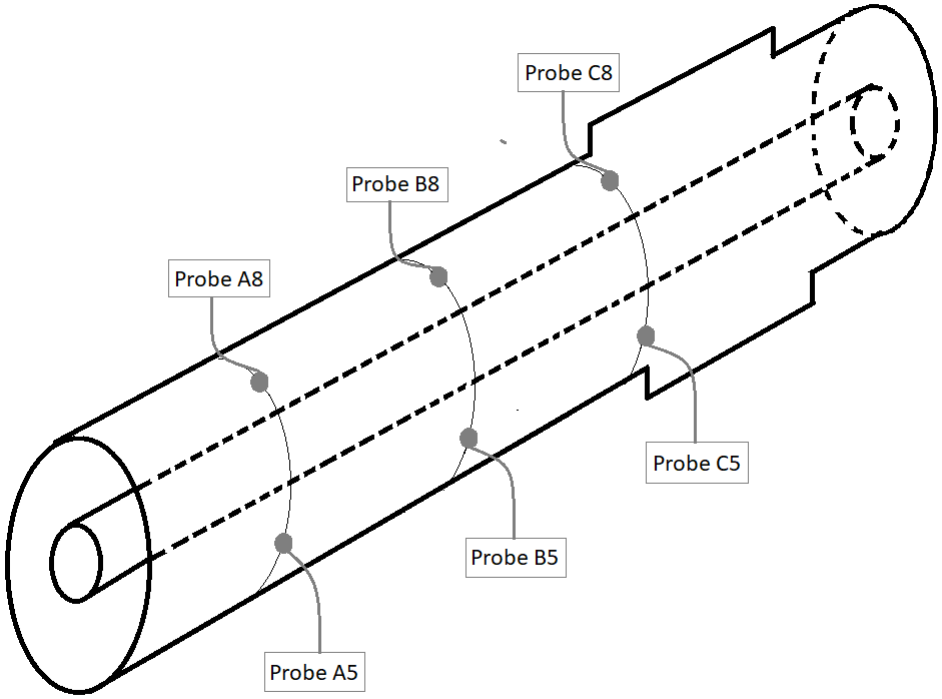

Figure 5.10: *Illustrating positioning of the different probes. Breakthrough order is A5, B5, A8, C5, B8, C8 as described in Table 5.5.*

Table 5.6: *Breakthrough times and resulting average velocities for the large scale test.*

Part	Interval	Distance *m*	Time *s*	Average velocity *m/s*
Upper	A8 to B8	2	3.64	0.549
	B8 to C8	2	3.36	0.595
	A8 to C8	**4**	**7.00**	**0.571**
Lower	A5 to B5	2	1.98	1.010
	B5 to C5	2	1.96	1.020
	A5 to C5	**4**	**3.94**	**1.015**

Conductivity measurements presented suggests that the displacing CMC-fluid displaces the bottom part of the pipe cross-section before the upper part. This observation suggests gravity segregation is present during testing.

The degree of mixing in the displacement front was also interpreted from the data in Figure 5.8, as shown in Table 5.7. Here t_{mix} is the time from the displacement is 0.1 to 0.9. t_{mix} was higher in the upper part of the pipe, but the velocity was lower here. By using the average velocity for the upper and lower parts of the pipe from Table 5.6, the length of the mixing front, l_{mix}, could be described as in Table 5.7.

Table 5.7: *Properties for the mixing displacement front of the two fluids.*

Part	Probe	t_{mix} s	l_{mix} m
Upper	A8	9.4	5.37
	B8	13.36	7.63
	C8	13.42	7.67
Lower	A5	5.4	5.48
	B5	7.02	7.13
	C5	6.72	6.82

5.3 Discussion

5.3.1 Discussion for small scale flow loop

The experiments can not be used to conclude if the roughness in the pipes influence the displacement efficiency and the dimensionless local velocity. The results show that we have test series that indicates both a positive and negative correlation, or no correlation at all. In the experiments with CMC-fluid displacing Laponite-fluid, air bubbles were observed in the flow and identified as a possible problem. By modifying the flow loop, installing an air bleed-off valve, these air bubbles were avoided. The following experiments with Laponite-fluid displacing oil were run without air-bubbles present in the flow. Still, without the presence of air-bubbles, the experimental results were inconsistent, like previously experienced.

There are several possibilities why the results appeared so inconsistent. First, the density difference between the CMC- and Laponite-fluid were not optimal, and calculations in chapter 3 indicates that gravity segregation could dominate the flow. Calculations supports this also for the experiments with Laponite-fluid and oil. Although the gravitational force acting on the system affects the flow, it is important to investigate other explanations to the significant segregation observed during testing.

Another reason for this segregated fluid behaviour can be the construction of the flow loop, specially the flow control valve. This is a gate valve, and for the flow rates used for these experiments, only a small part of the valve has been opened. Because this valve opens from the bottom, the flow into the displacable volume might have been dominated by a flow on the bottom for a longer entrance length than initially expected. As shown in Appendix A, the demanded entrance length is longer than the actual entrance length, and the construction of the gate valve that was installed in the flow loop will probably increase this even more.

Since the flow was obviously dominated by gravity and/or entrance effects the modeled displacement profile did not describe the situation. Comparing it to the experiments performed in the autumn project (Giil and Johansen, 2016) the model in the Master thesis describes the situation better, but still not perfect.

5.3.2 Discussion for large scale flow loop

By analyzing the data in Table 5.5 it can be observed that the flow velocity was higher in the bottom than in the top. Table 5.6 shows the travel times between the stations (A, B, C) for the upper (8) and lower (5) probes, together with the average velocities between the stations. As we see the average velocity in the upper part of the pipe is 44% lower than in the lower part of the pipe.

By comparing this to the analysis for the small scale flow loop we can see that the segregation effect in the large scale flow loop was much smaller than for the small scale flow loop. Based on the entrance design of the large scale flow loop, we assume that the segregation appearing in this test loop is caused by gravity (Ytrehus et al., 2017). It is logical that the gravitational impact is lower for an annular flow, as the fluid will experience more shear forces because of the inner pipe also acting as a boundary, but it can not be concluded if this is the only difference between the two flow loops, or if entrance effects in the small scale flow loop also is of significance.

As described in Table 5.7, there was a small difference in the length of the mixing front between the upper and lower part of the pipe. For Station A, the mixing front was 2% shorter in the upper part of the pipe, whereas for Stations B and C the front was 7% and 12% longer in the upper part. This difference is small, and the data provided is not enough to conclude if a trend is present and what causes these deviations. For the development in the axial direction it is different, and the mixing front is much shorter at Station A than at Station B, whereas it appeared more or less constant between B and C. This observation may indicate that at Station A the flow was under impact of entrance effects.

6. *Self assessment*

This chapter contains quality evaluations of both the theoretical model and the experimental setup. These evaluations are based on results and observations obtained while working with the project. Based on these evaluations, considerations for further work and improvements are presented concerning both the theoretical and practical aspects.

Quality of theoretical model and simulations

The basis for simulations and visualizations of experimental results is the model development in chapter 3. This chapter also covers simplifications and assumptions for the model. When simulating, these assumptions makes sense, and the results look promising. In terms of simulating a real cement operation, the model has several shortcomings. This is the fact that the model simulate flow in a pipe only, and it does not take gravitational forces on the displacement process into account. However, the physics and principle of displacement is independent of being annular or simple pipe geometry, and thus the simplification from annular to pipe geometry will not lead to any error. The gravitational forces on the other hand did dominate the flow, so this is associated with a non-negligible error.

The model is based on single fluid flow, meaning that the rheological properties of the displaced fluid is not taken into account. This is a shortcoming that may lead to less accurate results. However, the displacing fluid will dominate if it is more viscous than the displaced fluid, and thus this is a negligible error.

Quality of experiments

The experimental setup is a pre-existing setup. Alterations have been done, such as changing test pipe dimensions. It is not meant to simulate a real well, and therefore it has some

major simplifications regarding size, material, regular pipe flow and fluids used. These simplifications are used mainly because of economy and available space. Regular pipe flow is used because it is easier to observe the displacement front, and the results can in principle be transferred to apply for annular flow. Except for these simplifications, there are also some sources of error associated with the setup.

- Having a fully developed velocity profile is an assumption for comparing the theoretical model to the experimental results. Calculations performed in Appendix A indicated that this could be a problem, and analysis of video of the experiments supports this. The flow did not seem to be fully developed, and a main problem seem to be the entrance effects.
- Gravity segregation seems to be the major problem. Calculations indicates that the applied gravity differences will lead to segregation, and results from small scale and large scale flow loop supports this.
- The gate valve that acts as the flow control valve opens from the bottom resulting in a flow that is concentrated at the bottom of the pipe.

Improvements and consideration for further work

1. Model and fluid properties

Based on test observations and results, we believe that gravitational forces acts and impacts the system. This directly violates the associated model assumption mentioned in chapter 3. For further work, changes to the model might be necessary and other assumptions has to be considered.

Before using the model developed in this thesis to estimate slip velocity, the impact of gravitational force has to be eliminated. A possible method could be to use two water based fluids with the same density, but different viscosity. Having salt added to one of the fluids, conductivity measurements can be used to determine the volume fraction of the two fluids in the collector tank. Two water based fluids with the same density is preferred over one oil based and one water based fluid with the same density, as the latter would probably lead to separation problems in the collector tank, which in turn would lead to inaccurate volume measurements. Laponite is in this case a good viscosifier, as the density is 1000 kg/m^3.

Adding salt to one of the fluids would increase the density slightly, but this increase is probably negligible, as small amounts of salt is needed to increase the conductivity drastically. It is also recommended to add different colors to the two fluids, so that the displacement front can easily be observed visually and the impact of roughness can be interpreted from video.

Another possible method to avoid gravitational segregation is to run a single fluid experiment, where a tracer is added to the fluid at the inlet. The tracer particles travel length can then be observed on video to describe the velocity profile, and interpret the impact of roughness.

With the primary objective to determine how pipe roughness influences the flow it is recommended to focus on this first, and investigate the influence of different rheologies and fluid combinations as a secondary objective.

2. Experimental setup

The results of the experiment do not match the theory and expectations. Both results and observations during testing indicates that weaknesses are present in the pre-existing flow loop. In this section two different flow loop designs will be proposed. The first proposal suggest using a pump to drive the displacement process of two water based fluids with equal density. The other proposal suggests using a single-fluid approach, where a tracer is added to the fluid and monitored as it flows through the pipe.

1. proposal: Two-fluid approach with pumps This proposal suggests using a pump to drive the displacement process. Important elements of the flow loop is described below and illustrated in Figure 6.1.

- **Pump:** It is recommended to install a pump that can be used to drive the displacing fluid. This will ensure stable pressure supply and simpler operation. Using a pump to drive the displacement process will in addition to the benefits mentioned above, lead to a simplified fluid handling process, allowing the tanks containing fluids to be placed on the main floor.

- **Flow control valve:** A flow control valve should be positioned as illustrated in Figure 6.1 and Figure 6.2. This will enable flow rate adjustments.

- **Centered flow piece:** After the flow control valve, a pipe section with a smaller radius is fitted. This section is illustrated in Figure 6.2. The purpose of this section is to make sure the flow is centered when entering the test pipe section, reducing undesirable entrance effects.

- **On/off valve:** The on/off valve needs to go from closed to fully opened immediately, and have minimum restriction compared to the pipe radius where it is fitted. For the velocity profile to develop undisturbed it is also important to have the same diameter on both sides of the on/off valve. To increase repeatability an electronic valve can be installed, where opening and closing is managed by a computer. Opening at a command, and closing after a predetermined flow time. The preferred placement of this valve is in the centered section as shown in Figure 6.2.

- **Flow meter:** To increase the accuracy of the rate measurements it is recommended to install a flow meter.

- **Air bleed-of valves:** Air bleed-off valves is proposed placed along the test pipe as illustrated in Figure 6.1. The purpose of these valves is to reduce the amount of trapped air in the test loop prior to testing.

- **Roughness:** The roughness in the test pipes needs to be discussed more, to better understand if more variation is needed to recognize if the local velocity changes. Deeper grooves or other structures needs to be discussed.

- **Conductivity meter:** A conductivity meter is necessary to calculate fluid fractions. SINTEF has one, but it is more practical if NTNU acquires a separate one for this project.

- **Cameras:** To see how the displacement front develops throughout the test pipe two or more cameras needs to be installed. Three cameras, and a setup with a computer to control the cameras is recommended.

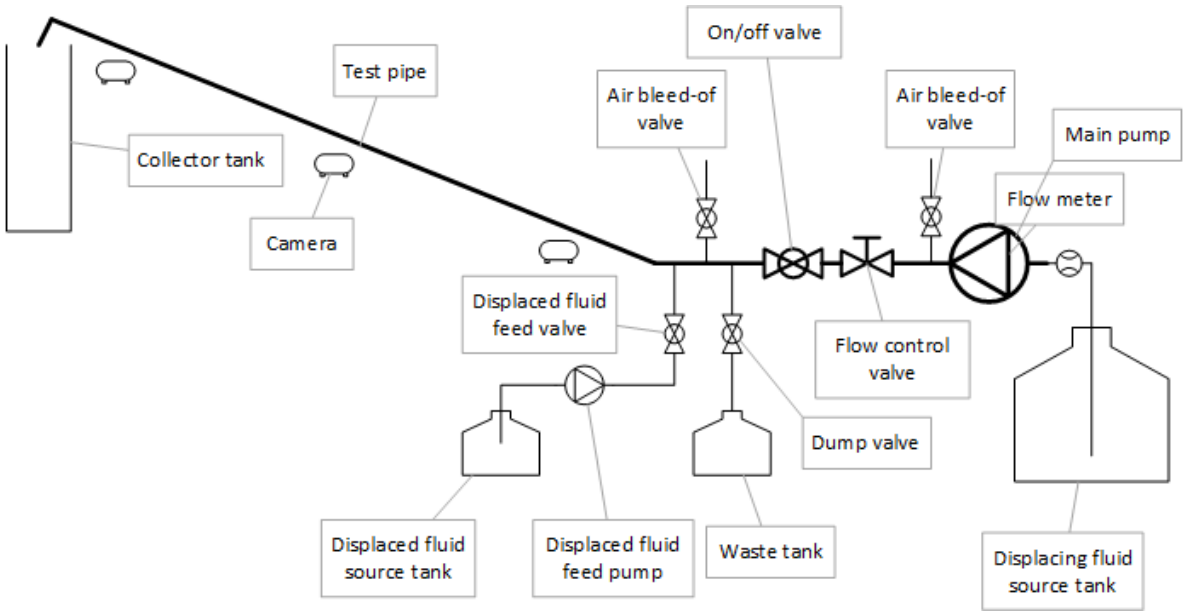

Figure 6.1: *Proposal 1 for a better flow loop design. Note that all fluid handling and operation can be done at the main floor.*

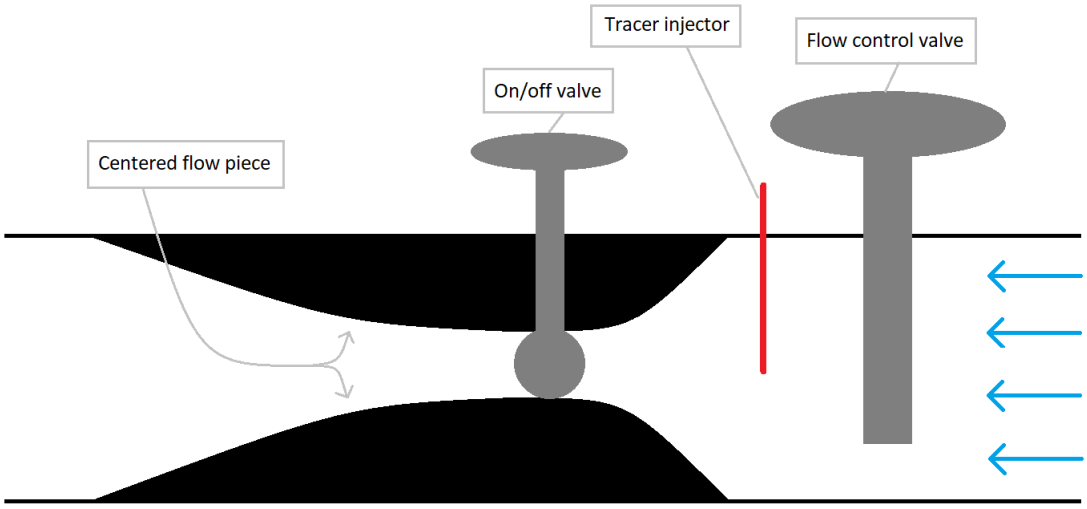

Figure 6.2: *Detailed schematic of the inflow design for proposal 1 and 2. Tracer injector (red) is relevant only for proposal 2.*

2. proposal: Single-fluid approach The scope of this thesis has been to observe if the velocity at the pipe wall is influenced by pipe roughness, and to determine if the no-slip theory is applicable at all time. To do experiments with displacement flow is not necessary to investigate this, even though the most important application in the oil industry is the displacement flow when performing cementing operations. Below is a proposal for a setup using a single

fluid with a tracer, together with high speed cameras for analysis.

- **Pressure supply:** For this setup the pressure supply is a pump. A pump is suitable as it simplifies fluid handling, gives a stable pressure supply and simplifies operation and fluid handling.
- **Tracer:** A tracer is continuously added to the fluid at the inlet to give points that are possible to track visually throughout the pipe. Polystyrene is a suitable tracer material.
- **High speed cameras:** Two or more high speed cameras are necessary to see how the fluid front develops throughout the pipe. Three cameras, and a setup with a computer to control the cameras is recommended.
- **Visual analysis software:** A computer with software suitable for visual tracer analysis is necessary to monitor how the velocity profile of the flow develops. Methods using particle image velocimetry or particle tracking velocimetry are suitable for this.

A sketch of the inflow design for the single-fluid setup is shown in Figure 6.3. A sketch of the methodology for analysis of the velocity profile is also shown. Here the computer software follows the specific particles at the straight line chosen at time $t1$ and highlights them with a drawn line on the image of the flow at time $t2$. A detailed schematic of the inflow design is shown in Figure 6.2, and it is the same valve arrangement as used in proposal 1.

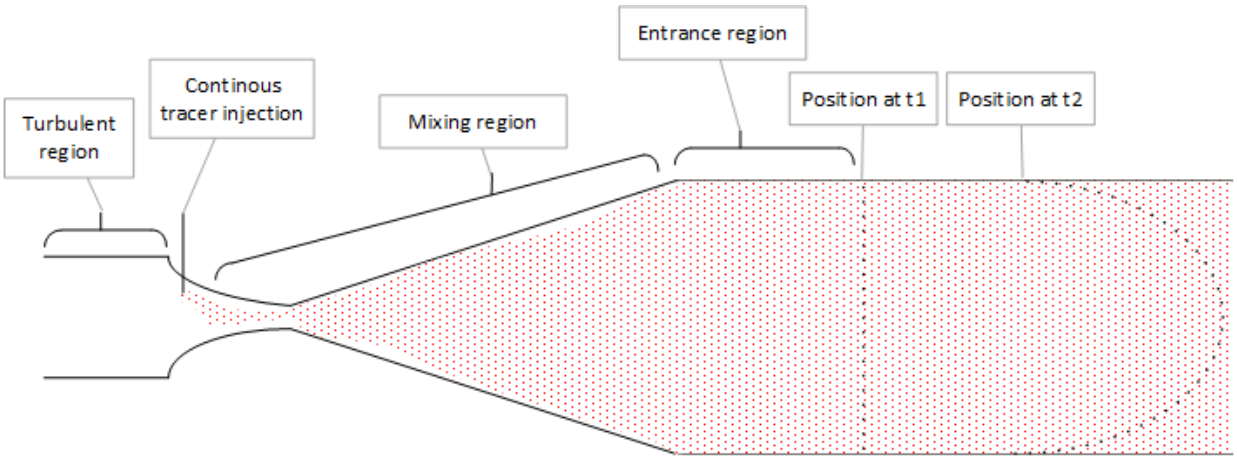

Figure 6.3: *Simplified setup for the inflow design in proposal 2, with single-fluid and tracer. Tracer particles of interest shown with a dotted line at two different times $t1$ and $t2$. Detailed schematic of the inflow design is shown in Figure 6.2.*

7. *Conclusion*

Conclusions below are based on knowledge gathered from the theoretical study, simulations and experiments.

1. A higher local velocity will lead to a flatter velocity profile resulting in a better volumetric efficiency. Thus, a higher local velocity would be preferable in terms of achieving better fluid displacement.

2. Fluid rheology impacts the displacement. Thus, the fluids should be constructed in such a way that the rheological properties give a displacement efficiency as good as possible to prevent a poor cement job.

3. Gravity segregated fluid displacement should not occur during cementing of a horizontal well section.

4. The effect of roughness could not be investigated in current experiments due to shortcomings present in the test setup leading to segregated flow.

5. Inconsistent results and observable weaknesses has lead to the conclusion that the flow loop has to be redesigned. Two different designs are presented in chapter 6.

Nomenclature

Acronyms

API	American Petroleum Institute
IPT	Department of Petroleum Engineering and Applied Geophysics
NTNU	Norwegian University of Science and Technology
PTS	Petroleumsteknisk senter
SPE	Society of Petroleum Engineers

Symbols

A	Area
d	Pipe diameter
d_d	Droplet diameter
d_i	Diameter of inner pipe in large scale flow loop
d_{irr}	Diameter of irregular section in large scale flow loop
d_o	Diameter of outer pipe in large scale flow loop
f_d	Darcy friction factor
F_g	Gravitational force
F_τ	Viscous (shear) force

g	Acceleration of gravity
K	Consistency factor
L	Pipe length
ΔL	Distance between conductivity probes in large scale flow loop
l_d	Droplet falling distance
l_{mix}	Length of mixing front
m	Mass
n	Flow index
P	Pressure
Δp	Pressure drop
q	Flow rate
R	Pipe radius
r	Radial position
r_0	Plug flow radius
r_d	Droplet radius
Re	Reynolds number
R^2	Coefficient of determination
s	Distance from pipe inlet
S_f	Displacement front position
S_t	Displacement tail position
t	Time
t_{bt}	Breakthrough time
t_{mix}	Time mixing front uses to pass probe

T	Temperature
v	Velocity
v_0	Plug flow velocity
v_d	Droplet falling velocity
v_{local}	Slip velocity (velocity of tail)
v_{max}	Maximum velocity (velocity of front)
$\bar{v}$	Average velocity
v_δ	Flow velocity at the edge of the viscous sublayer
v^*	Dimensionless local velocity
v_*	Friction velocity
V_o	Oil volume
V_t	Total volume
V_w	Water volume
$w\%$	Weight-percent
y	Distance from pipe wall

Greek letters

α	Angle from vertical
γ	Shear rate
$\delta_{sublayer}$	Thickness of viscous sublayer
ϵ	Displacement efficiency
ϵ_a	Areal displacement efficiency
ϵ_v	Volumetric displacement efficiency

μ	Viscosity
μ_{pl}	Plastic viscosity
ν	Kinematic viscosity
ρ	Density
τ	Shear stress
τ_0	Yield stress
τ_w	Wall shear stress

Bibliography

Alba, K., S. M. Taghavi, and I. A. Frigaard (2012). Miscible density-stable displacement flows in inclined tube. *Physics of Fluids 24*(12).

API RP 13B-1 (2003). *Recommended Practice for Field Testing Water-based Drilling Fluids* (Third ed.). Washington, DC.: API.

Batista, T., A.-M. Chiorcea-Paquim, A. M. O. Brett, C. C. Schmitt, and M. G. Neumann (2011). Laponite rd/polystyrenesulfonate nanocomposites obtained by photopolymerization. *Applied Clay Science 53*(1), 27–32.

Bayville Chemical Supply Company Inc. (2014). Laponite RD powder. `https://www.bayvillechemical.net/production-chemicals/laponite-rd-powder` (accessed 30 November 2016).

Bourgoyne Jr., A. T., K. K. Millheim, M. E. Chenevert, and F. S. Young Jr. (1986). *Applied Drilling Engineering*. SPE Textbook Series, Volume 2. Richardson, TX: Society of Petroleum Engineers.

Braghini, A., M. F. Naccache, M. I. Fonseca, C. R. de Miranda, A. L. Martin, and P. E. Aranha (2010). Effect of rheology on flow displacement during cementing process in oil wells. 13th Brazilian Congress of Thermal Sciences and Engineering, Uberlândia, MG, Brazil, 05-10 December.

Bu, Y., Z. Li, C. Wan, and H. A. Li (2016). Determination of optimal density difference for improving cement displacement efficiency in deviated wells. *Journal of Natural Gas Science and Engineering* **31**, 119–128. `http://dx.doi.org/10.1016/j.jngse.2016.03.008`.

Cengel, Y. A. and J. M. Cimbala (2006). *Fluid Mechanics - Fundamentals and Applications* (Second ed.). New York City, NY: McGraw-Hill.

Corino, E. R. and R. S. Brodkey (1969). A visual investigation of the wall region in turbulent flow. *J. Fluid Mech. 37*(1), 1–30.

DrillWell (2016). Well solutions for improved recovery. http://www.drillwell.no/research-/program-3, (accessed 18 May 2017).

Fann Instrument Company (2016). *Model 35 Viscometer - Instruction Manual*. Houston, TX.

Giil, G. L. and E. Johansen (2016). *Cement displacement efficiency in rough pipes*. Project thesis, Norwegian University of Science and Technology, Trondheim.

Glover, P. W. J. (2000). *Petrophysics - Msc Course Notes*. Aberdeen: University of Aberdeen, Department of Geology and Petroleum Geology.

Hawker, D. (2001). *Drilling Fluid Hydraulics Manual*. Calgary, Alberta: Datalog Technology.

Hemphill, T. (1993). Yield-power law model more accurately predicts mud rheology. *Oil and Gas Journal 91*(34).

Lam, C. and S. A. Jefferis (2014). Interpretation of viscometer test results for polymer support fluids. Presented at Geo-Shanghai 2014, Shanghai, 26-28 May. dx.doi.org/10.1061/9780784413449.043.

Laponite RD, Technical Data Sheet (2013). byk-chemie gmbh: Wesel, byk additives & instruments. http://www.byk.com/en/additives/additives-by-name/laponite-rd.php, (accessed 20 March 2017).

Leinebø, R. (1971). *Precision of salinity determinations by Mohrs method and by conductivity measurements*, Volume 27 of *Report (Universitetet i Bergen. Geofysisk institutt. Avd. A. : trykt utg.)*. Bergen: University of Bergen.

Lund, B. (2016). P3.5 Drillwell - Recipe for mixing fluids. Internal Memo, Sintef Petroleum AS, Trondheim.

Madlener, K., B. Frey, and H. K. Ciezki (2007). Generalized reynolds number for non-newtonian fluids. Presented at the 2nd European Conference for Aerospace Sciences, Brussels, 1-6 July. http://dx.doi.org/10.1051/eucass/200901237.

Mehari, M. R. (2016). *Cement Displacement Efficiency in Smooth and Rough Pipes*. Master thesis, Norwegian University of Science and Technology, Trondheim.

Olowolagba, K. O. and K. B. Yerubandi (2011). Improved spacer rheology model for cement operations. Presented at the SPE Production and Operations Symposium, Oklahoma City, Oklahoma, 27-29 March. SPE-140805-MS. http://dx.doi.org/10.2118/140805-MS.

Perotti, G. F., H. S. Barud, Y. Messaddeq, S. J. L. Ribeiro, and V. R. L. Constantino (2011). Bacterial cellulose–laponite clay nanocomposites. *Polymer* **52**(1), 157–163. http://dx.doi.org/10.1016/j.polymer.2010.10.062.

Shahriar, A. (2011). *Investigation on Rheology of Oil Well Cement Slurries*. Phd thesis, University of Western Ontario, London, Ontario.

Syvum Technolgies Inc. (1999). Problem solutions in transport phenomena: Fluid mechanics problems. http://www.syvum.com/cgi/online/serve.cgi/eng/fluid, (accessed 17 November 2016).

Werner, B., B. Lund, B. R. Kosberg, E. Johansen, G. L. Giil, and J. D. Ytrehus (2017). Effect of preconditioning and ageing on rheological properties of model-drilling fluids. *Annual Transactions Of The Nordic Rheology Society 25*, 5.

Ytrehus, J. D., B. Lund, A. Taghipour, S. Divyankar, and A. Saasen (2017). Experimental investigation of wellbore fluid displacement in concentric and eccentric annulus. International Conference on Ocean, Offshore and Arctic Engineering, Trondheim, 25-30 June.

Appendices

Here is a short overview over the contents in the appendices.

Appendix A - *Flow loop design requirements*

Here is design requirements for the flow loop presented. This includes calculations to determine if the gravity will be sufficient for pressure supply, calculations of how long the entrance region will be, and a description of how the roughness in the pipe is made together with argumentation for its impact on the velocity profile. Parts of this appendix are inspired by Giil and Johansen (2016).

Appendix B - *Reynolds Number for non-Newtonian fluids*

This appendix presents the work of Madlener et al. (2007) who shows how the Reynolds number can be calculated for non-Newtonian fluids, and was also presented in Giil and Johansen (2016). Equations are presented to calculate the pressure drop for the test pipe.

Appendix C - *Determination of rheological constants for non-Newtonian fluids*

Here the method presented by Hemphill (1993) to determine the rheological constants for non-Newtonian fluids is shown.

Appendix D - *Risk assessment*

This appendix includes the risk assessment performed before the laboratory work was initiated. The risk assesment was performed in Risk Manager in cooperation with professor Pål Skalle.

Appendix E - *Simulation tables*

In this appendix values and data used to produce some of the plots in section 3.5 are shown.

Appenix F - *Procedure for Rheology measurements with Fann viscometer*

Here is a presentation of the general procedure for Rheology measurements with Fann 35 rotational viscometer. This was also presented in Giil and Johansen (2016).

A. *Flow loop design requierements*

A.1 Pressure supply

The flow loop should be design so that the pressure supply is satisfactory for all planned activities.

1. Hydrostatic pressure from feed tank to flow loop is the driving force.
2. All planned tests will be performed under laminar flow conditions. Turbulent flow may be a future demand, so a Reynolds number of 4000 is the criteria.
3. Friction in the large diameter feed pipe is assumed neglible.

The most viscous fluid that is planned to be used as displacing fluid is the CMC-fluid. Using Fann-measurements shown in Table 2.1, and interpreting it to describe a Power-law fluid the flow rate necessary to obtain the specific Reynolds number can be calculated with Equation B.2. The corresponding frictional pressure drop, Δp_f, in the test pipe is found by using Equation B.6. Using the Bernoulli equation (Cengel and Cimbala, 2006) to perform an energy balance we can see if the hydrostatic pressure supply is great enough to be the only driving force. This criteria is shown in Equation A.1, and in Table A.1 we can see that the criteria is fullfilled.

$$\rho g h > \frac{1}{2}\rho v^2 + \Delta p_f \tag{A.1}$$

Table A.1: *Values for the different parts of the Bernoulli equation.*

Left side	Right side
$\rho gh = 75\,537\ Pa$	$\frac{1}{2}\rho v^2 = 9\,981\ Pa$ $\Delta p_f = 32\,652\ Pa$
Sum = 75 537	Sum = 42 653

A.2 Entrance length

The flow loop should be designed with an entrance length long enough for the fluid to be stable in the inclined section of the test pipe. For laminar flow the entrance length is shown in Equation A.2 (Cengel and Cimbala (2006)).

$$L_{h.lam.} = 0.05 Re_d D \tag{A.2}$$

For the highest laminar Reynolds number, $Re_d = 2300$, the resulting entrance length is

$$L_{h.lam.} = 0.05 \times 2300 \times 0.05 = 5.75\ m.$$

The actual entrance length is less than this, $L_{entr} = 1.5\ m$. In Figure 4.7 this is the distance from the $Flow\ control\ valve$ to the start of the inclined pipe section. This means that the velocity profile may not be fully developed before the front enters the inclined section, and this is a weakness of the system.

For turbulent flow the entrance length is shown in Equation A.3 (Cengel and Cimbala (2006)).

$$L_{h.turb.} = 1.359 Re_d^{1/4} D \tag{A.3}$$

For $Re_d = 4000$, which is the flow loop design criteria, the resulting entrance length is

$$L_{h.turb.} = 1.359 \times 4000^{1/4} \times 0.05 = 0.54 m.$$

The actual entrance length is higher than the demand for a turbulent flow regime, and thus the velocity profile can be expected to be fully developed before the front enters the incline section.

A.3 Roughness

As stated in chapter 2, the criteria for breaking the viscous sublayer with the presence of a local turbulence is given by a roughness height comparable to the viscous sublayer thickness. The rule of thumb is that the viscous sublayer thickness, y, is less than 1% of the pipe diameter (Cengel and Cimbala (2006)), here corresponding to:

$$y = 0.01 \times D = 0.01 \times 50\ mm = 0.5\ mm.$$

The roughness in the test pipe is made as an indentation groove (not protruding). The groove has a spiral shape, with a spiral tightness of 5 and 20 rounds per axial meter for the two different roughness degrees. The depth of the roughness is 1 mm. This is 2% of the diameter, which is comparable to the 1% criteria stated above. The experimental work is aiming to prove a relationship between the spiral tightness and the slip velocity, v_{local}. Figure A.1 shows a pipe section with the spiral roughness pattern.

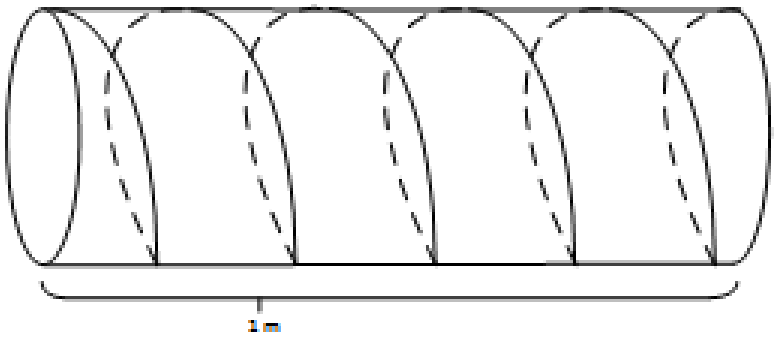

Figure A.1: *Pipe section of 1 m of a pipe with a roughness tighthness of 5/m.*

B. *Reynolds Number for non-Newtonian fluids*

Madlener et al. (2007) shows how the Reynolds number can be calculated for Herschel-Bulkley (Equation B.1), Power-law (Equation B.2), Bingham (Equation B.3) and Newtonian (Equation B.4) fluids. The formulas are given below:

$$Re_{HB} = \frac{\rho \bar{v}^{2-n} D^n}{(\tau_0/8)(D/\bar{v})^n + K[(3m+1)/(4m)]^n 8^{n-1}} \tag{B.1}$$

$$m = \frac{nK(8\bar{v}/D)^n}{\tau_0 + K(8\bar{v}/D)^n}$$

$$Re_{PL} = \frac{\rho \bar{v}^{2-n} D^n}{K[(3m+1)/(4m)]^n 8^{n-1}} \tag{B.2}$$

$$m = n$$

$$Re_B = \frac{\rho \bar{v} D}{(\tau_0/8)(D/\bar{v}) + \mu_{pl}(3m+1)/(4m)} \tag{B.3}$$

$$m = \frac{\mu_{pl}(8\bar{v}/D)}{\tau_0 + \mu_{pl}(8\bar{v}/D)}$$

$$Re_N = \frac{\rho \bar{v} D}{\mu_{pl}} \tag{B.4}$$

$$m = 1$$

These formulas are used for calculating the Darcy friction factor (f_d) and the pressure loss per pipe length ($\Delta p/L$), which is used to calculate the velocity of the fluid ($v(r)$) in Equation 2.8, 2.12, 2.13 and 2.16. The equations for f_d and $\Delta p/L$ is shown in Equation B.5 and B.6.

$$f_d = \frac{Re}{64} \tag{B.5}$$

$$\frac{\Delta p}{L} = f_d \frac{\rho \bar{v}^2}{2D} \tag{B.6}$$

C. *Determination of rheological constants for non-Newtonian fluids*

A well known procedure to interpret the Fann 35 Viscometer readings to describe the Herschel-Bulkley parameters of a fluid is to use the 3RPM viscometer reading to describe the yield point (τ_0). K and n are then found by linear interpretation of a log-log plot of $\tau - \tau_0$ vs shear rate (γ).

In Hemphill (1993) a more accurate method is proposed, which uses three partial derivatives that minimize the error of prediction, shown in Equation C.1 to C.3.

$$\frac{\delta \Sigma [\tau_i - (\tau_0 + K\gamma_i^n)]^2}{\delta K} = 0 \tag{C.1}$$

$$\frac{\delta \Sigma [\tau_i - (\tau_0 + K\gamma_i^n)]^2}{\delta \tau_0} = 0 \tag{C.2}$$

$$\frac{\delta \Sigma [\tau_i - (\tau_0 + K\gamma_i^n)]^2}{\delta n} = 0 \tag{C.3}$$

For N number of shear stress/shear rate data pairs these derivatives are solved to develop Equation C.4 to C.6.

$$\tau_0 = \frac{\Sigma\tau_i \Sigma\gamma_i^{2n} - \Sigma\tau_i\gamma_i^n \Sigma\gamma_i^n}{N\Sigma\gamma_i^{2n} - (\Sigma\gamma_i^n)^2} \tag{C.4}$$

$$K = \frac{N\Sigma\tau_i\gamma_i^n - \Sigma\gamma_i^n \Sigma\tau_i}{N\Sigma\gamma_i^{2n} - (\Sigma\gamma_i^n)^2} \tag{C.5}$$

$$E = \tau_0 \Sigma\gamma_i^n \ln\gamma_i + K\sigma\gamma_i^{2n} \ln\gamma_i - \Sigma\tau_i\gamma_i^n \ln\gamma_i = 0 \tag{C.6}$$

Equation C.4 and C.5 can for a given value of n be used to calculate τ_0 and K. Excels solver tool can be used to solve the system of equations by finding which value of n that gives $E = 0$ in Equation C.6.

D. *Risk Assessment*

Risk assessments created with Risk Manager are presented in this appendix. The risk assessments and considerations were done by Espen Johansen, Gunnar Giil and Pål Skalle.

Detailed Risk Report

ID	15748	**Status**	**Date**
Risk Area	Risikovurdering: Helse, miljø og sikkerhet (HMS)	Created	29.11.2016
Created by	Gunnar Lia Giil	Assessment started	29.11.2016
Responsible	Pål Skalle	Actions decided	29.11.2016
		Closed	

Risk Assessment:

Laboratory - Project-/Master thesis

Valid from-to date:

-

Location:

4 - Sydområdet / 442 - PTS, hallbygg / 1010 - 1. etasje

Goal / purpose

Fluid displacement tests with oil, laponite and CMC.

Background

Experimental tests. Project-/master thesis.

Description and limitations

Pumping of fluids in pipe systems. Measurements of volumes, time and rheology.

Prerequesites, assumptions and simplifications

Relying on experimental results. The liquids are not very toxic.

Attachments

[Ingen registreringer]

References

[Ingen registreringer]

Summary, result and final evaluation

The summary presents an overview of hazards and incidents, in addtition to risk result for each consequence area.

Hazard: **Pipe system**

Incident: **Leakage**

Not to be analyzes.

Planned action	Responsible	Registered	Deadline	Status
Oljelekkasje	Gunnar Lia Giil	29.11.2016	29.11.2016	Evaluated

Hazard: **Pump**

Incident: **Spark**

Not to be analyzes.

Final evaluation

This is concidered a low rsik project with limited hazards and consequences. Risk assesments will also be carried out continuously.

Organizational units and people involved

A risk assessment may apply to one or more organizational units, and involve several people. These are lsited below.

Organizational units which this risk assessment applies to

- NTNU

Participants

Espen Johansen

Gunnar Lia Giil

Readers

[Ingen registreringer]

Others involved/stakeholders

[Ingen registreringer]

The following accept criteria have been decided for the risk area Risikovurdering: Helse, miljø og sikkerhet (HMS):

Helse	Materielle verdier	Omdømme	Ytre miljø

Overview of existing relevant measures which have been taken into account

The table below presents existing measures which have been take into account when assessing the likelihood and consequence of relevant incidents.

Hazard	Incident	Measures taken into account

Existing relevant measures with descriptions:

Protection

Coveralls
Safety shoes
Gloves
Helmet
Glasses
Hearing protection

Ventilation

Big room, good ventilation.

Collection of oil

Oil drain in the floor.

Ignition of oil

Fire extinguisher available close by.
The oil is kept away from sources of ignition.

Safety valve

Safety valve is in place in case of pipeline leakage occurs.

Laponite

Water based fluid. May cause skin irritation. Protective clothes, gloves and glasses should be used. In case of exposure to:
skin - wash with water.
eyes - use suitable rinsing equipment located by the marked first aid kit.

CMC

Water based fluid. May cause skin irritation. Protective clothes, gloves and glasses should be used.
In case of exposure to:
Skin - Wash with water
Eyes - Use suitable rinsing equipment located by the marked first aid kit.

Oil

Oil based fluid. May cause skin irritation. Protective clothes, goves and glasses should be used.
In case of exposure to:
Skin - Wash with water
Eyes - Use suitable rinsing equipment located by the marked first aid kit.

Detailed view of hazards and incidents:

Hazard: Pipe system

Leakage of fluids

Incident: Leakage

Fluid leakage resulting in spilling.

Likelihood of the incident (common to all consequence areas): **(0)**

Kommentar:
[Ingen registreringer]

Consequence area: Helse ***Risk:***

Assessed consequence: **()**

Comment: [Ingen registreringer]

Consequence area: Ytre miljø ***Risk:***

Assessed consequence: **()**

Comment: [Ingen registreringer]

Overview of risk mitiating actions which have been decided:

Below is an overview of risk mitigating actions, which are intended to contribute towards minimizing the likelihood and/or consequence of incidents:

- Oljelekkasje

Overview of risk mitigating actions which have been decided, with description:

Oljelekkasje

Lekkasje utløp fra oppsamlingstank (Påls fortrengnignssløyfe) for Exxsol D60 etter flytting.
Tettet med en ny skive+pakning.

Action decided by:	Gunnar Lia Giil
Responsible for execution:	Gunnar Lia Giil
Deadline for execution:	11/29/2016

E. *Simulation tables*

Table E.1: *Simulated volumetric efficiency data for the Herschel-Bulkley model and Newtnonian model.* $q = 0.02m3/s$, $v_{loc} = 0m/s$. *Used to manufacture part of Figure 3.15.*

Time s	Pumped volume $\#V_{pipe}$	Volumetric efficiency	
		Herschel-Bulkley	Newtonian
0.0	0.0	0.0000	0.0000
0.3	0.4	0.3913	0.3913
0.6	0.8	0.7114	0.6806
0.9	1.2	0.8156	0.7871
1.2	1.6	0.8641	0.8403
1.5	2.0	0.8923	0.8722
1.8	2.3	0.9108	0.8935
2.1	2.7	0.9239	0.9087
2.4	3.1	0.9336	0.9201
2.7	3.5	0.9411	0.9290
3.0	3.9	0.9471	0.9361
3.3	4.3	0.9520	0.9419
3.6	4.7	0.9561	0.9468
3.9	5.1	0.9595	0.9509
4.2	5.5	0.9624	0.9544
4.5	5.9	0.9649	0.9574
4.8	6.3	0.9672	0.9601
5.1	6.7	0.9691	0.9624
5.4	7.0	0.9708	0.9645
5.7	7.4	0.9724	0.9664
6.0	7.8	0.9738	0.9681
6.3	8.2	0.9750	0.9696
6.6	8.6	0.9762	0.9710
6.9	9.0	0.9772	0.9722
7.2	9.4	0.9782	0.9734
7.5	9.8	0.9791	0.9744
7.8	10.2	0.9799	0.9754
8.1	10.6	0.9806	0.9763
8.4	11.0	0.9813	0.9772
8.7	11.3	0.9820	0.9780

Table E.2: *Simulated volumetric efficiency data for the Herschel-Bulkley model and Newtnonian model.* $q = 0.02m3/s$, $v_{loc} = 1m/s$. *Used to manufacture part of Figure 3.15.*

Time s	Pumped volume $\#V_{pipe}$	Volumetric efficiency	
		Herschel-Bulkley	Newtonian
0.0	0.0	0.0000	0.0000
0.3	0.4	0.3913	0.3913
0.6	0.8	0.7288	0.6946
0.9	1.2	0.8382	0.8095
1.2	1.6	0.8888	0.8666
1.5	2.0	0.9179	0.9006
1.8	2.3	0.9369	0.9230
2.1	2.7	0.9501	0.9389
2.4	3.1	0.9598	0.9506
2.7	3.5	0.9672	0.9596
3.0	3.9	0.9730	0.9666
3.3	4.3	0.9776	0.9723
3.6	4.7	0.9813	0.9769
3.9	5.1	0.9844	0.9807
4.2	5.5	0.9870	0.9838
4.5	5.9	0.9891	0.9865
4.8	6.3	0.9909	0.9887
5.1	6.7	0.9925	0.9906
5.4	7.0	0.9938	0.9922
5.7	7.4	0.9949	0.9936
6.0	7.8	0.9958	0.9948
6.3	8.2	0.9966	0.9958
6.6	8.6	0.9973	0.9966
6.9	9.0	0.9979	0.9974
7.2	9.4	0.9984	0.9980
7.5	9.8	0.9988	0.9985
7.8	10.2	0.9991	0.9989
8.1	10.6	0.9994	0.9992
8.4	11.0	0.9996	0.9995
8.7	11.3	0.9998	0.9997

Table E.3: *Simulated volumetric efficiency data for the Herschel-Bulkley model and Newtnonian model.* $q = 0.02m3/s$, $v_{loc} = 3m/s$. *Used to manufacture part of Figure 3.15.*

Time s	Pumped volume $\#V_{pipe}$	Volumetric efficiency	
		Herschel-Bulkley	Newtonian
0.0	0.0	0.0000	0.0000
0.3	0.4	0.3913	0.3913
0.6	0.8	0.7635	0.7219
0.9	1.2	0.8820	0.8540
1.2	1.6	0.9339	0.9165
1.5	2.0	0.9618	0.9512
1.8	2.3	0.9782	0.9720
2.1	2.7	0.9882	0.9848
2.4	3.1	0.9943	0.9927
2.7	3.5	0.9979	0.9972
3.0	3.9	0.9996	0.9994
3.3	4.3	1.0000	1.0000
3.6	4.7	1.0000	1.0000
3.9	5.1	1.0000	1.0000
4.2	5.5	1.0000	1.0000
4.5	5.9	1.0000	1.0000
4.8	6.3	1.0000	1.0000
5.1	6.7	1.0000	1.0000
5.4	7.0	1.0000	1.0000
5.7	7.4	1.0000	1.0000
6.0	7.8	1.0000	1.0000
6.3	8.2	1.0000	1.0000
6.6	8.6	1.0000	1.0000
6.9	9.0	1.0000	1.0000
7.2	9.4	1.0000	1.0000
7.5	9.8	1.0000	1.0000
7.8	10.2	1.0000	1.0000
8.1	10.6	1.0000	1.0000
8.4	11.0	1.0000	1.0000
8.7	11.3	1.0000	1.0000

Table E.4: *Simulated volumetric efficiency data for the Herschel-Bulkley model and Newtnonian model.* $q = 0.01 m3/s$, $v_{loc} = 0.5 m/s$. *Used to manufacture part of Figure 3.16.*

Time s	Pumped volume $\#V_{pipe}$	Volumetric efficiency	
		Herschel-Bulkley	Newtonian
0.0	0.0	0.0000	0.0000
0.2	0.1	0.1304	0.1304
0.4	0.3	0.2609	0.2609
0.6	0.4	0.3913	0.3913
0.8	0.5	0.5218	0.5218
1.0	0.7	0.6542	0.6255
1.2	0.8	0.7284	0.6946
1.4	0.9	0.7771	0.7439
1.6	1.0	0.8119	0.7808
1.8	1.2	0.8381	0.8095
2.0	1.3	0.8586	0.8324
2.2	1.4	0.8751	0.8510
2.4	1.6	0.8887	0.8666
2.6	1.7	0.9000	0.8797
2.8	1.8	0.9097	0.8909
3.0	2.0	0.9179	0.9006
3.2	2.1	0.9251	0.9090
3.4	2.2	0.9313	0.9164
3.6	2.3	0.9369	0.9230
3.8	2.5	0.9418	0.9289
4.0	2.6	0.9461	0.9341
4.2	2.7	0.9501	0.9389
4.4	2.9	0.9536	0.9432
4.6	3.0	0.9569	0.9471
4.8	3.1	0.9598	0.9506
5.0	3.3	0.9625	0.9539
5.2	3.4	0.9649	0.9568
5.4	3.5	0.9672	0.9596
5.6	3.7	0.9693	0.9621
5.8	3.8	0.9712	0.9645

Table E.5: *Simulated volumetric efficiency data for the Herschel-Bulkley model and Newtnonian model.* $q = 0.02m3/s$, $v_{loc} = 0.5m/s$. *Used to manufacture part of Figure 3.16.*

Time s	Pumped volume $\#V_{pipe}$	Volumetric efficiency	
		Herschel-Bulkley	Newtonian
0.0	0.0	0.0000	0.0000
0.2	0.3	0.2609	0.2609
0.4	0.5	0.5218	0.5215
0.6	0.8	0.7201	0.6876
0.8	1.0	0.8013	0.7706
1.0	1.3	0.8471	0.8204
1.2	1.6	0.8766	0.8535
1.4	1.8	0.8972	0.8772
1.6	2.1	0.9125	0.8949
1.8	2.3	0.9242	0.9086
2.0	2.6	0.9335	0.9196
2.2	2.9	0.9411	0.9286
2.4	3.1	0.9473	0.9360
2.6	3.4	0.9526	0.9423
2.8	3.7	0.9571	0.9477
3.0	3.9	0.9609	0.9523
3.2	4.2	0.9643	0.9564
3.4	4.4	0.9672	0.9599
3.6	4.7	0.9698	0.9631
3.8	5.0	0.9722	0.9659
4.0	5.2	0.9742	0.9684
4.2	5.5	0.9761	0.9707
4.4	5.7	0.9778	0.9727
4.6	6.0	0.9793	0.9746
4.8	6.3	0.9807	0.9763
5.0	6.5	0.9820	0.9779
5.2	6.8	0.9832	0.9793
5.4	7.0	0.9842	0.9806
5.6	7.3	0.9852	0.9818
5.8	7.6	0.9861	0.9830

Table E.6: *Simulated volumetric efficiency data for the Herschel-Bulkley model and Newtonian model.* $q = 0.05m3/s$, $v_{loc} = 0.5m/s$. *Used to manufacture part of Figure 3.16.*

Time s	Pumped volume $\#V_{pipe}$	Volumetric efficiency	
		Herschel-Bulkley	Newtonian
0.0	0.0	0.0000	0.0000
0.2	0.7	0.6447	0.6185
0.4	1.3	0.8400	0.8132
0.6	2.0	0.8976	0.8780
0.8	2.6	0.9255	0.9104
1.0	3.3	0.9420	0.9299
1.2	3.9	0.9529	0.9428
1.4	4.6	0.9606	0.9520
1.6	5.2	0.9663	0.9589
1.8	5.9	0.9707	0.9643
2.0	6.5	0.9743	0.9686
2.2	7.2	0.9772	0.9721
2.4	7.8	0.9796	0.9750
2.6	8.5	0.9816	0.9775
2.8	9.1	0.9833	0.9796
3.0	9.8	0.9848	0.9814
3.2	10.4	0.9861	0.9830
3.4	11.1	0.9872	0.9844
3.6	11.7	0.9882	0.9856
3.8	12.4	0.9891	0.9867
4.0	13.0	0.9899	0.9877
4.2	13.7	0.9907	0.9886
4.4	14.3	0.9913	0.9894
4.6	15.0	0.9919	0.9901
4.8	15.7	0.9925	0.9907
5.0	16.3	0.9930	0.9914
5.2	17.0	0.9934	0.9919
5.4	17.6	0.9938	0.9924
5.6	18.3	0.9942	0.9929
5.8	18.9	0.9946	0.9933

F. *Procedure for Rheology measurements with Fann viscometer*

The following procedure for the rheology measurements were followed. The procedure is given by Fann Instrument Company (2016), but in this appendix it is described more detailed.

1. Measure the fluid temperature and heat or cool if necessary.
2. It is important that the fluid is agitated, so stir for 1 minute in small Waring blender before measurements are performed.
3. Fill the agitated fluid in the test cup up to the fill line. Place the cup on the cup stand and raise it until fluid surface is in line with the mark on the cylinder.
4. Start the motor by switching the toggle to high speed. Move the gear shift knob to 600 RPM position (bottom). It is important to change gears only when motor is running.
5. When the dial reading indicator has stabilized, read θ_{600}.
6. With the gear shift knob in the lower position, the toggle should be switched to low speed (300 RPM). Wait for dial reading indicator and read θ_{300}.
7. By changing gears and speeds, readings should also be recorded for 200, 100, 6 and 3 RPM.

Gel strength can also be measured using the Fann viscometer, and the procedure is as follows (*API RP 13B-1*, 2003):

1. Stir the fluid at 600 RPM for 10 s.
2. Set the gear shift knob at 3 RPM, and turn the motor off.

3. Wait 10 s, then start the motor at 3 RPM and read the highest value. This is the initial gel strength (or 10-$second$ gel strength).

4. Stir fluid again at 600 RPM for 10 s.

5. Set the gear shift knob at 3 RPM, and turn the motor off.

6. Wait 10 min, then start the motor at 3 RPM and read the highest value. This is the 10-$minute$ gel strength. Note that measurements are in $lb/100ft^2$.